Development of SQUID based Magnetocardiography system & Cardiac signal-source analysis using Ensemble Empirical Mode Decomposition

By

N. MARIYAPPA

(Enrolment No.: PHYS02200804003)

Indira Gandhi Centre for Atomic Research, Kalpakkam

A thesis submitted to the

Board of Studies in Physical Sciences

In partial fulfillment of requirements

For the Degree of

DOCTOR OF PHILOSOPHY

of

HOMI BHABHA NATIONAL INSTITUTE

September, 2013

Homi Bhabha National Institute

Recommendations of the Viva Voce Board

As members of the Viva Voce Board, we certify that we have read the dissertation prepared by **N. Mariyappa** entitled **"Development of SQUID based Magnetocardiography system & Cardiac signal-source analysis using Ensemble Empirical Mode Decomposition"** and recommend that it may be accepted as fulfilling the dissertation requirement for the Degree of Doctor of Philosophy.

____ **Date:**

Chairman - Dr. B.V.R. Tata

____ **Date:**

Guide/Convener - Dr. C.S. Sundar

____ **Date:**

Member 1 - Shri. M.P. Janawadkar

____ **Date:**

Member 2 - Dr. B.P.C. Rao

____ **Date:**

Member 3 - Dr. G. Baskaran

____ **Date:**

External Examiner

Final approval and acceptance of this dissertation is contingent upon the candidate's submission of the final copies of the dissertation to HBNI.

Date:

Place:

CERTIFICATE

I hereby certify that I have read this dissertation prepared under my direction and recommend that it may be accepted as fulfilling the dissertation requirement.

Date:

Place: **(C.S. Sundar)**

STATEMENT BY AUTHOR

(N. Mariyappa)

DECLARATION

I, hereby declare that the investigation presented in the thesis has been carried out by me. The work is original and has not been submitted earlier as a whole or in part for a degree/diploma at this or any other Institution/University.

(N. Mariyappa)

Dedicated

To

My Parents

ACKNOWLEDGEMENTS

It is my pleasure to thank all those who contributed in many ways to the success of this study and made it an unforgettable experience for me.

I am extremely grateful to my principal supervisor, **Dr. C.S. Sundar**, Director, Materials Science Group (MSG), IGCAR, for his guidance, support and patience without which, this thesis would not have been possible. I really appreciate his willingness to meet me at short notice every time and for critically going through endless drafts of my thesis and research papers. I remain amazed that despite his busy schedule, he was able to give ready attention to my drafts and could give valuable suggestions, that has added substantially to the style of presentation, comprehension as well as technical content, the latter, through extensive discussions.

My sincere gratitude is reserved for my second supervisor **Shri. M.P. Janawadkar**, Head, Condensed Matter Physics Division (CMPD), MSG, IGCAR. He has always made himself available to clarify my doubts despite his busy schedules and I consider it a great privilege and opportunity to do my doctoral programme under his guidance and to learn from his rich research expertise. His insightful scientific discussions and clarification have greatly improved my understanding of the basics and enriched my comprehension. I always wonder at his patience while correcting the draft of my papers and the thesis in making them free of grammatical and technical errors. I am very grateful to him for all these and for several other aspects of my tenure as a doctoral student.

I am much indebted to **Dr. T.S. Radhakrishnan**, Formerly Head, Materials Science Division and currently DST supported Scientist, MEG Laboratory, for his valuable advice in my work, spending his precious times to read and correct this thesis, research papers and for his valuable suggestions and for his unconditional support in many ways. His support and friendship has been invaluable both on the academic front and at a personal level, for which I consider myself extremely fortunate. He patiently provided the vision, encouragement and advice necessary for me to proceed through the entire doctorial program and to complete my dissertation.

I owe special thanks to my doctoral committee members, **Dr. B.V.R. Tata**, **Dr. B.P.C. Rao**, and **Dr. G. Baskaran** for their support, guidance and helpful suggestions. Their guidance has served me well and I owe them my heartfelt gratitude.

I would like to express my sincere gratitude to **Dr. K. Gireesan** for his unconditional support and help. He has been very kind and patient and was always willing to teach me experimental aspects from his rich experience. He also helped me with planning my experiments. I owe him a debt of gratitude. I also thank him for proving liquid helium which is becoming a difficult resource, without interruption for my experiments and all the staff at the liquid helium plant.

My other colleagues in the MEG Laboratory, **S. Sengottuvel**, **C. Parasakthi** and **Rajesh Patel**, have all extended their support in very special ways, and I gained a lot from them, through their personal and scholarly interactions, their suggestions at various points of my research programme. I thank all of them, for the stimulating discussions, and for all the fun we have had in the last five years.

I take this opportunity to sincerely acknowledge the **Department of Atomic Energy, Government of India**, for providing financial assistance in the form of Junior and Senior Research Fellowships which buttressed me to perform my work comfortably.

I thank the former and present Directors, IGCAR, **Dr. Baldev Raj** and **Dr. P.R. Vasudeva Rao** and **Dr. M. Saibaba**, Associate Director, RMG, IGCAR for providing me accommodation, necessary infrastructure and resources to accomplish my research work. I also express my gratitude to all the library staff for their services. I also thank all the staff members of MSG, IGCAR for their help and support. I thank **Mrs. Sasikala** and **Mrs. Uma** for their administrative help.

My heartfelt thanks to my many good friends, **P. Manimuthu, S.R. Arun, K. Balaji, N. Ganesha moorthy, K.S. Karthikeyan, A. Arokiasamy, T. Uthayakumar, M.S. Manirajan, Charles, C. Kumaran, G. Jai Ganesh, Rajesh Kannan, M. Sivanandam** and **Mrs. A. Ruby** for their valuable help and support. I am indebted to my batch mate friends **L. Herojit Singh, M. Bupathi, D. Sri Maha Vishnu, P. Ilaiyaraja, Lakshmoji Kosuru, Jagadeesh Sure, D. Sharath, S. Naveena, Pradeepkumar Samantaroy, K. Siva Srinivas, Sudhansu Pati, Ch. Kishan Singh, Soumee Chakrobarty**, and **Manan Dolakia**, for providing a stimulating and fun filled environment. I would like to thank **D. Karthikeyan, Saravana kumar, V. Mahendiran, Yazhi Suresh, Bonu venkatramana** and **Hari babu** who became voluntary subjects for my measurements and also for their fun discussions. I also thank **Mrs. Devi** and **Mr. Suresh** for their help in collecting and Xeroxing the course materials and for making my stay at the JRF enclave, comfortable. I thank all the senior and junior research scholars and friends in IGCAR with whom I interacted in several ways and whose names I might have missed out here inadvertently.

I would also like to thank all my **Teachers**, who throughout my educational career have supported and encouraged me to believe in my abilities. They have directed me in various difficult situations, which have helped to reach this accomplishment.

I owe a lot to my parents, **V. Narayanan** and **N. Thilagam**, who encouraged and helped me at every stage of my personal and academic life, and have longed to see this achievement come true. I also would like to thank my extended family members and relatives, **S. Dhivya, S. Nivedha, S. Shalini, S. Lusiltha** and **S. Thamizh mani** for their personal support and encouragement.

Above all, I owe it all to Almighty **God** for granting me the wisdom, health and strength to undertake this research task and enabling me to take it to completion.

Contents

Abstract

MagnetoCardioGraphy (MCG), which is the magnetic counterpart of the surface ElectroCardioGraphy (ECG), measures the magnetic field (typically 50pT at QRS peak) produced by the electrical activity of the myocardial tissues constituting the heart in a non-invasive and non-contact way by harnessing the highly sensitive Superconducting QUantum Interference Devices (SQUIDs). The inherent advantages of the MCG technique have been explored in clinical research over the last two decades and is now receiving considerable attention. In view of this, several research groups, including that at IGCAR, Kalpakkam, have established multichannel MCG systems. These enable simultaneous measurements of magnetic fields at a discrete set of points on the thorax to generate a comprehensive picture of the magnetic field distribution, which makes it possible to visualize the cardiac source in terms of current density maps and source reconstruction through the solution of the inverse problem.

This thesis describes the efforts involved in the assembly and wiring of a multichannel MCG measurement facility and in using the facility to record multichannel MCG data. Since the measured MCG data often has a low signal-to-noise ratio (SNR), it was essential to explore methods to denoise the measured data prior to using for estimation of source parameters. Towards this, Ensemble Empirical Mode Decomposition (EEMD) based approach was developed and its performance in enhancing the SNR was assessed by comparing it with other standard denoising techniques based on wavelet transform and Independent Component Analysis (ICA). A combination of EEMD and ICA applied to the multichannel MCG data is shown to have the twin advantages of significant improvement in SNR and a lower computational burden. An assessment of the performance of the combination of EEMD and ICA has been compared with other standard techniques such as the use of ICA alone and wavelet enhanced ICA (wICA). The denoised data has been used for the construction of pseudocurrent density maps and for estimation of source parameters in the context of a single equivalent current dipole model. The effect of signal denoising on the pseudocurrent density maps and on the estimation of source parameters is discussed.

List of Figures

List of Tables

Abbreviations

ADC	Analog-to-Digital Converter
AV node	Atrio-Ventricular node
BSPM	Body Surface Potential Mapping
DT	Direct Thresholding
ECD	Equivalent Current Dipole
ECG	Electrocardiography
EEMD	Ensemble Empirical Mode Decomposition
EEMD-ICA	Combined EEMD and ICA
EMD	Empirical Mode Decomposition
FLL	Flux Locked Loop
FRP	Fiber Reinforced Plastic
HHT	Hilbert-Huang Transform
ICA	Independent Component Analysis
ICs	Independent Components
IGCAR	Indira Gandhi Centre for Atomic Research
IMF	Intrinsic Mode Function
IT	Interval Thresholding
LM	Levenberg-Marquardt
MCG	Magnetocardiography
MEG	Magnetoencephalography
MFM	Magnetic Field Map
MRI	Magnetic Resonance Imaging
MSR	Magnetically Shielded Room
MUSIC	MUltiple Signal Identification and Classification
NM	Nelder-Mead
P2S	0.2 times the standard deviation of the signal
PCA	Principal Component Analysis
PCD	Pseudo Current Density
RFSR	Radio Frequency Shielded Room
RMSE	Root Mean Square Error
RSQ	R-square
SAMCG	Signal Averaged MCG
SDS	Standard Deviation of the Second order derivative
SNR	Signal-to-Noise Ratio
SQUID	Superconducting QUantum Interference Device
SSP	Signal Space Projection
wICA	wavelet enhanced ICA

1 Introduction to MCG and Data Analysis

This chapter presents an introduction to magnetocardiography (MCG) and the origin of biomagnetic fields associated with the physiological activities of the human heart. The clinical applications of MCG and some of the advantages of this technique are described. This chapter also discusses the necessity for MCG signal pre-processing and concludes after presenting a brief description of the objectives of the present study.

1.1 Electrophysiology of the Heart

Electrophysiology of organs such as human heart and human brain involves the flow of tiny currents, which are accompanied by the appearance of an electric potential on the outer skin surface as well as a magnetic field. The ionic current, which flows across the cell membrane of a cardiac myocyte, is primarily responsible for the magnetic field measured in the Magnetocardiography (MCG) measurements as well as the potential difference measured in the Electrocardiography (ECG) and the Body Surface Potential Mapping (BSPM) measurements [1, 2]. Thus, both ECG and MCG measurements have a common physiological origin. The transport of ions across the cell membrane is governed by processes similar to those operating in the nerve cell or a skeletal muscle cell, except that the duration of the action potential is almost two orders of magnitude longer (about 300ms) in a cardiac cell, compared to that of the nerve cells or the cells of the skeletal muscle (about 2ms) [2].

The coordinated contraction and dilation of the atria and ventricles are maintained by the heart's own intrinsic electrical conduction system which conducts the impulses generated at the sinoatrial node throughout the cardiac muscle; the latter is composed of specialized muscle tissues that initiates and conducts the electrical impulse through a specialized conduction pathway [1, 4]. Any interruption or abnormal changes in the heart's electrical conduction system may potentially result in irregular cardiac activity or arrythmia.

The conduction pathway of the cardiac impulse is illustrated in fig.1.1. The sinoatrial (SA) or sinus node embedded in the posterior wall of the right atrium, near the entrance of the superior vena cava initiates the electrical impulse spontaneously at a rapid rate (60-100 beats per minute). This impulse propagates through the myocardium of the atria (left and right) and stimulates the atria to contract; this part of the electrical conduction is seen as P-wave in the ECG/MCG. The electrical impulse then propagates to the Atrio-Ventricular (AV) node, which electrically isolates the atrial myocardium from the ventricular myocardium and is located within the floor of the right

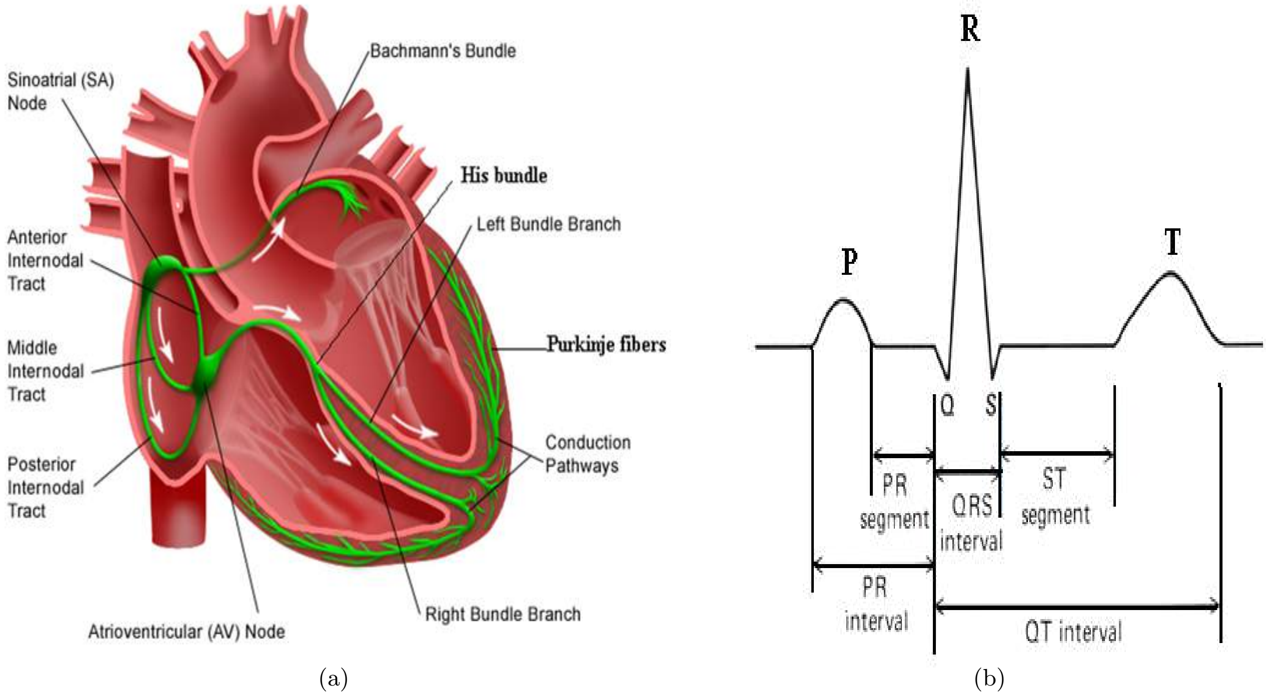

Figure 1.1: The left panel (a) shows the cardiac impulse conduction pathway (adapted from [3]) and the right panel (b) shows the pattern of normal cardiac cycle. The electrical impulse originates at the SA node and propagates through the AV node via atria, bundle of His, left and right bundle branches and Purkinje fibers. The electrical conduction allows the cardio-myocytes to depolarize (associated with mechanical contraction) and repolarize (associated with mechanical dilation) and the resulting events manifest in the cardiac cycle as P-wave (atrial depolarization), QRS complex (ventricular depolarization) and T-wave (ventricular repolarization). The intervals and segments in the cardiac cycle indicated in the panel (b) are crucial for clinical diagnosis.

atrium near the interatrial septum. At the AV node, the electrical conduction is delayed so that the atrial contraction would be completed fully before the ventricular activation. After the AV node, the impulse enters into the distal portion of the AV node called His bundle or AV bundle, which is located at the upper part of the interventricular septum, and then divides into left and right bundle branches on either side of the interventricular septum. The impulse reaches the terminal of the left and right bundle branches and then enters into the ramification of the Purkinje fibers. This causes the depolarization of the myocytes in the ventricles, seen as QRS complex in the ECG/MCG, and the activation propagates in the direction from endocardium to epicardium. This activation results in the simultaneous contraction of both the ventricles. The repolarization of the myocytes of the ventricles takes place after the ventricular contraction and manifests as a T-wave in the ECG/MCG. The repolarization of the atria usually does not leave a signature in the recorded ECG/MCG since it overlaps with the ventricular depolarization and is, therefore, masked by the much stronger QRS complex.

1.2 Magnetocardiography (MCG)

Magnetocardiography (MCG) [1, 2, 4, 5, 6, 7] is a non-invasive and non-contact functional imaging or mapping technique which characterize the spatial distribution of cardiac magnetic field on the anterior surface of the thorax. MCG is already providing valuable information, which is complementary to that provided by Electrocardiography (ECG) in the clinical practice. Historically, Baule and Mcfee [8] were the first to record the MCG signal from a canine heart in 1963 using induction coils with almost two million turns as magnetic field sensors. These recordings were relatively noisy, however, and, when Superconducting QUantum Interference Device (SQUID) sensors became available, they were used by David Cohen to record the first human magnetocardiogram inside a Magnetically Shielded Room in 1970 [9, 10]. Since then, SQUID sensors have emerged as the sensors of choice with adequate sensitivity to measure the extremely weak biomagnetic fields ranging from 100 femto-Tesla to 100 pico-Tesla. Fig.1.2 illustrates a schematic representation of a typical MCG measurement set-up comprising SQUID sensors immersed in liquid helium in a cryostat since, during the operation, the SQUID sensors have to be cooled to an operating temperature of 4.2K. The magnetic field lines perpendicular to the anterior thoracic surface, which

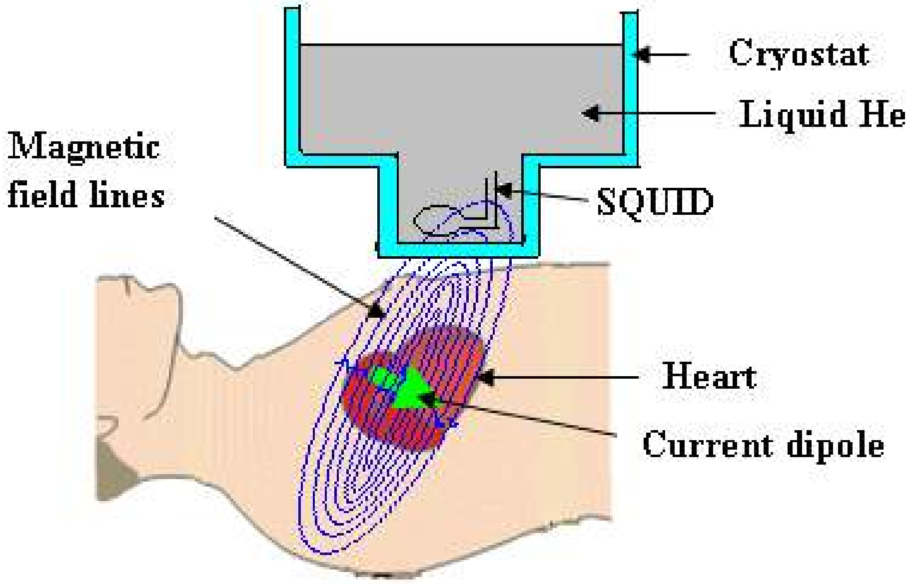

Figure 1.2: The schematic illustration of the non-invasive and non-contact magnetocardiographic technique which measures the magnetic fields associated with the electrical activity of the heart using the Superconducting QUantum Interference Devices (SQUIDs). The arrow illustrates the direction of the equivalent current dipole responsible for the measured magnetic field distribution.

are associated with a tangentially oriented current dipole, are sensed by the SQUID sensor, which acts as a transducer for detecting the changes in the magnetic field and generates a voltage signal proportional to the instantaneous magnetic field intensity at the location of the sensor. The voltage output from the SQUID sensor is processed by sensor electronics and is suitably recorded for further analysis [5]. In the following sections, we compare the MCG with ECG and give a brief account of the challenges involved in MCG measurements.

1.3 Comparison of MCG with ECG

Fig.1.3 schematically shows the difference in sensitivity of ECG and MCG to the type of current sources. Although the ECG and MCG seek to measure different effects associated with the electrophysiological activity of the same cardiac source and show morphologically same features (P-wave, QRS complex, and T waves) in the temporal dependence of the cardiac cycle, they have different sensitivities to different orientations of the underlying current sources or dipoles [2]. The ECG is sensitive to both radially and tangentially oriented current dipoles, while the MCG is more

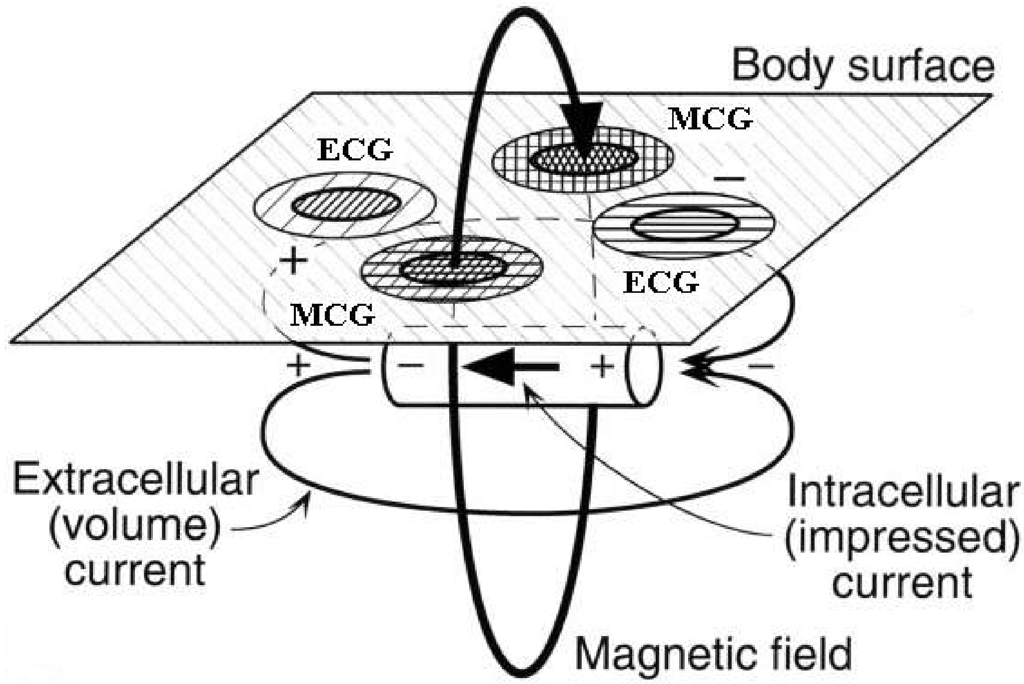

Figure 1.3: The difference in the sensitivity of ECG and MCG techniques to the flow of volume currents and primary currents respectively is schematically illustrated (adapted from [11]). The sensitivity difference of ECG and MCG to different types of sources (primary current in MCG and volume current in ECG) reflects the inherent complementarity of the two techniques.

sensitive to the tangentially oriented current dipole (fig.1.2); indeed, in special conductor geometries such as the spherically symmetric conductor or the horizontally layered conductor, the contribution of a radially oriented dipole to the normal component of the magnetic field (which represents the measured MCG signal) may be shown to vanish [12]. A vortex current source [13] oriented parallel to the thoracic plane is more likely to manifest in the MCG signal, but leave only a relatively weak signature in the ECG, especially since the ECG senses the effects due to volume currents while MCG senses the effects due to the primary current (the normal component of the magnetic field produced by volume currents may be shown to vanish in special conductor geometries such as spherically symmetric conductor or the horizontally layered conductor).

A very significant advantage of the MCG measurements arises from the fact that the measured magnetic fields are not much influenced by the electrical conductivity of the intervening tissues [14] whereas measurements of electric potential critically depend on the values of the electrical conductivity of the intervening tissues; indeed, presence of poor electrical conductors like bones between the source and measurement points results in attenuation and distortion of the measured ECG signals (presence of skull makes this an even more serious issue in the context of Electroencephalography (EEG)). The electrical conductivity of the tissues is inhomogeneous and anisotropic making the reconstruction of the sources from the ECG data a relatively difficult mathematical problem. Since the MCG is sensitive to primary current (rather than volume current) and is relatively insensitive to the conductivity distribution of intervening tissues, the solution of the inverse problem is slightly more straightforward in the context of MCG compared to ECG. This translates into a superior source localization accuracy when MCG data is used as compared to that attainable using the ECG data. It is also well known from Helmholtz's theorem that a bounded vector field (source current density) can be reconstructed only if both the divergence (flow source likely to manifest in ECG) and curl (vortex source likely to manifest in MCG) of the vector field are specified reflecting the inherent complementarity between ECG and MCG. This difference in the sensitivities of ECG and MCG to different types of sources (fig.1.3) makes these two techniques as complimentary tools [11] for investigating the cardiac activity, and, whenever feasible, ECG and MCG signals may be simultaneously measured to construct a more comprehensive and reliable picture of the underlying cardiac electrophysiology.

1.4 Advantages and clinical applications of MCG

As mentioned above, although, both the ECG and the MCG techniques are complementary, magnetocardiography (MCG) offers several distinct advantages over the more conventional electrocardiography (ECG). Some of these advantages are listed below [2, 4, 15, 16]:

- As the technique is non-contact, the time for subject preparation (such as skin preparation and establishing contact with a conducting gel in ECG), is much less compared to ECG. Since MCG does not require electrode attachment (as required for ECG), the artifacts associated with the fluctuating skin-electrode contact potential, which may affect the measured ECG data, are absent. The MCG technique is also suitable for the patients with burns on the anterior thoracic skin surface since there is no need to establish any contact with the skin surface; recording of ECG in such patients with burns on the chest surface might pose a difficulty.

- Since ECG records electric potential, necessity of a reference electrode with respect to which the measurements are made is critical to perform ECG measurements; however, it is difficult to find a location on the body which is at zero or a steady time invariant potential, making the ECG measurements sensitive to the choice of the reference electrode. On the other hand, measurements of magnetic field in MCG are absolute and do not require any reference.

- MCG is suitable for the detection of vortex (circular) currents in a plane parallel to the skin surface; such sources may go undetected in ECG. The detection of such currents is of clinical importance in the early diagnosis of myocardial infarction, caused by the total or partial occlusion of a coronary artery.

- MCG is not much sensitive to the variations in the electrical conductivity of the intervening tissues between the sensor and the current source, whereas electrical conductivity of the intervening tissues critically affects the measured ECG signals. This results in a lower source localization error in MCG compared to what is attainable using ECG.

- The presence of electrically insulating layers (*vernix caseosa*) makes recording of foetal ECG relatively difficult during the later period of gestation. However, presence of vernix caseosa does not pose any difficulty in recording the MCG.

- The evaluation of the DC shift of the ST segment of the cardiac cycle, which is important for the detection of myocardial infarction, is possible using the MCG measurement whereas in the ECG, the fluctuations of the skin-to-electrode resistance distort the baseline making the determination of ST shift difficult.

- As the magnetic measurements are unaffected by the electrical conductivity of the intervening tissues, the posterior MCG is possible whereas in the ECG the intervening (low conductivity or high resistivity) tissues completely distort the electrical signal necessitating the use of an oesophageal lead for recording posterior ECG.

- As MCG has a high sensitivity for the detection of tangential currents, it is particularly suitable for the detection of abnormal activation, whereas in the ECG, the signals associated with the tangential components are attenuated by Brody effect.

- The detection of multiple dipoles is possible using MCG. Certain configurations of dipoles may result in a relatively weak signal in ECG measurements.
- Visualization of cardiac current through the construction of pseudo current density maps, which are constructed by evaluating the spatial gradients of the magnetic field, is possible with MCG; such maps cannot be constructed using the ECG data.

MCG is found to have greater sensitivity and specificity in the detection of cardiac disorders, especially in cases where the ECG may be nonspecific, and is therefore emerging as a technique with a high potential to significantly improve the diagnostic accuracy [17]. Here, we list a few of the clinical applications of MCG, drawn from the literature; the list is representative and, by no means, exhaustive:

- The genetically transmitted arrythmogenic diseases such as Brugada syndrome [18]
- The arrythmogenic substrates of atrial arrythmias such as Atrial Fibrillation (AF) [19]
- Detection of ST shift (rest and stress MCG) and risk stratification in Ischemic Heart Disease (IHD)/coronary artery disease/myocardial infarction [20]
- Distinguishing the inter-atrial conduction pathways [21]
- Noninvasive recording of His bundle activity [22]
- Fetal arrythmia diagnosis [22]
- Prolongation of QT interval and dispersion [22, 23]
- Localization of cardiac arrhythmias such as ventricular tachycardia, premature ectopic beats, supraventricular arrhythmias [23]
- Monitoring rejection after heart transplantation [23]
- Detection and quantification of left ventricular hypertrophy [23, 24]
- Localization of accessary pathways or pre-excitation sites in Wolff-Parkinson-White (WPW) syndrome [23, 24]

- Three-dimensional localization of ventricular pre-excitation sites [25]

1.5 Challenges in MCG

Although, MCG has several advantages as mentioned in the earlier section 1.4, there are several challenges in performing MCG measurements with a reasonably good signal-to-noise ratio. These challenges may be categorized into two groups, viz., i) **Instrumentation** and ii) **Data analysis**. Overcoming these two challenges forms the crux of the present thesis, which describes the establishment of SQUID based MCG system for the MCG measurement on a human subject and the analysis of the measured MCG data.

The major challenges in the assembly and development of the facility for MCG measurements include the high cost of investment (SQUID sensors, magnetically shielded room, liquid helium infrastructure), high revenue costs associated with system operation and maintenance (liquid helium, low noise environment), the overall complexity of the system, and its non-portability. Since the MCG signals are extremely weak, it is necessary to exercise extra care during the design of the hardware to ensure that the measured MCG data is not contaminated with parasitic magnetic noise.

With regard to the MCG data analysis, the challenges involved are briefly discussed in the following section 1.5.1.

1.5.1 MCG Data Analysis

The clinical diagnosis is, in general, based on empirical correlation of a particular type of cardiac dysfunction with the observed changes in the amplitude as well as durations of different segments (see fig.1.1(b)) of the cardiac cycle in a typical ECG measurement; however, accurate MCG measurements offer a potential to noninvasively determine the precise location of the abnormal (or normal) electrical activity of the cardiac source and, thus, provide information of value to the cardiologist. This possibility of determining the source responsible for the observed spatial distribution of cardiac magnetic field using a multichannel MCG system, however, runs into problems when the measured MCG signals have a relatively poor signal-to-noise ratio. The measured MCG signals are often contaminated by different types of parasitic noise (which will be discussed subsequently in section 1.5.1(a)) resulting in a deterioration of the signal-to-noise ratio. The reasons for the choice of MCG over ECG for the purpose of source localization has already been explained in section 1.4.

The multichannel MCG systems enable simultaneous measurements of magnetic field at a discrete set of points on the thorax to generate a comprehensive picture of the magnetic field distribution. These systems offer the scope for visualization of the source in terms of current density maps [26], and source reconstruction through the solution of the inverse problem [27]. In the context of MCG, the transformation of the as recorded MCG data to the visualization of magnetic field maps and the interpretation of data (post-processing) through the solution of the inverse problem is termed as data analysis, which includes the pre-processing of data as the necessary first step. In the next section, we discuss the importance of preprocessing of the MCG signals.

Necessity of MCG Signal Preprocessing

The source of biomagnetic fields has been often modelled as an Equivalent Current Dipole (ECD) [4, 6] with a changing magnitude and direction. The location of the source (or ECD) is inferred through the solution of the inverse problem. However, we know that the inverse problem is ill-posed and its solution may be non-unique in three dimensions [27]; the source localization accuracy, in general, depends on various factors such as measurement noise, source modeling, volume conductor modeling, approach used for solving the inverse problem etc. The source modeling, volume conduction, and the method used for solving the inverse problem are under the control of the user and it is possible to minimize the localization error resulting from these by adopting a more realistic model at the expense of an enhancement of the computational burden. However, the inherent noise present in the measurement can distort the data, especially when the signal-to-noise ratio is not sufficiently high as is the case with most biomagnetic measurements, and can pose a real difficulty in the reliable reconstruction of the source from the measured magnetic field distribution. The contribution to the magnetic noise by many sources of environmental noise such as those associated with power-line interference (50 Hz), movement of heavy vehicles or magnetic objects in the neighbourhood etc., may be attenuated to the required extent by performing the measurements inside a magnetically shielded room (MSR) and by using superconducting gradiometers to couple the signal to the SQUID sensor. However, the magnetic noise associated with several other types of sources cannot be reduced and continues to contaminate the measured data. These include biological artifacts resulting from the movement of the subject or a muscle-mass relative to the sensor array and magnetic noise resulting from biological sources other than the one under investigation (which may be clubbed together as parasitic sources of noise). It is extremely important to ensure that these parasitic sources of noise, if present, do not significantly affect the stability and robustness of the solution to the inverse problem, irrespective of the details of the modeling of source and volume conductor. As the model does not account for the existence of such noise in the measured data, the presence of any such parasitic noise would act as a perturbation during the solution of the inverse problem and lead to an avoidable uncertainty in the source localization [28]. In this context, preprocessing of the measured signals to eliminate or reduce the noise present in the measurements represents a necessary and crucial prerequisite for the subsequent data analysis, as the stability of the solution to the inverse problem is often influenced by the extent of noise. The preprocessing stage involves the reduction of noise present in the measured data and consequently leads to an enhancement in the signal-to-noise ratio. This sets the motivation for much of the computational work presented in this thesis. The objectives of the thesis are discussed in the subsequent section.

1.6 Objectives and organization of the present study

The multichannel SQUID based MCG facility at IGCAR was assembled in-house for the measurement of MCG on a human subject inside a Magnetically Shielded Room (MSR) and for imaging the functional activity of the human heart from the measured magnetic field distribution over the anterior thoracic surface of a subject. The developmental work carried out during the course of this thesis includes the setting up the facility for SQUID based measurement of biomagnetic fields and progressively upgrading the MCG facility from a single channel instrument to the 37 channel system (see fig.1.4) presently operational, assembly and calibration of SQUID sensors, estimation of field sensitivity, measurement of MCG signal on subjects and generation of magnetic field maps. A brief description of this work has been presented in the **second chapter** of this thesis.

Figure 1.4: The photograph of the 37 channel SQUID based MCG system housed inside a Magnetically Shielded Room (MSR), that is presently operational at IGCAR, Kalpakkam. The liquid helium cryostat is supported on the non-magnetic gantry. The SQUID sensors housed inside the liquid helium cryostat pick up the biomagnetic signals. The output voltage of each SQUID sensor is coupled, via twisted pairs and shielded cables, to the pre-amplifier and flux locked loop (FLL) electronics located at the top of the cryostat.

As mentioned earlier, the pre-processing of the raw data is crucial for the enhancement of SNR and consequently for the improvement in the source localization accuracy. In view of this, we adopted the Ensemble Empirical Mode Decomposition (EEMD) for the MCG signal pre-processing because of its adaptiveness and substantial reduction of mode mixing [29]. EEMD is a noise assisted signal preprocessing technique and the two important parameters, which primarily govern the effectiveness of EEMD in signal denoising, are (i) amplitude of the added noise and (ii) the number of ensemble averages [29]. When the amplitude of the added noise is larger, the number of ensemble averages necessary to suppress the added noise in the EEMD inevitably becomes too large. Conversely, when the amplitude of the added noise is very small, it may be inadequate to prevent mode mixing although the number of ensemble averages necessary to suppress the added noise is lower. Hence, the amplitude of the added noise has a decisive role in the prevention of mode mixing and in reducing the computational burden associated with a large number of ensemble averages. In view of this, we introduce an empirical relation for the noise amplitude in such a way as to be just sufficient to prevent the mode mixing while preserving the signal integrity with a lower computational burden by requiring a lower number of ensemble averages.

There are several techniques which have been used and reported in the literature for the elimination of smooth low frequency baseline drift; however, to our knowledge, no suitable method has been reported for the elimination of high frequency baseline drift, which sometimes results in sudden and discontinuous changes in the signal baseline. Towards this, we propose a novel method based on EEMD for the elimination of the high frequency baseline drift. We thus propose a novel EEMD based method for the elimination of both the low frequency as well as high frequency baseline drifts .

One of the objectives during the course of this research was to improve the signal-to-noise ratio of the MCG signal and investigate the effectiveness of different signal processing methods with regard to signal denoising. In this context, as against the conventional use of partial sum of selected intrinsic mode functions (IMFs) for the EEMD based signal denoising, we use the EEMD method with interval thresholding (IT) on the IMFs. The interval thresholding is employed to reduce the discontinuities in the reconstructed denoised version of the signal, which would otherwise appear whenever direct thresholding (DT) is used.

We also demonstrate that the weak His-Bundle activity that manifests in signal averaged MCG only after averaging over a few hundred cardiac cycles, is deciphered distinctly even after a much fewer averages after preprocessing by EEMD.

We use a combination of EEMD and ICA for the multichannel MCG data to achieve a significant enhancement in the quality of the denoised signals (see fig.1.5) compared to that achieved using ICA alone; this also results in a substantial reduction in the computational burden associated with the EEMD. The latter is because the number of ICA components derived from the multichannel data is much smaller compared to the number of channels and we need to apply EEMD to only each ICA component instead of to each channel as required during the application of the EEMD alone. We compare the results obtained by the EEMD-ICA with those obtained by the ICA alone and also by the wavelet-ICA method. The pre-processing of the MCG signal using EEMD method is covered in the **third chapter** of the thesis.

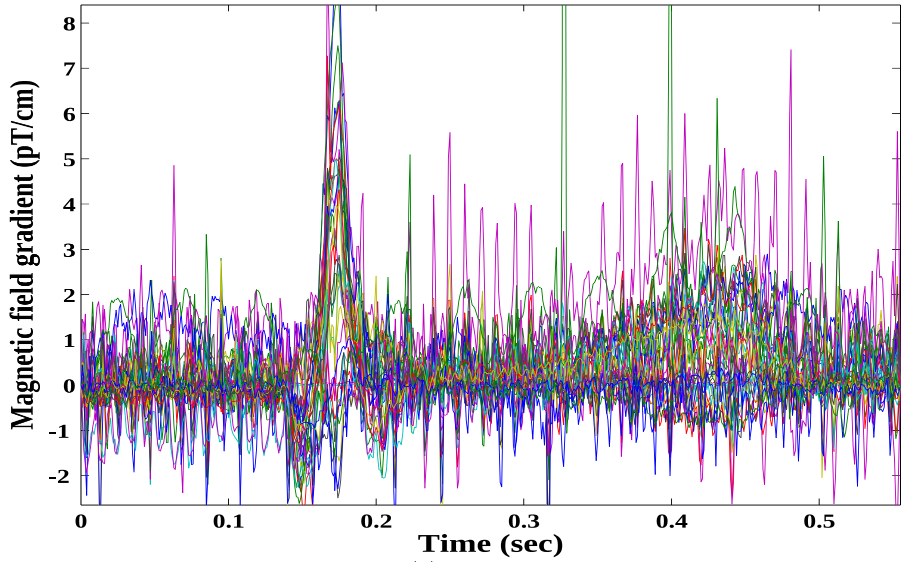

(a) Raw

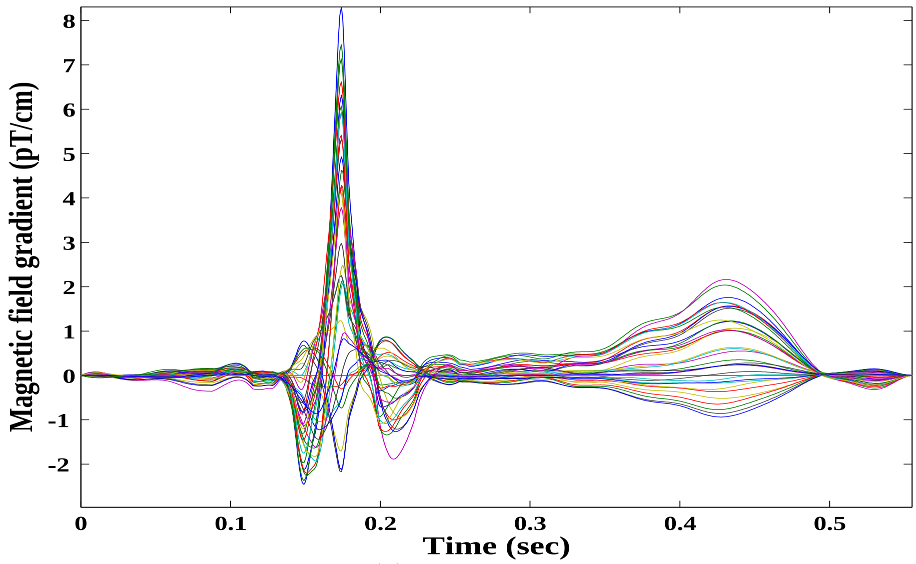

(b) EEMD-ICA

Figure 1.5: The top and bottom panels show respectively the butterfly MCG plot (superposition of all the 37 channels data) constructed using the raw data, and the data denoised by combination of Ensemble Empirical Mode Decomposition (EEMD) and Independent Component Analysis (ICA) methods. The combined use of EEMD and ICA (bottom panel) is seen to result in an effective noise reduction and a significant enhancement of signal quality.

After preprocessing of the MCG data to improve the SNR, the next step involves the source estimation. We present our results on the visualization of source current through Pseudo Current Density (PCD) maps and in some cases by a detailed estimation of source parameters through the solution of the inverse problem by choosing an appropriate source model. For the latter, we use nonlinear least square optimization technique with a set of pseudo random numbers serving as initial guess for the source parameters by imposing realistic spatial constraints on the inverse solution for estimating the cardiac source through the solution of the inverse problem. For this purpose, the cardiac source was approximated as an equivalent current dipole embedded in a horizontal layered conductor. As many independent sets of pseudo random numbers were chosen to serve as initial guess values for the source parameters in 50 independent trials carried out for estimating the source parameters using the iterative nonlinear least square optimization technique with a view to avoid the solution getting trapped in a local minimum.

We also analyze the effect of signal denoising on the Magnetic Field Map (MFM), PCD map and the estimation of source parameters obtained by solving the inverse problem for the 37 channel MCG data. We show that the denoising of the 37 channel MCG data using a combination of EEMD and ICA yields a robust estimation of the source parameters compared to what can be achieved using ICA alone and by the wavelet-ICA based technique for signal denoising. The cardiac source estimation techniques and the influence of signal denoising techniques on the source estimation are presented in the **fourth chapter** of the thesis.

The summary of all the results and the scope for future work are presented in the **fifth chapter**.

Bibliography

[1] S. J. Williamson and L. Kaufman. Biomagnetism. *J. Magnetism and Magnetic Materials.* **22** (1981) 129 - 201.

[2] J. Malmivuo and R. Plonsey. Bioelectromagnetism - Principles and Applications of Bioelectric and Biomagnetic Fields. Oxford Univ. Press. New York. 1995.

[3] http://mdmedicine.wordpress.com/2011/04/24/heart-conduction-system/#comment-79

[4] Y. Nakaya and H. Mori. Magnetocardiography. *Clin. Phys. Physiol. Meas.* **13** (1992) 191 - 229.

[5] K. Sternickel and A.I. Braginski. Biomagnetism using SQUIDs: status and perspectives. *Supercond. Sci. Technol.* **19** (2006) S160 - S171.

[6] G. Stroink, B. Hailer and P. Van Leeuwen. "Cardiomagnetism." In: Magnetism in Medicine, edited by W. Andrä and H. Nowak. Weinheim: *WILEY-VCH*, 2006, pp. 164 - 209.

[7] G. Stroink. Forty Years of Magnetocardiology. *IFMBE Proc.* **28** (2010) 1 - 8.

[8] G. Baule and R. McFee. Detection of the magnetic field of the heart. *Am. Heart J.* (1963) 95 - 96.

[9] D. Cohen. Magnetic fields around the torso: production by electrical activity of the human heart. *Science.* **156** (1967) 652 - 654.

[10] D. Cohen, E.A. Edelsack and J.E. Zimmerman. Magnetocardiograms taken inside a shielded room with superconducting point-contact magnetometer. *Appl. Phys. Lett.* **16** (1970) 278 - 280.

[11] J. Vrba and S.E. Robinson. Signal Processing in Magnetoencephalography. *METHODS.* **25** (2001) 249 - 271.

[12] C.D. Gratta, V. Pizzella, F. Tecchio and G.L. Romani. Magnetoencephalography - a non-invasive brain imaging method with 1 ms time resolution. *Rep. Prog. Phys.* **64** (2001) 1759 - 1814.

[13] S. Dutz, M.E. Bellemann, U. Leder and J. Haueisen. Passive vortex currents in magneto- and electrocardiography: comparison of magnetic and electric signal strengths. *Phys. Med. Biol.* **51** (2006) 145 - 151.

[14] M. Hämäläinen, R. Hari, R.J. Ilmoniemi, J. Knuutila and O.V. Lounasmaa. Magnetoencephalography-theory, instrumentation, and applications to noninvasive studies of the working human brain. *Rev. Mod. Phys.* **65** (1993) 413 - 497.

[15] H. Koch and W. Haberkorn. Magnetic field mapping of cardiac electrophysiological function. *Phil. Trans. R. Soc. Lond. A.* **359** (2001) 1287 - 1298.

[16] H. Koch. Recent advances in magnetocardiography. *J. Electrocardiol.* **37** (2004) 117 - 122.

[17] R. Fenici, D. Brisinda and A.M. Meloni. Clinical application of magnetocardiography. *Expert Rev. Mol. Diagn.* **5**(3) (2005) 291 - 313.

[18] D. Brisinda, G. Bottelli, C. Napolitano, S.G. Priori and R. Fenici. Magnetocardiographic findings and follow-up in an asymptomatic Brugada patient - Effects of Flecainide and of exercise tests. *Int. Congress Series.* **1300** (2007) 459 - 462.

[19] D. Kim, K. Kim, Y.H. Lee and H. Ahn. Detection of atrial arrhythmia in superconducting quantum interference device magnetocardiography; preliminary result of a totally-noninvasive localization method for atrial current mapping. *Interactive CardioVascular & Thoracic Surgery.* **6** (2007) 274 - 279.

[20] B. Hailer and P. Van Leeuwen. Clinical application of MCG in ischemic heart disease. *Int. Congress Series.* **1300** (2007) 741 - 744.

[21] R. Jurkko, V. Mäntynen, J.M. Tapanainen, J. Montonen, H. Väänänen, H. Parikka and L. Toivonen. Non-invasive detection of conduction pathways to left atrium using magnetocardiography: validation by intra-cardiac electroanatomic mapping. *Europace.* **11** (2009) 169 - 177.

[22] S. Yamada and I. Yamaguchi. Magnetocardiograms in Clinical Medicine: Unique Information on Cardiac Ischemia, Arrhythmias, and Fetal Diagnosis. *Internal Medicine.* **44** (2005) 1 19.

[23] I. Tavarozzi, S. Comani, C. Del Gratta, S. Di Luzio, G.L. Romani, D. Brisinda, S. Gallina, M. Zimarino, D. Brisinda, R. Fenici and R. De Caterina. Magnetocardiography: current status and perspectives - Part II: Clinical applications. *Ital. Heart J.* **3** (2002) 151 - 165.

[24] S. Achenbach, W. Moshage and K. Bachmann. Magnetocardiography: Clinical investigations with a biomagnetic multichannel system. *Physiol. Meas.* **14** (1993) 61 - 68.

[25] R. Fenici and D. Brisinda. Magnetocardiography provides non-invasive three-dimensional electroanatomical imaging of cardiac electrophysiology. *Anatol. J. Cardiol.* **7** (2007) 23 - 28.

[26] W. Haberkorn, U. Steinhoff, M. Burghoff, O. Kosch, A. Morguet and H. Koch. Pseudo current density maps of electrophysiological heart, nerve or brain function and their physical basis. *Biomagn. Res. Technol.* **4**:5 (2006).

[27] J. Sarvas. Basic mathematical and electromagnetic concepts of the biomagnetic inverse problem. *Phys. Med. Biol.* **32** (1987) 11 - 22.

[28] P.C. Hansen, M.L. Kringelbach and R. Salmelin. MEG: An Introduction to Methods. Oxford Univ. Press. New York. 2010.

[29] Z. Wu and N.E. Huang. Ensemble empirical mode decomposition method: A noise-assisted data analysis method. *Advances in Adaptive Data Analysis.* **1** (2009) 1 - 41.

2 Development of SQUID based MCG system

This chapter describes the Magnetocardiography (MCG) system that was developed as a part of the work carried out during the course of this thesis. This chapter also gives an account of the sensor calibration of the MCG system, evaluation of system noise and the standardized procedure adopted for carrying out MCG measurements on a human subject inside a magnetically shielded room.

2.1 MCG system set up

Fig.2.1 shows the block diagram of the MCG measurement set up developed at IGCAR that comprises of different modules (or units) such as Magnetically Shielded Room (MSR), Superconducting QUantum Interference Device (SQUID) gradiometers, cryostat, SQUID electronics, data acquisition system, etc. The same SQUID based MCG system can also be used for probing the functional activities of a limited cortical area by measuring the magnetic field associated with neuronal currents, which is known as magnetoencephalography (MEG). The system for the measurement of MCG/MEG signals started initially as a single channel system and was upgraded progressively to house 4, 13 and 37 SQUID channels respectively [1, 2]. Although, MCG and MEG systems share the common infrastructure such as the Magnetically Shielded Room for measurements, the flat bottom cryostat used for MCG limits the cortical area probed during the MEG measurements using this system. For MCG measurements, a flat bottom cryostat (with sensors arranged in a plane at the same level) is used to match the approximately flat profile of the surface of the thorax. On the other hand, for whole head MEG measurements, a concave bottom cryostat wherein the sensors are arranged on the surface of a helmet shaped sensor holder that has the profile of an average adult human head is preferred. Such an MEG cryostat with 90 channels has been assembled and is being commissioned. Here, we particularly discuss the features of the MCG system used for the work presented in this thesis..

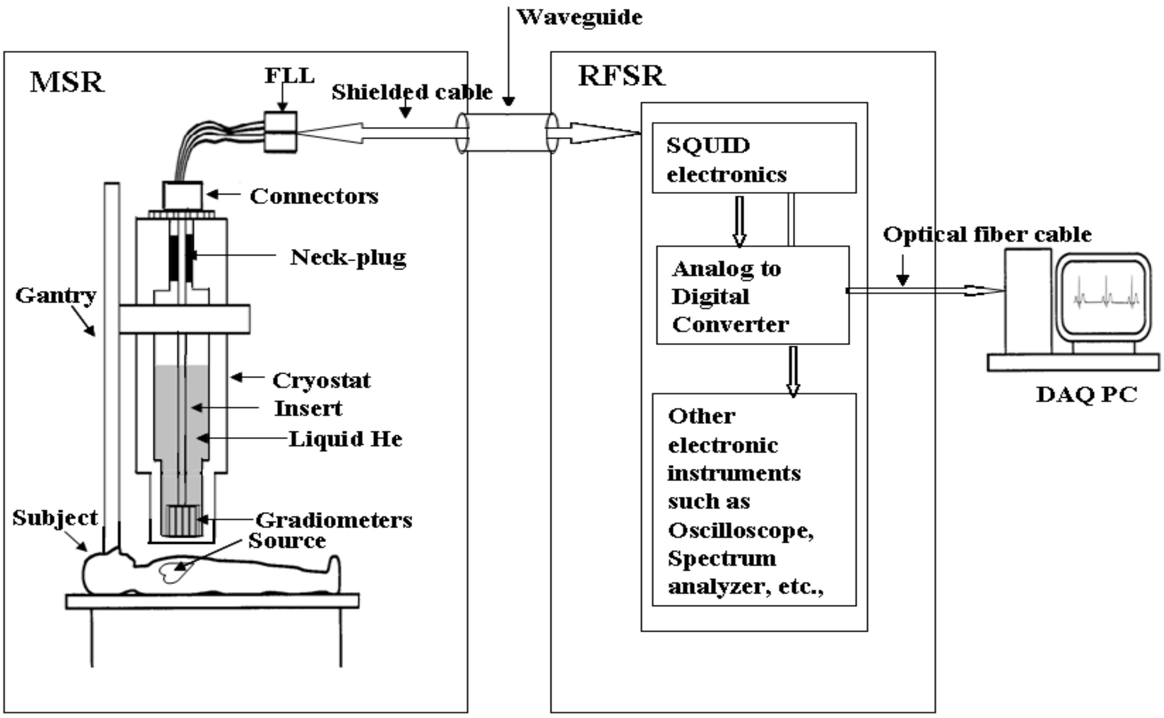

Figure 2.1: Block diagram of the MCG system used for the present work. The liquid helium cryostat housing an array of axial gradiometers immersed in liquid helium is located inside the Magnetically Shielded Room (MSR). The MCG signals originating from a human subject are detected by an array of axial gradiometers. The SQUID output voltage of each sensor is amplified and processed by Flux Locked Loop (FLL) electronics inside the MSR. The output signals are then taken to the radio frequency shielded room (RFSR), via waveguides connecting the MSR to RFSR, for digitization using analog-to-digital converter (ADC) cards. All the electronic equipments that require electrical Mains Power are housed inside the RFSR. The digitized data is transmitted via an optical fibre link for storage and graphical display on a server class computer located in the unshielded environment.

In the following, we give a brief account of the basic principles governing the operation of the SQUID sensor and the associated Flux Locked Loop (FLL) electronics used for the linearization of the periodic output of the SQUID.

2.2 SQUID as a magnetic field sensor

Biomagnetic signals ($10^{-12} - 10^{-15}$ T) are extremely weak [3]; they are four to six orders of magnitude weaker than the fluctuations in the earth's magnetic field (~2 nano-Tesla) and about six to seven orders of magnitude weaker than the earth's static magnetic field ($\sim$50 μT). The magnetic noise in an urban setting is generally caused by mains power line, vehicle movements, vibrations, etc., which may be in the range 1 nano-Tesla to 100 nano-Tesla depending on the site. The cardiac magnetic field (typically, $\sim$40 pT at the QRS peak) although relatively strong compared to the magnetic field produced by the human brain (100 fT - 2 pT), is completely masked by the ubiquitous ambient magnetic noise. In order to measure such a weak magnetic field associated with the biomagnetic sources, there are two essential prerequisites;

- The first is a magnetic field sensor, which is sufficiently sensitive to measure such extremely weak magnetic fields in the range of 100 femto-Tesla to 100 pico-Tesla.
- The second involves the reduction of the ambient magnetic noise to a level lower than the signal of interest.

The advent of the Superconducting QUantum Interference Device (SQUID) [4, 5] with a sensitivity of 1 to 10 femto-Tesla has therefore been crucial for the measurement and characterization of biomagnetic fields; indeed, these are the only sensors with adequate sensitivity to measure the biomagnetic fields.

Josephson effect and the flux quantization form the fundamental principles which govern the operation of the SQUID [4, 5]. The flux quantization implies that the magnetic flux threading through a closed superconducting loop is constrained to be an integral multiple of a flux quantum ($\Phi_0 = \frac{h}{2e}, 1\Phi_0 = 2.07 \times 10^{-15}$ Wb, where h is the Planck's constant and e is the elementary charge). Josephson effect refers to the establishment of phase coherence between two weakly coupled superconductors, which allows super-current to flow from one superconductor to other without developing any voltage. The weak coupling may be realized in practice by separating the two superconductors by a thin tunnel barrier of an insulating material. Such a structure is known as the Josephson junction, and the quantum mechanical tunneling of cooper pairs across the junction assists in the establishment of phase coherence between the two superconductors.

Depending on the operating principle, SQUID sensors are broadly classified into two categories: DC SQUID (which is biased with direct current) and RF SQUID (which uses a radio frequency current bias). The DC SQUID consists of a superconducting loop intercepted by two weak links whereas in the RF SQUID, the superconducting loop is intercepted by a single weak link. Both types of SQUID sensors act as magnetic flux to voltage transducers [4, 5] and their output voltage is a periodic function of the magnetic flux coupled to them with the periodicity of a flux quantum Φ_0. SQUID sensors based on Nb (having transition temperature, T_c ~9 K) are operated at liquid helium temperatures (4.2 K) and are known as low T_c SQUIDs (LTSC SQUID), while SQUID sensors based on high temperature superconductors such as YBCO ($T_c \sim$ 90 K) are operated at liquid nitrogen temperatures (77 K) and are known as high-T_c SQUIDs (HTSC SQUID) [4]. LTSC SQUID sensors offer superior sensitivities in the detection of magnetic field changes compared to the HTSC SQUIDs. We use low temperature DC SQUID (based on $Nb/AlO_x/Nb$ Josephson junctions) as a magnetic sensing device for MCG measurement and the working principle of the DC SQUID is briefly discussed in the following section.

2.2.1 Working Principle

In the absence of any external magnetic field, when a symmetric DC SQUID (which has two identical Josephson junctions) is biased with a DC current (I_b), the bias current I_b divides equally ($I_1 = I_2 = I_b/2$) into the two branches as shown in fig.2.2(a) and flows through the two Josephson junctions. The critical current (which represents the maximum current the SQUID sensor can support at zero voltage) of the SQUID in this case would be equal to $2I_c$, where I_c denotes the critical current of each Josephson junction. When a magnetic field (B) is applied perpendicular to the plane of the SQUID loop, a screening current (I_s) begins to circulate around the loop so as to produce the necessary magnetic flux required to satisfy the requirement of flux quantization [4, 5, 6].

$$\Phi_{tot} = \Phi_{ext} + LI_s = n\Phi_0 \tag{2.1}$$

Here Φ_{tot} is the total flux threading the SQUID loop, Φ_{ext} is the externally applied flux, I_s is the screening current induced by the applied flux, n is an integer which has to be chosen to minimize I_s, L is the inductance of the SQUID loop, and Φ_0 is the flux quantum. When the external applied flux is $n\Phi_0$, the screening current I_s induced is zero and when the external applied flux is $(n+\frac{1}{2})\Phi_0$, the induced screening current is $\pm(\Phi_0/2L)$. Thus, as the magnetic flux coupled to the SQUID is monotonically varied, the induced screening current varies periodically with the periodicity of Φ_0.

Since the induced current circulates around the SQUID loop in a clockwise or counterclockwise direction depending on the magnitude and direction of the applied magnetic field, the direction of the induced current I_s is the same as that of the bias current I_b in one branch of the SQUID while its direction is opposite to that of the bias current in the other branch, and this gives rise to a total current of $I_1(=\frac{I_b}{2}+I_s)$ in one branch while in other branch, it is $I_2(=\frac{I_b}{2}-I_s)$ (see fig.2.2(a)). A voltage appears across the junction as soon as the total current in any one of the

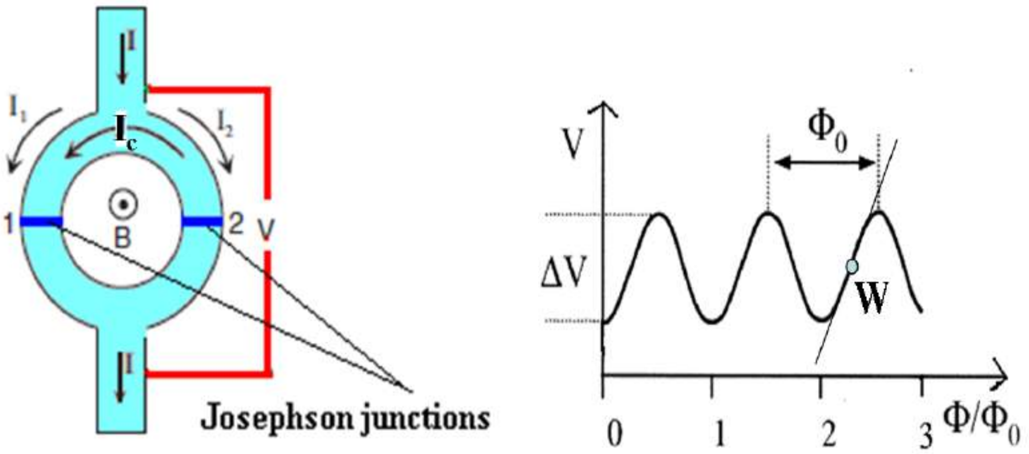

(a) (b)

Figure 2.2: (a) The schematic of the DC SQUID sensor (b) Periodic variation of the output voltage of the SQUID with the periodicity of a flux quantum (Φ_0), as the magnetic flux threading through the SQUID is monotonically varied (known as the $V-\Phi$ characteristic of SQUID) (adapted from [5]). Normally, SQUID is locked at the operating point W, and the effect of any applied magnetic flux is compensated by an equivalent feedback flux to lock the SQUID at the operating point. Any excursions around the operating point are limited to a very small region around W over which the $V-\Phi$ characteristic is linear with a flux-to-voltage transfer function of the bare SQUID sensor given by the slope ($V_\Phi = \partial V/\partial\Phi$).

two branches exceeds the critical current of the Josephson junction in that branch. As a result of this, the critical current of the SQUID reduces from $2I_c$ to $(2I_c-2I_s)$. The critical current of the SQUID is a periodic function of the externally applied magnetic flux and is given by [7].

$$I_{c_{max}}(\Phi_{ext}) = 2I_c|cos(\pi\frac{\Phi_{ext}}{\Phi_0})| \tag{2.2}$$

A voltage is developed across the SQUID when the SQUID is biased with DC current slightly larger than $2I_c$; this output voltage is a periodic function of external flux with the periodicity of a flux quantum Φ_0 (see fig.2.2(b)), as the magnetic field applied perpendicular to the plane of the SQUID loop [4, 5, 6] is varied. Thus SQUID can be termed as a magnetic flux to voltage transducer, giving a measurable output voltage for extremely small variations in the applied magnetic field, which are not measureable by any other sensor technology. The linearization of the periodic output voltage of the SQUID sensor is essential for most of the SQUID based measurements and is generally accomplished using a Flux Locked Loop (FLL) or current locked loop electronics [4, 8]. The discussion on the FLL, that we use in the MCG system, is given in the following section.

2.2.2 Flux Locked Loop (FLL) electronics

Several SQUID electronics readout schemes [5, 7, 9], such as direct readout, flux locked loop mode, etc., have been used for the purpose of linearizing the otherwise periodic flux-voltage characteristics of the bare SQUID sensor. In many such schemes, the SQUID often serves as a null detector in the feedback control system by keeping either the flux threading through the SQUID loop (in the flux locked mode) or the screening current flowing through the gradiometer (in the current-locked mode) constant [8]. The working point W on the $V-\Phi$ characteristic (see fig.2.2(b)) is maintained by cancelling the changes in the input flux or the screening current respectively using suitable feedback circuits in the SQUID electronics. In brief, the output voltage across the DC SQUID sensor resulting from the application of the signal flux is amplified, filtered and fed back as the compensating flux to ensure that the SQUID stays locked to the chosen working point. We now discuss in somewhat greater detail the operation of the SQUID in the Flux Locked Loop (FLL) mode [6], as shown in fig.2.3, which is extensively used for most of the DC SQUID readout systems (including the MCG system assembled during the course of this thesis).

Fig.2.3 shows the typical block diagram of FLL electronics [6] and this has been implemented in the present MCG system. An oscillator is used to pass a 100 kHz or higher frequency AC current with an adjustable amplitude through a modulation coil, which inductively couples a weak modulation flux of peak-to-peak amplitude upto $\sim \Phi_0/2$ into the SQUID loop. Depending on the flux-bias, the output voltage of the SQUID contains components at 100 kHz or 200 kHz or a mixture thereof with differing amplitudes of 100 kHz and 200 kHz components. A phase sensitive detector is arranged to detect the amplitude of 100 kHz component, which is indicative of the

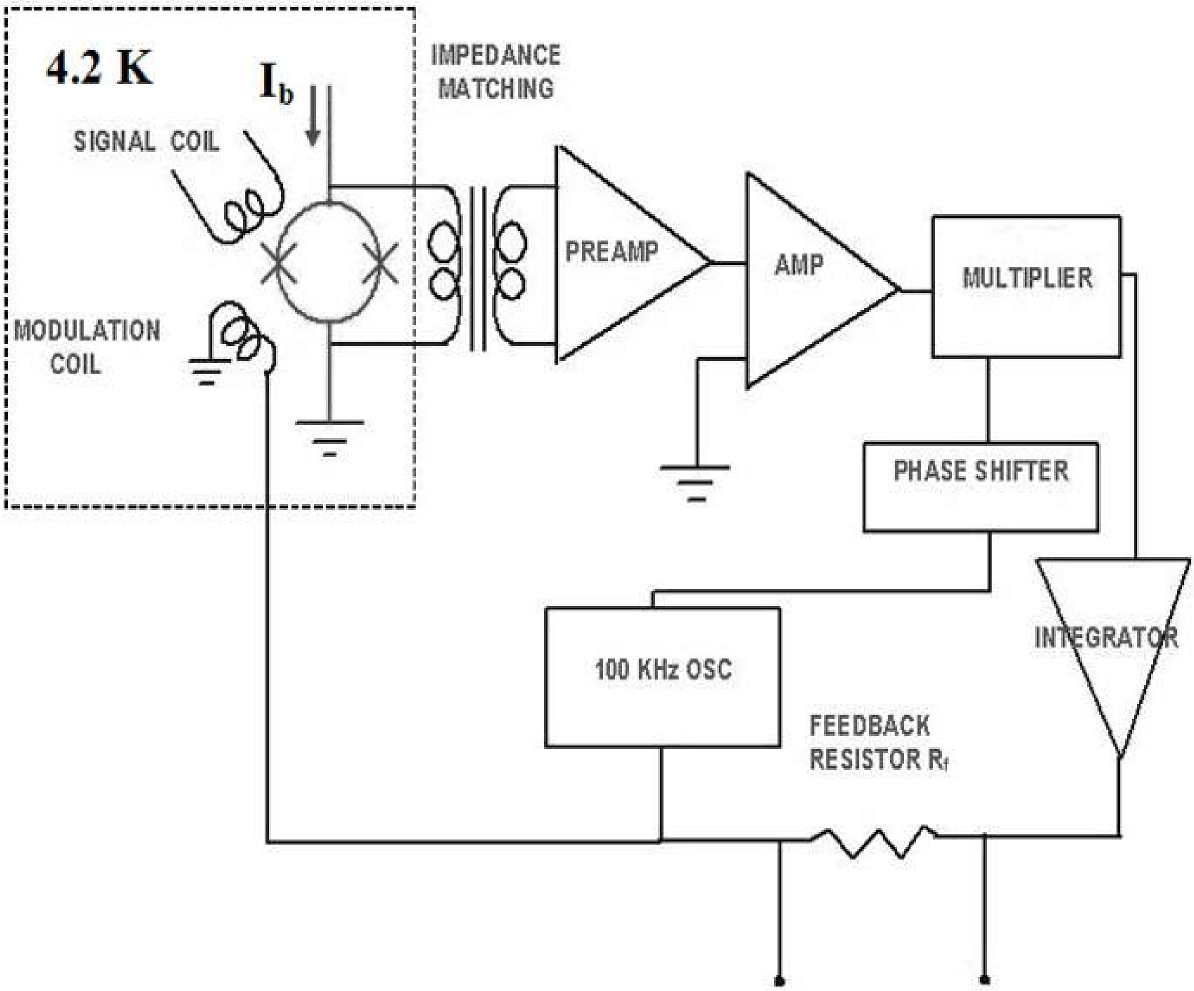

Figure 2.3: Typical schematic of the Flux Locked Loop (FLL) electronics circuit used for linearizing the periodic flux-to-voltage output response of the bare DC SQUID.

extent of deviation from the working point caused by the application of the input flux; the output of the phase sensitive detector is used to derive a feedback current to inject a compensating flux into the SQUID loop by passing the current through the feedback coil (and also the feedback resistor connected in series with the feedback coil). The output voltage across the feedback resistor (R_f) is a measure of the input flux signal, which is intended to be measured. The output voltage of the FLL is zero when no signal flux is coupled to the SQUID loop as SQUID remains at the working point W. When a signal flux is applied, however, there is a deviation from the working point and the FLL generates an output voltage which is proportional to the applied flux. The SQUID output voltage readout scheme based on flux locked loop electronics increases the dynamic range of measurement of magnetic flux, and also eliminates the low frequency noise arising from low frequency drifts in the junction critical currents/other SQUID parameters and $1/f$ noise from the preamplifiers etc. as the signal of interest is moved to frequencies (~100 kHz) above the $1/f$ threshold. Since the maximum feedback voltage is limited by the supply voltage (say, 12 V), the dynamic range is limited to the flux equivalent of the supply voltage at the selected gain of FLL and may be increased depending on the requirements by selecting a lower FLL gain, which may be easily tuned by changing the feedback resistor R_f, since it is given by the ratio R_f/M_f. The output voltage that appears across the feedback resistor R_f is proportional to the external flux intended to be measured and thus the periodic response of the bare SQUID is converted into a linear one, with a flux-to-voltage conversion factor independent of the open loop gain of the amplifier [10].

Although, the signal bandwidth is limited by the modulation frequency and is often substantially lower than the modulation frequency, this is not a serious limitation in biomagnetic investigations since a bandwidth of 1kHz is adequate for most of the applications. In the FLL mode, the total magnetic flux noise of the dc SQUID is given by [7],

$$S_{\Phi}^{\frac{1}{2}} = \sqrt{S_{\Phi,SQUID} + \frac{S_{V,AMPL}}{V_{\Phi}^2}} \tag{2.3}$$

where $S_{\Phi,SQUID}$ and $S_{V,AMPL}$ are the flux noise of the SQUID and voltage noise of the preamplifier respectively and $V_{\Phi}(= \partial V/\partial\Phi)$ is the flux-to-voltage transfer function of the bare SQUID. It may be noted that the decrease in the flux-to-voltage transfer function V_{Φ} deteriorates the attainable signal-to-noise ratio.

2.3 Reduction of ambient magnetic noise

Although SQUID sensors have the requisite sensitivity to detect the extremely weak biomagnetic fields, the ambient magnetic noise such as that associated with power line interference, vibrational noise, magnetic noise associated with vehicle movements etc., present at the site is orders of magnitude higher than the signal of interest and completely masks it. This poses a real difficulty in the measurement of biomagnetic signals, unless the ambient magnetic noise in the frequency bandwidth of interest (0-1000 Hz) is suppressed to a sufficiently low level.

Fig.2.4 indicates the strength of the typical biomagnetic signals of interest and compares it with the strength of the magnetic fields associated with some of the parasitic sources of ambient magnetic noise in the neighbourhood [7, 12]. In order to detect such extremely weak biomagnetic

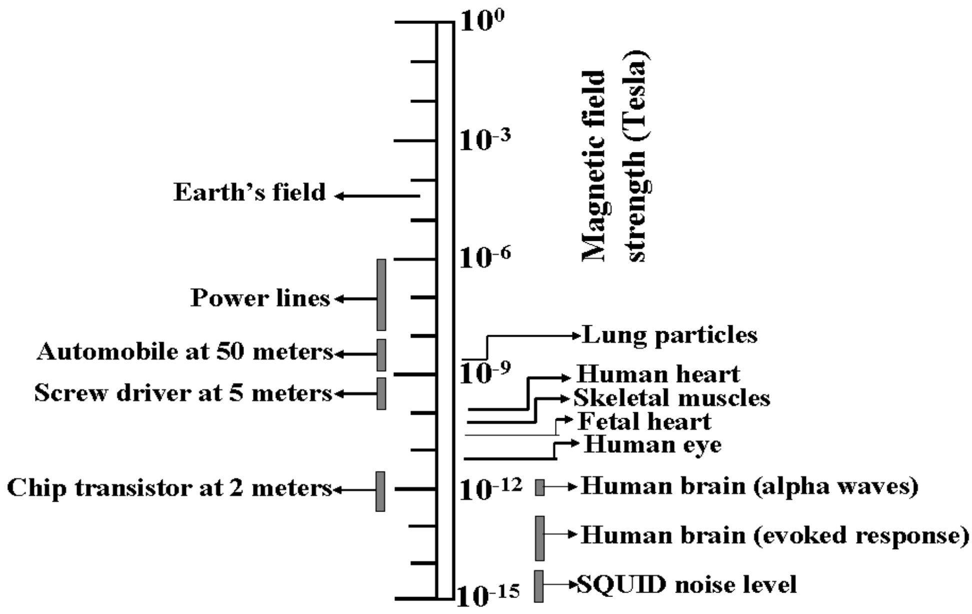

Figure 2.4: Schematic illustration of the strength of the magnetic fields originating from different sources (adapted from [12]). Since the biomagnetic fields of interest are much weaker compared to the parasitic ambient magnetic noise, it is essential to attenuate the ambient magnetic noise using some form of shielding in order to measure the signal of interest.

signals, it is therefore essential to attenuate all the parasitic sources of the ambient magnetic noise by using some form of shielding [7, 13] such as that provided by a Magnetically Shielded Room (MSR) and by using pick-up loops in the form of gradiometers [14] which further reduce the contribution of the residual magnetic noise present inside the MSR by discriminating against distant sources of magnetic noise which are expected to produce a nearly uniform field over the relatively small volume of the gradiometer; nearby sources, on the other hand, are expected to produce a non-uniform magnetic field over the volume of the gradiometer and, hence, get preferentially detected. Some research groups have tried to avoid the use of the expensive MSR for biomagnetic measurements by using higher order hardware gradiometers [14] or synthetic gradiometers [15] for measuring biomagnetic signals in an unshielded environment; however, measured signals in this case are generally of much poorer quality. In the following sections, we discuss the basics of MSR and the gradiometers that we employed for the reduction of ambient magnetic noise.

2.3.1 Magnetically Shielded Room (MSR)

As discussed earlier, Magnetically Shielded Room (MSR) is a prerequisite for biomagnetic measurements and is of crucial importance for all high quality measurements of biomagnetic signals [7, 11, 16]. MSR serves to attenuate the external ambient magnetic noise to a sufficiently low level so as to enable the SQUID sensors to measure the extremely weak biomagnetic signals, which are otherwise completely masked by the ambient magnetic noise. The magnetic shielding may be categorized into various types: ferromagnetic shielding using high permeability μ-metal (low frequency magnetic shielding), eddy current shielding using high conductivity aluminum or copper [7](high frequency magnetic shielding), active compensation [17] or superconducting magnetic shielding [18] etc. Here, we specifically describe the shielding configuration employed in our laboratory [19].

Our Magnetically Shielded Room (MSR), custom built by IMEDCO, Switzerland, inside which all the measurements reported in this thesis were carried out, has the internal dimensions 3m(width) $\times$ 4m(length) $\times$ 2.4m(height) and is constructed using two layers of ferromagnetic shielding (μ-metal) and two layers of eddy current shielding (aluminum) on each of the six sides. The outer aluminum layer is 4 mm thick, while the outer μ-metal layer is 2 mm thick. The inner aluminum layer is 8 mm thick while the inner μ-metal layer is 3 mm thick. The top panel of fig.2.5 shows the photograph of the MSR erected in our laboratory, at IGCAR, for biomagnetic measurements such as MCG and MEG. The principles of magnetic shielding provided by μ-metal and the aluminum layer may be explained [5, 11, 16] as follows:

High frequency magnetic noise is attenuated through the induction of eddy currents in the grounded high conductivity aluminum panels; by Lenz's law the eddy currents are induced in a direction so as to oppose the original magnetic field fluctuations. While this eddy current shielding is quite effective at high frequencies, it ceases to be effective at low frequencies owing to an inevitable increase in skin depth at low frequencies. For low frequency magnetic shielding, ferromagnetic materials such as μ-metal are used for the construction of the walls of MSR. Owing to the very high magnetic permeability of the μ-metal compared to air, it offers a path of low magnetic reluctance to the magnetic lines of force, and consequently, the magnetic field lines, which would have otherwise

(a)

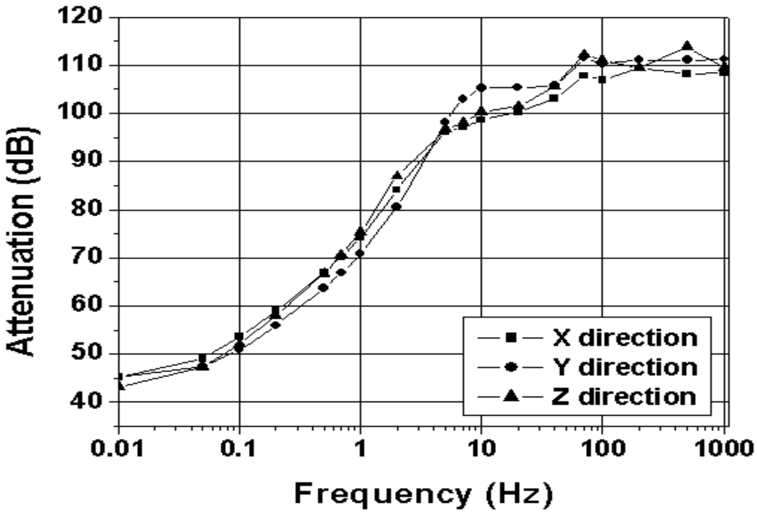

(b)

Figure 2.5: (a). The photograph of the magnetically shielded room (MSR) used for shielding against the external ambient magnetic noise. The bottom panel (b) shows the measured shielding factor of the MSR as a function of frequency for each of the three mutually orthogonal components of the magnetic field along X, Y and Z directions. It may be noted that the MSR provides a shielding factor of 70 dB at 1 Hz and 110 dB at 100 Hz and beyond.

passed through the shielded region, are bunched up and largely bypassed through the μ-metal walls of the MSR. Thus, in the region enclosed on all sides by the μ-metal walls, there is a considerable reduction (typically by a factor of 1000) in the density of magnetic lines of force. Magnetic shielding capability of a MSR may be quantified in terms of a Shielding Factor (S), which is taken to be the ratio of the external field (H_A) outside the MSR to the corresponding residual field (H_R) in the interior of the MSR; since the attenuation is frequency dependent, the Shielding Factor varies with frequency [20]. It is usual to express the Shielding Factor of a MSR on a logarithmic scale (dB) as per eq. 2.4:

$$S = 20log(\frac{H_A}{H_R}) \tag{2.4}$$

The bottom panel of fig.2.5 shows the shielding performance of the MSR as a function of frequency for all the three mutually orthogonal components of magnetic field. MSR provides a shielding factor of 70 dB at 1 Hz, which steadily improves to 110 dB at 100 Hz and beyond as seen in fig.2.5(b). MSR is equipped with a pneumatically operated door and four waveguides to route the SQUID cables without noise pick up from the ambient into an adjoining Radio Frequency Shielded Room (RFSR), which houses the electronic instrumentation.

2.3.2 SQUID Gradiometers

For coupling the signal of interest into the sensing area of the SQUID, a superconducting flux transformer is conventionally used to enhance the attainable field sensitivity. The superconducting flux transformer typically consists of either a single superconducting pickup loop (magnetometer) or a set of superconducting pick-up loops connected in opposition (gradiometer); it serves to sense the instantaneous net magnetic flux at its location and couple it to the input coil of the SQUID so that the SQUID sensor generates a proportional voltage output. Gradiometer type of pick-up loops have emerged as the preferred flux transformer design inside most MSRs which provide only a moderate level of attenuation of ambient magnetic noise (40 dB to 80 dB) and, despite their somewhat lower sensitivity for the detection of deeper sources, offer the advantage of additional attenuation of contributions arising from distant sources of noise.

In the gradiometer configuration, the coil which is closer to the source of interest is known as the pickup coil and the other coils which are away from the source are known as the compensation coils. The first order gradiometer is obtained by separating a pickup coil and a compensation coil by a distance called the baseline of the gradiometer. The gradiometers may be classified as axial or planar depending on the spatial gradient of the magnetic field sensed by them. The axial gradiometer measures the spatial gradient of the magnetic field along the axial direction perpendicular to the pick-up loop ($\partial B_z/\partial z$) and the off-diagonal or planar gradiometers measure the spatial gradient along the two orthogonal directions in the plane of the pick-up loop ($\partial B_z/\partial x, \partial B_z/\partial y$). Such gradiometers are commonly referred to as hardware gradiometers [7, 11], as distinct from synthetic gradiometers [14, 15, 16] which can be constructed electronically [13] or using software [15]. In the synthetic gradiometers, output signals of the lower order gradiometers are readout separately and subtracted. The different types of gradiometer configurations used conventionally in a SQUID based measuring set-up are illustrated in fig.2.6.

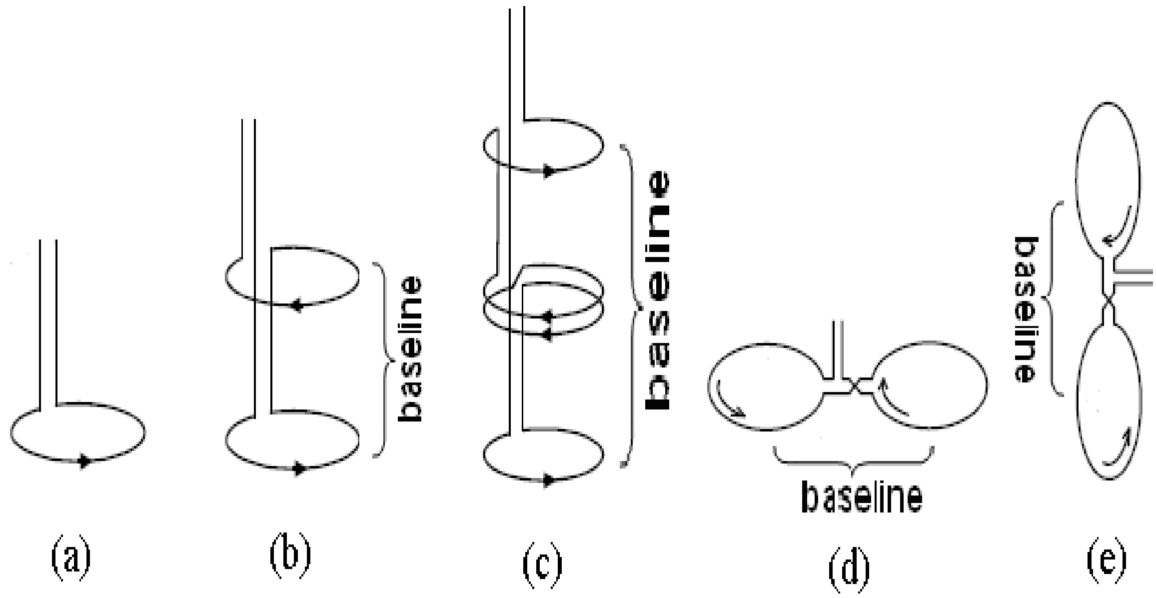

Figure 2.6: Schematic illustration of different types of pick-up coils used in a SQUID based measuring set-up (adapted from [4]). (a) to (e) show the different types of pick-up coils such as the magnetometer, first order axial gradiometer, second order axial gradiometer, planar gradiometer in the x-direction and planar gradiometer in the y-direction respectively. The magnetometer (a) measures the total magnetic field produced by both the signal of interest and any nearby as well as distant sources of magnetic noise. The gradiometers (b,c,d and e) measure the spatial gradient of the magnetic field ($\partial B_z/\partial z$, $\partial^2 B_z/\partial z^2$, $\partial B_z/\partial x$, $\partial B_z/\partial y$ respectively for (b)-(e)), and are relatively insensitive to distant sources of magnetic noise.

A first order axial gradiometer (used in our MCG system) consists of two equal radius loops of superconducting wire separated along the common axis by a distance b (baseline of the gradiometer, which is typically 5 cm in our system) and wound in opposition (one loop is clockwise while the other loop is anti-clockwise). Since the gradiometer basically senses the difference in magnetic flux threading through the two oppositely wound pick-up loops, the output of an ideally balanced gradiometer is zero if the applied magnetic field is uniform over the region occupied by the gradiometer. The variation of attenuation with the source distance R is governed by the parameter $(b/R)^2$ for a first order axial gradiometer. The immunity of the gradiometer to the external sources of ambient magnetic noise can be further improved by using higher order gradiometers which comprise of two or more lower order gradiometers connected in opposition (which are designed to sense higher order spatial derivatives of the magnetic field); indeed using second or higher order gradiometers, some research groups have succeeded in measurement of biomagnetic fields in an unshielded environment, although the quality of the measured data is relatively poor.

2.4 MCG system modules

As some of the modules of MCG system such as SQUID gradiometers, MSR, and FLL electronics have been already discussed in the earlier sections, we now describe the remaining modules of the MCG system in the subsequent sections.

2.4.1 MCG cryostat and the SQUID insert

The SQUID sensors have to be operated at a temperature well below the superconducting transition temperature of the superconducting materials used for their fabrication. Niobium has a superconducting transition temperature of $\sim$9 K, and hence, LTSC SQUID sensors based on niobium (that we use) are usually operated by immersing them in liquid helium, which has a boiling point of 4.2 K at the normal pressure of 1 atm., and, hence, provides a stable thermal environment for the operation of the SQUID sensor. For storing cryogenic liquids such as liquid helium or liquid nitrogen, it is necessary to use a cryostat or a dewar, which is specially designed to reduce heat leaks associated with thermal conduction, convection and radiation and achieve a reasonably low boil-off rate and consequently a longer holding time [5, 16, 20].

The MCG measurements are carried out inside a MSR housing the liquid helium cryostat in which SQUIDs are immersed in liquid helium in order to operate them at the temperature of 4.2 K. The cryostat is supported on a non-magnetic gantry, which allows the cryostat to be moved vertically, along the z-axis, in order to adjust its position above the thorax of the subject, depending on the experimental needs. As mentioned earlier in the section 2.1, the MCG system at IGCAR was progressively upgraded from a single channel system developed initially to the 37 channels system presently operational. Each SQUID channel consists of an axial gradiometer connected to a DC SQUID, a flux-locked-loop module, an Analog-to-Digital Converter (ADC) module to digitize the data, which is eventually displayed on a computer as the channel output as a function of time. While the individual modules (or units) of the MCG system are identical for MCG systems with different number of channels, there are variations in the overall size of the fiber reinforced plastic (FRP) cryostat, the number of SQUID gradiometers, inter-sensor spacing, the number of channels in the data acquisition system hardware etc. The increase in size of the cryostat is necessary to accommodate a larger number of sensors with a view to increase the area covered by the sensors over the surface of the thorax. Table 2.1 shows the features of the different MCG systems developed during the course of this thesis; in each system, different cryostats and sensor configurations were used. The photographs of the 4 channel and 13 channel MCG systems have been respectively shown in fig.2.7 and fig.2.8(a), while a dimensioned sketch of the 37 channel cryostat is shown in fig.2.9(a).

Table 2.1: The different MCG systems which were developed during the course of this thesis work. The cryostat used for the single channel system was also used for the four channel system. While the individual modules (or units) of the MCG system are identical for MCG systems with different number of channels, there are variations in the overall size of the fiber reinforced plastic (FRP) cryostat, the number of SQUID gradiometers, inter-sensor spacing, the number of data acquisition channels etc.

No. of channels	Liquid helium capacity (litres)	Warm-to-cold distance (mm)	Area covered on thorax (cm^2)	LHe boil-off rate (litres/day)	Geometry of sensor array	Inter-Sensor spacing (mm)
4	11.5	10	40	2	square	42
13	13	10	106	3	hexagonal	28
37	18	16	300	5	hexagonal	30

The single channel and four channel MCG systems were assembled in a 11.5 litre capacity liquid helium cryostat, while the 13 channel system and the 37 channel system were assembled in liquid helium cryostats having a capacity to hold 13 and 18 litres of liquid helium respectively. The

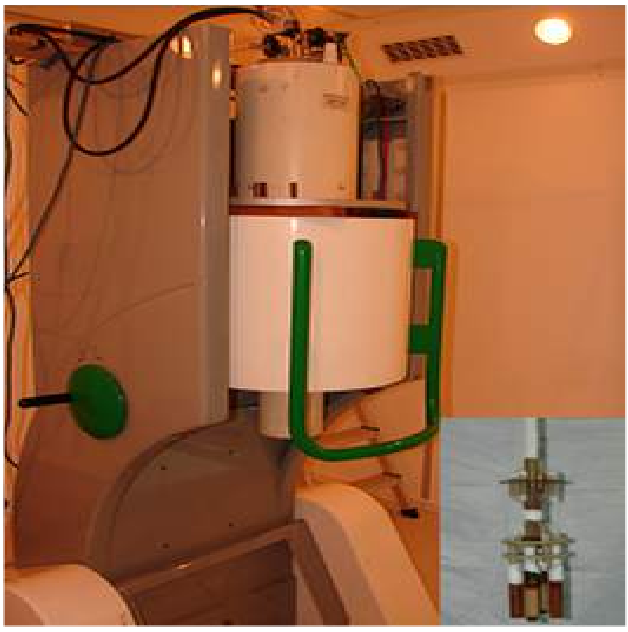

Figure 2.7: The photograph of the 4 channel MCG system developed during the course of this thesis. The inset in the photograph shows the SQUID holder in which the first order axial gradiometers are housed in a square lattice with an inter-sensor spacing of 42 mm.

(a)

(b)

Figure 2.8: (a) The photograph of the 13 channel MCG system developed during the course of this thesis. The inset in the photograph shows the SQUID holder in which the first order SQUID axial gradiometers are arranged in a hexagonal lattice with an inter-sensor spacing of 28 mm. (b) The photograph of the top view of the 13 channel cryostat showing the recesses (for locating the sensors) provided on the bottom plate of the liquid helium vessel of the cryostat, which serve to reduce the warm-to-cold distance.

holding time of liquid helium depends on the evaporation rate and the latter is listed for MCG systems with different number of channels. The geometrical configuration of the sensors and the inter-sensor spacing which eventually determine the coverage area are also different for the different MCG systems.

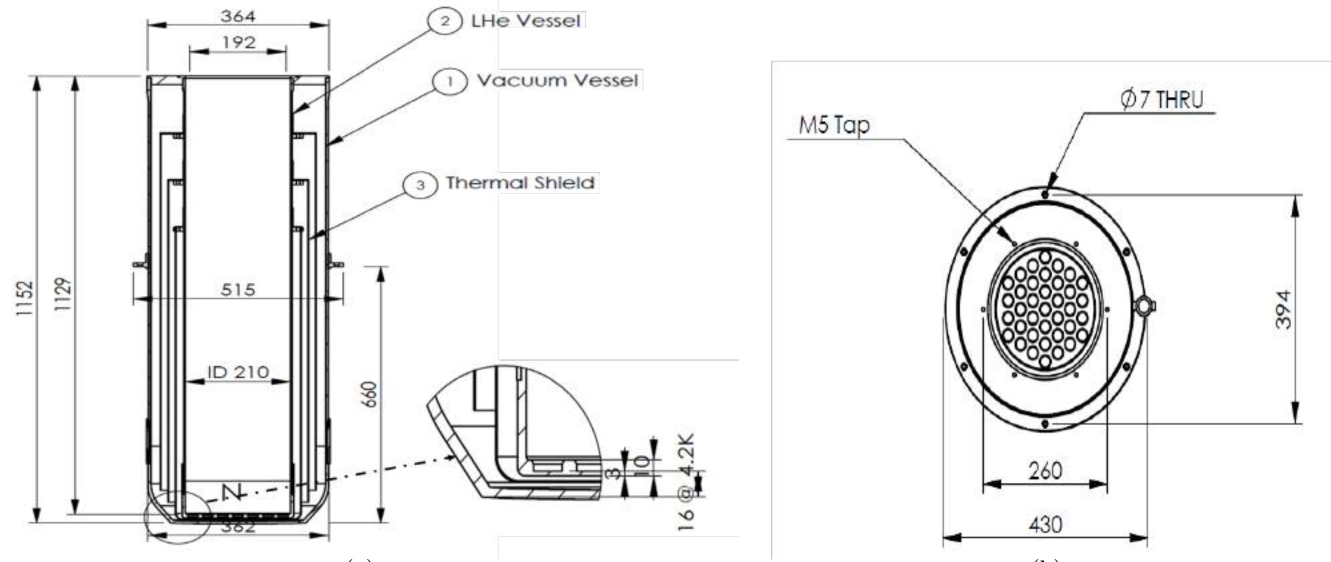

(a) (b)

Figure 2.9: (a) A dimensioned schematic sketch of the 37 channel MCG cryostat. The portion enclosed by the oval at the bottom of (a) is enlarged at right to show the warm-to-cold distance which is about 16 mm. (b) The sketch of the top view of the 37 channel cryostat showing the recesses (for locating the sensors) provided on the bottom plate of the liquid helium vessel of the cryostat, which serve to reduce the warm-to-cold distance.

It is important for a MCG cryostat to have the warm-to-cold distance as low as possible so that the pick-up coil of the sensors at liquid helium temperatures could be brought as close as possible to the skin surface of the subject, which has to be at room temperature. To ensure this, each cryostat is provided with recesses on the bottom plate of the liquid helium vessel at the locations of the sensors so that each sensor would be actually fitted to sit inside the appropriate recess so that the respective pick-up coil is as close as possible to skin surface. Fig.2.8(b) and 2.9(b) respectively show the photograph and sketch of the top view of the 13 channel and 37 channel cryostats. The recesses can be seen at the bottom flange of the liquid helium vessel of the cryostat which serve to reduce the warm-to-cold distance. Since the magnetic field decreases rapidly as one moves away from the source, it is important that the sensors are as close to the source as possible so that the measurements are performed with a relatively high signal-to-noise ratio. Reduction of the stand-off distance between the warm and cold surfaces of the cryostat to values $\sim$10 mm leads to an improved signal-to-noise ratio [19]. The warm-to-cold distance is about 10 mm for the four and thirteen channel cryostats whereas, for the 37 channel cryostat, it is about 16 mm.

With cryostats having a lower number of channels, it was necessary to perform sequential measurements in multiple configurations of sensor positions over the thorax in order to cover the thoracic area of interest for MCG measurements with consequent uncertainties in sensor positions as well as the considerably long time required to complete a typical MCG scan; when the 37 channel system became operational, it was possible to record the MCG signals simultaneously over an array of 37 points arranged on a hexagonal lattice covering a much larger area (300 cm^2) on the anterior surface of the thorax, and the need to perform sequential measurements was obviated, making the MCG scans relatively faster. With the 37 channel cryostat, sensor positions were also accurately known, leading to a much smaller uncertainty in the coordinates of the sensors during the MCG measurement, thereby enhancing the reproducibility [21] of the MCG data recorded during different experimental runs; consequently, the error in the reconstruction of the source from the measured MCG data is also considerably lower [22].

A suitable insert was designed for each cryostat along with a SQUID holder on which the SQUID modules, comprising of the wire wound axial gradiometer coupled to a SQUID sensor, were mounted. The SQUID insert fabricated from the fiber-reinforced plastic (FRP) material, which goes inside the cryostat, is equipped with a set of mounting plates to support the SQUID gradiometers at the bottom and the insulated LEMO electrical connectors (which are used to connect the SQUID electrical leads) at the top [19]. Each axial gradiometer consisted of two superconducting loops of 15 mm diameter separated by a baseline of 50 mm and was connected via superconducting contacts to the input coil which was integrated on-chip. The insert is also equipped with suitable radiation baffles in the neck region, to reduce the boil-off of liquid helium as a consequence of radiative heat leak. Fig.2.10 shows the photographs of the insert. The SQUID insert and the SQUID holder are designed in such a way that as the insert is carefully lowered into the cryostat, each gradiometer sits snugly into the corresponding 10 mm deep recess specially provided on the bottom flange of the liquid helium vessel in order to bring the pick up loop of the gradiometer as close to the source as possible.

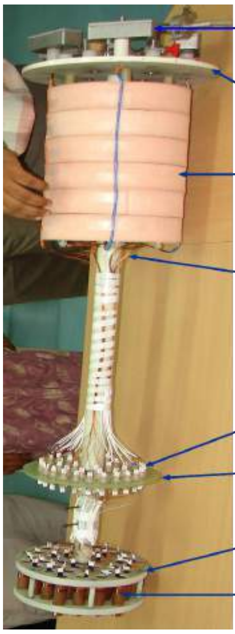

Figure 2.10: Photograph of the insert of the 37 channel MCG system which comprises of electrical connectors, SQUID holders, radiation baffles, mounting plates, etc. The first order axial gradiometers are mounted on the SQUID holder on a hexagonal lattice with inter-sensor spacing of 30 mm. This whole assembly is inserted inside the 37 channel cryostat.

2.4.2 SQUID electrical leads

An Electro-Static Discharge (ESD) safe work bench and ESD safe work-practices were used during the assembly of the SQUID sensors onto the SQUID insert, to avoid the risk of any possible damage to the tunnel barriers of the SQUID sensor by electrostatic discharge during mounting of the sensors and soldering of the electrical leads. Each SQUID module was wired with four twisted pairs of electrical leads, one pair each for bias current, flux modulation, SQUID output voltage and heater. The use of twisted pairs of electrical leads offers substantial immunity against the possible contamination of the signal by inductively coupled noise. The 40 SWG low resistive ($\sim 1\ \Omega m^{-1}$) copper wires were used for voltage and bias leads of the SQUID, while 40 SWG high resistive ($\sim 35\ \Omega m^{-1}$) manganin wires were used for the modulation and heater leads. The use of low resistive copper wires for the SQUID output voltage reduces the possibility of any signal drop across the electrical leads [23], especially when the relatively low output impedance of the SQUID sensor ($\sim 1\ \Omega$) is transformed using an impedance matching transformer to the values of source impedance at which the preamplifier yields the best noise performance. Use of low thermal conductivity manganin wires [23] for the other electrical leads (modulation and heater) serves to minimize the heat leak into the cryostat and consequently contributes to reducing the boil-off of liquid helium, thereby increasing the hold-time of the cryostat. The heater incorporated in the sensor is occasionally used in case magnetic flux is accidentally trapped in the form of vortices in the vicinity of the Josephson junctions constituting the SQUID sensor and consequently, the critical current of the SQUID as well as the modulation depth of the SQUID are reduced. In such a case, the heater may be activated for a few seconds to pass a current to raise the temperature of the SQUID sensor above the superconducting transition temperature T_c, in order to detrap the trapped flux and restore the critical current as well as the modulation depth to their original values, in the cool down of the SQUID on switching off the heater. The SQUID output voltage signals from all the channels, which are first routed to the intermediate electrical connectors on the mounting plate of the insert, are eventually brought out of the cryostat to the electrical connectors at the top of the insert by means of twisted pairs of electrical leads [2]. The battery powered modules comprising of preamplifier and the FLL electronics are located close to the top of the cryostat.

2.4.3 Radio Frequency Shielded Room (RFSR)

The linearized FLL output voltages from all the SQUID channels are routed via shielded cables through the waveguides connecting the MSR to an adjoining Radio Frequency Shielded Room (RFSR) [19], where necessary electronic instrumentation for analog-to-digital conversion (ADC) and data acquisition is located. The RFSR houses all the electronic instrumentation requiring the Mains Power such as the control units for the FLL, ADC modules to digitize the SQUID output voltage signal in each channel, function generators, oscilloscope, spectrum analyzer and other test and measuring instrumentation required during an experiment. Fig.2.11(a) shows a photograph of the RFSR and shows how it is connected to the MSR via four 100 mm diameter waveguides, while fig.2.11(b) shows a photograph of the electronic instrumentation housed inside the RFSR. The RFSR is constructed using 2 mm thick aluminum sheets of high electrical conductivity and provides a shielding factor of 100 dB at frequencies of 1 MHz and beyond [19].

The digitized voltage output data from all the SQUID channels is transmitted outside the RFSR over a fiber optic cable to a data acquisition system PC (DAQ-PC) located in the unshielded area through a port provided for this purpose on the rear wall of the RFSR. The fiber optic cable supports data transfer rates upto 75 Mbps and provides immunity against noise during the transmission of data to PC. The RFSR is equipped with ten signal line feedthrough filters, which

(a) (b)

Figure 2.11: (a). The photograph of the Radio Frequency Shielded Room (RFSR) coupled to the Magnetically Shielded Room via four waveguides (left panel). The right panel shows a view of the electronic instruments kept inside the RFSR. The RFSR provides high frequency shielding against electromagnetic interference with an attenuation factor of 100 dB at 1 MHz and beyond.

allows the passage of low level, low frequency signals inside RFSR, if desired by the user. All the electronic instruments inside the RFSR derive the Mains Power from a special isolation transformer, located far away from the MSR and RFSR, and the 220V, AC power line enters the RFSR via a filter.

2.4.4 Data Acquisition System

Based on the experimental requirements, the SQUID output voltage signal in each channel, which is proportional to the instantaneous axial gradient $\partial B_z/\partial z$ at the location of the gradiometer, may be low pass filtered with user desired cut-off frequency which may be set at any of the four values: 30 Hz, 100 Hz, 300 Hz and 1 kHz. An individual Delta-Sigma ADC is used for digitizing the SQUID output voltage in each channel with a 24 bit resolution at any user desired sampling rate upto 200 kHz [19]. However it may be noted that for most measurements a sampling rate of 1 kHz is adequate. The digitized data received over the optical fibre link is stored in a server PC, which is equipped with a custom-built data acquisition and display software. The software, based on a LABVIEW platform enables real-time graphical display of the output voltage of each channel as a function of time, with modules for low-pass, high-pass or band-pass filtering depending on the needs of the user. Besides allowing the data to be visualized in the time domain, the software enables investigations of the spectral content in the frequency domain and is also equipped with modules required for trigger based epoching and averaging to suppress uncorrelated noise, which are important for studies of evoked response in the context of MEG and for visualizing weak effects such as those associated with the activation of His bundle in Signal Averaged MCG (SAMCG). The channel output data, together with information on the experimental details and the sensor coordinates, is stored in the computer for subsequent off-line analysis.

2.5 Field gradient-to-Voltage Calibration for SQUID gradiometer

The SQUID system needs to be properly calibrated, prior to the biomagnetic measurements so that the measured SQUID output voltage may be expressed in terms of magnetic field, or magnetic field gradient using the calibration factor. For calibration, it is customary to relate the output voltage of the magnetometer or gradiometer to the value of the external magnetic field or field gradient produced by a known reference system. In general, the calibration factor is expressed as voltage/field or as voltage/field gradient. It is important that the calibration factor is accurately known in a multichannel biomagnetic system, since even a few percent error in calibration may result in appreciable errors in the source localization [22]. Although several calibration procedures have been reported in the literature [20, 24], we have adopted relatively a simple procedure for calibrating the output voltage of the SQUID sensors, which is found to be effective.

We used a large circular current carrying coil, encircling the tail of the Dewar, whose diameter was 20 times larger than the diameter of the superconducting gradiometer coil, which was used for sensing the magnetic field (or field gradient) and coupling it to the SQUID sensor as a proportional flux. In this arrangement, the coil is aligned to be along the gradiometer axis and its position is adjusted until a maximum voltage from the SQUID is obtained. From Biot-Savart's law, the vertical component of the magnetic field B_z at a distance z from the centre along the axis of the large circular coil is given by [24],

$$B_z(x = 0, y = 0, z) = \frac{\mu_0 N I a^2}{2(a^2 + z^2)^{3/2}} \tag{2.5}$$

where, N is the number of turns in the large circular coil, I is the current passed through the coil, a is the radius of the large circular coil and z is the distance between the sensor and the coil along the vertical axis. One can change either the amplitude of the current I by adjusting the level of the sinusoidal voltage in the signal generator or the vertical distance z by adjusting the height of the cryostat vertically to vary the input magnetic field values and the output voltage of the SQUID for the corresponding changes in the magnetic field are recorded. As the sensor used was a first order axial gradiometer, the first order derivative of B_z at the sensor position is evaluated and the observed SQUID output voltage is plotted against the known value of the field gradient $\partial B_z/\partial z$ as shown in fig.2.12. The slope of the calibration plot yields the calibration factor. For instance, we estimated the calibration factor for the first order axial gradiometer, with a loop diameter of 15 mm and a baseline of 50 mm, as 22.2 pT/cm/V.

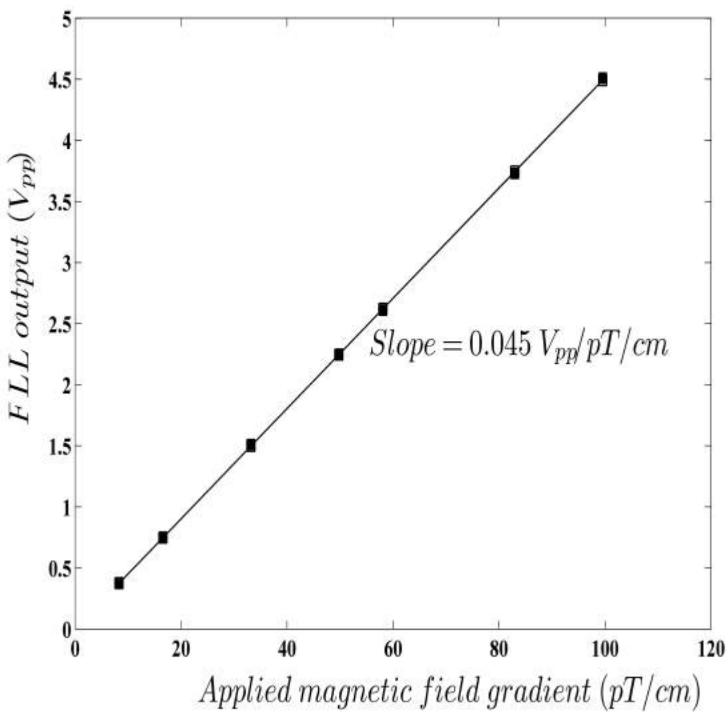

Figure 2.12: The flux-to-voltage calibration plot for a typical SQUID sensor. A known value of magnetic field (or field gradient) is presented to the sensor by passing a known amplitude of sinusoidally varying current through a large circular coil and the amplitude of the flux-locked-loop (FLL) output voltage for the corresponding magnetic field (or field gradient) is recorded. FLL output voltage is recorded for different values of applied magnetic field (or field gradient). The slope of the plot of FLL output as a function of applied magnetic field (or field gradient) is taken to be the calibration factor, which is used for converting the measured SQUID output voltage into the corresponding magnetic field (or field gradient).

2.6 Field gradient noise level in the SQUID system

It is imperative that, for a signal of interest to be measurable, its amplitude should be much larger than the sensitivity of the sensor used in the required bandwidth and the latter is limited by the intrinsic noise generated within the SQUID sensors and the extrinsic noise associated with electronics units, residual ambient magnetic noise, vibrations etc [20]. Hence, the background noise (the environmental noise in the absence of the subject) measured in the shielded room with an axial gradiometer must be lower than the signal of interest and this condition implies that white noise level of the sensor should not be more than several $fT_{rms}/cm/\sqrt{Hz}$ which represents the typical spectral density of the noise content in unit frequency bandwidth. The minimum noise level to be achieved depends on the amplitude of the signal to be measured. Fig.2.13(a) illustrates the typical variation of the spectral density of noise with frequency. The output noise of the SQUID comprises of a combination of white instrumental noise and the low frequency environmental noise. The distribution of system white noise for the 37 channel MCG system, above 10 Hz, is illustrated in fig.2.13(b). The average field gradient noise level measured, above 10 Hz, for the first order axial gradiometer with 15 mm loop diameter and 50 mm baseline was measured to be $\sim$ 2.2 $fT_{rms}/cm/\sqrt{Hz}$. The field gradient noise measured by the axial gradiometer could be converted

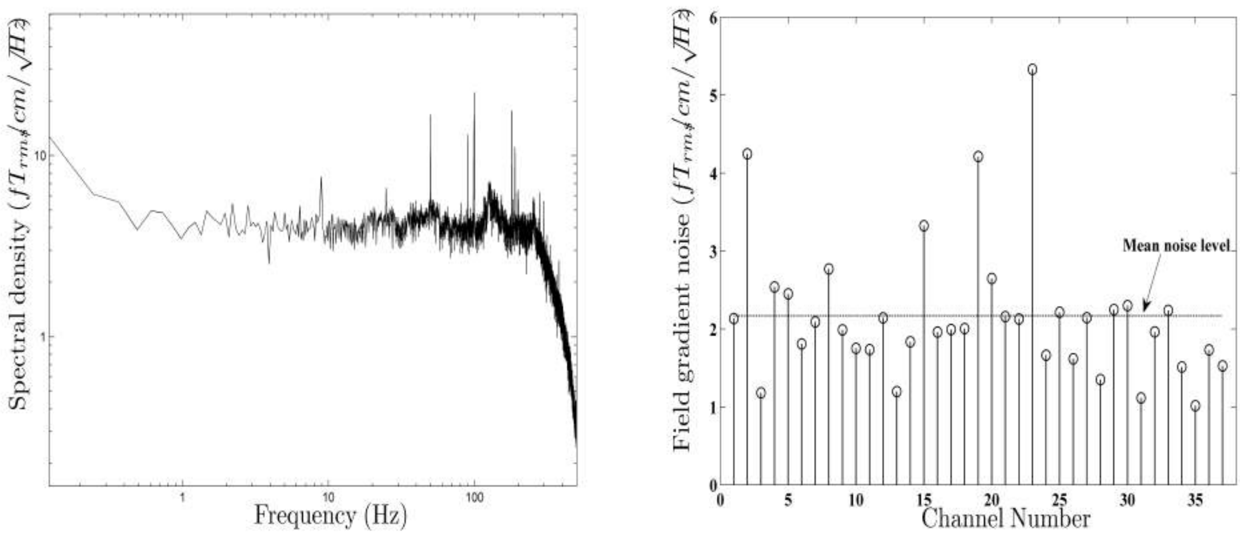

(a) (b)

Figure 2.13: (a) The spectral density of magnetic field noise for a typical SQUID sensor coupled to a first order axial gradiometer (with a baseline of 50 mm), measured with a low pass filter setting of 300 Hz. The low frequency noise peaks associated with vibration, and power line frequency of 50 Hz and its harmonics are seen. The right panel (b) shows the distribution of white noise level measured above 10 Hz, in the 37 channel SQUID based MCG system; the mean noise level ($\sim$ $2.2 fT_{rms}/cm/\sqrt{Hz}$ in field gradient noise or equivalently $\sim 11 fT_{rms}/\sqrt{Hz}$ in field noise) evaluated across all the channels is indicated by a horizontal line.

into an equivalent magnetic field noise by multiplying the field gradient noise by the baseline length of the gradiometer [20]. The average magnetic field noise is thus inferred to be $\sim 11\ fT_{rms}/\sqrt{Hz}$ for our MCG system.

2.7 MCG Measurement

Before MCG recording, the SQUID sensors are tuned to the correct bias current at which the maximum modulation depth is observed, which usually corresponds to the minimum output noise in the Flux Locked Loop (FLL) mode. The subject is instructed to remove and deposit all magnetic and metallic objects (including currency notes, which are usually printed with a magnetic ink). The subject is then taken inside the Magnetically Shielded Room (MSR), and is positioned under the cryostat in a supine position by appropriately raising or lowering the cryostat along the vertical axis. It is important to adjust the vertical position of the cryostat in such a way as to minimize the distance between the sensor plane and the subject to realize a high signal-to-noise ratio during the MCG measurements; nevertheless, care should be taken to ensure that the body of the subject does not touch the cryostat and that there is a clear gap between them. After the position of the subject under the cryostat is adjusted to align the central axis of the cryostat with reference to selected anatomical reference points on the thorax of the subject, the pneumatic door of the MSR is closed. The MCG signal is then recorded using the SQUID sensor array and is displayed on the server PC of the data acquisition system located in the unshielded environment. For recording, we typically use a sampling rate of 1 kHz in each channel with a low pass filter setting of 300 Hz and the FLL is usually operated at a gain setting of 5 V/Φ_0. Fig.2.14(a) shows a photograph of the MCG recording on a human subject in progress inside the MSR using the 37 channel MCG system; fig.2.14(b) shows the recorded MCG on the Data Acquisition Computer.

(a)

(b)

Figure 2.14: (a). Photograph representing the MCG measurement, using 37 channel MCG system on a human subject, in progress inside the MSR. The position of the subject and the cryostat are adjusted in such a way that the sensors are just above the anterior thoracic surface. The bottom panel (b) shows a screenshot of the recorded MCG on the Data Acquisition Computer. A few channels have been shown on an expanded scale in the ordinate for clarity.

2.8 MCG signal source analysis

The four channel SQUID system developed initially was used to record the magnetocardiograms on the subject's chest sequentially at a total of 36 locations on a 6 × 6 square lattice covering an area of 21 cm × 21 cm as indicated in fig.2.15. The spatial distance between the adjacent SQUID sensors was 4.2 cm. Fig.2.15 also shows the grid pattern of the measurement locations superimposed on a representation of the chest surface to indicate the measurement positions relative to the heart, which is schematically shown as inlay. The signal at each location was preprocessed (removing

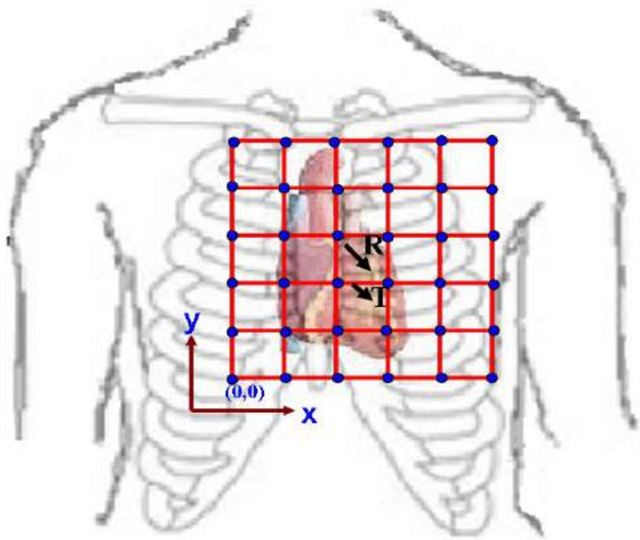

Figure 2.15: The two dimensional thoracic surface of a subject showing the location of the grid pattern (the jugular notch over the sternum provided the reference) used for the MCG measurement as well as other anatomical landmarks relative to the heart. The arrows represent the orientation of the respective dipoles obtained from a solution of the inverse problem at the instants of the R and T peaks.

breathing artifact and 50 Hz power line frequency) and averaged over a hundred cardiac cycles to improve the signal to noise ratio. The breathing artifact has been removed by using wavelet toolbox in MATLAB. The Daubechies (*db10*) wavelet was used with an appropriate user selectable level of decomposition to identify and eliminate the low frequency components such as breathing artifact (about 15 to 20 cycles/min) and baseline drift. The signal reconstructed was free of breathing artifact and baseline drift. Fig.2.16(a) shows the signal averaged MCG at the 36 locations and fig.2.16(b) shows the corresponding magnetic field map, which is the iso-field gradient contour map (MFM) constructed from the measured magnetic field gradient distribution at the instant of the

R-peak of the ventricular depolarization, for a typical subject. From the MFM, our objective is

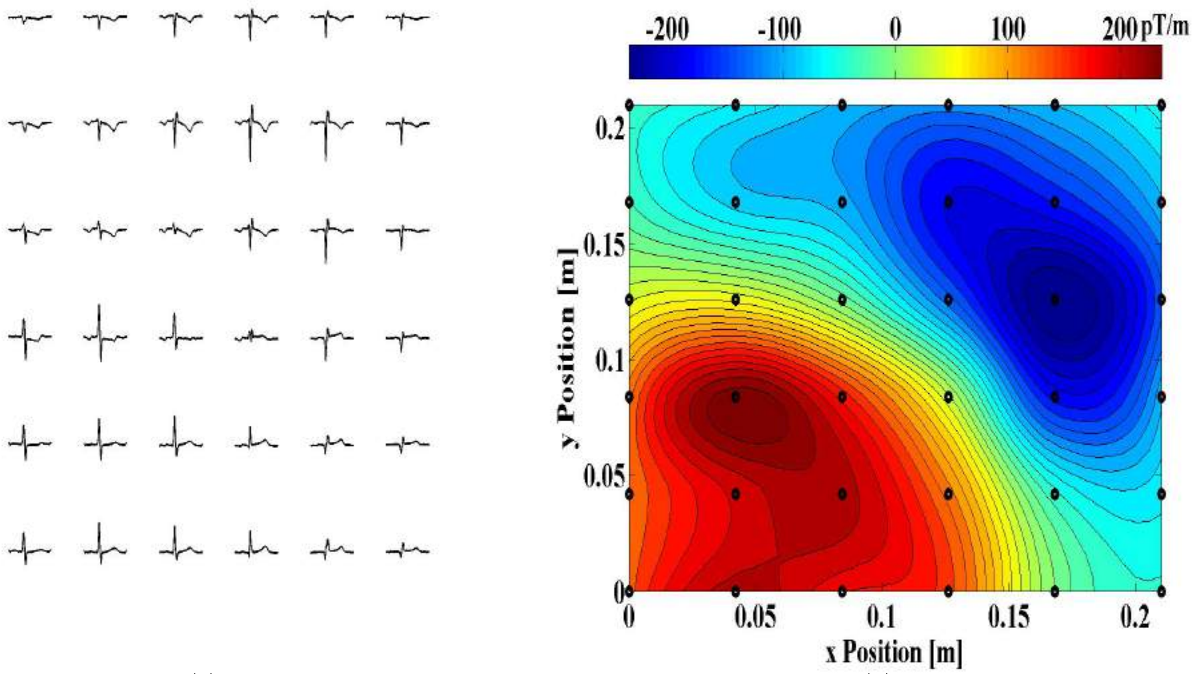

(a) (b)

Figure 2.16: (a) The signal averaged MCG over hundred cardiac cycles at the 36 locations, and (b) the MFM constructed at the instant of ventricular depolarization, the R-peak. The dots on the MFM represent the spatial locations of the sensors. The spatial distribution of signal averaged MCG in the lower left half shows the positive prominent R-peak while the upper right half shows negative prominent R-peak illustrating the approximately dipolar spatial variation of the cardiac magnetic field. The MFM on the right panel reveals a characteristic dipolar spatial variation, and the source (modeled as an equivalent current dipole) is expected to lie midway along the line joining the positive (red) and negative (blue) extremum. The depth of the dipole relative to the sensor plane may be empirically estimated by $d/\sqrt{2}$, where d is the distance between the two extrema.

to reconstruct the source parameters, which could account for the observed electrical activity of the heart, through a solution of the inverse problem. There are many algorithms (nonlinear least square optimization [10], MUSIC [25], simulated annealing [26], genetic algorithms [27], etc.) and cardiac source models (equivalent current dipole, multipole expansion model [28], etc.) which have been used by researchers to solve the inverse problem in the context of MCG. Here we have adopted the equivalent current dipole model (ECD) to represent the cardiac source and the inverse problem is solved by means of iterative nonlinear least square optimization described in chapter 4. The results and discussion of the data analysis are also presented in the fourth chapter.

As already noted, the use of a four channel system for experimental measurements imposes limitations on the possible accuracies in the positioning of the sensors exactly at the nodal points of the grid during the measurement of the MCG at each of the nine configurations. This problem could be circumvented if simultaneous measurements were made using a system with a larger number of channels and covering a larger area of the thorax. In view of this, subsequent studies have been carried out with 37 channel MCG system and also the advanced signal pre-processing methods such as ensemble empirical mode decomposition method (described in chapter 3) has been adopted for denoising since the conventional denoising methods like filtering, averaging, wavelet based denoising, etc. have some drawbacks which are discussed in the **third chapter**.

Bibliography

[1] K. Gireesan, C. Parasakthi, S. Sengottuvel, N. Mariyappa, Rajesh Patel, M.P.Janawadkar and T.S. Radhakrishnan. Establishment of 13 channel SQUID based MEG system for Studies in biomagnetism. *Indian J. Cryogenics.* **36** (2012) 169 - 172.

[2] C. Parasakthi, Rajesh Patel, S. Sengottuvel, N. Mariyappa, K. Gireesan, M.P. Janawadkar and T.S. Radhakrishnan. Establishment of 37 channel SQUID system for magnetocardiography. *AIP Conf. Proc.* **1447** (2012) 871 - 872.

[3] Y. Nakaya and H. Mori. Magnetocardiography. *Clin. Phys. Physiol. Meas.* **13** (1992) 191 - 229.

[4] A. Braginski and J. Clarke. "Introduction." In: The SQUID Handbook - Fundamentals and Technology of SQUIDs and SQUID Systems - Vol I. edited by J. Clarke and A.I. Braginski. Weinheim: *WILEY-VCH*, 2004, pp. 1 - 25.

[5] R.L. Fagaly. Superconducting quantum interference device instruments and applications. *Rev. Sci. Instrum.* **77** (2006) 101101; doi: 10.1063/1.2354545.

[6] M.P. Janawadkar, R. Baskaran, Rita Saha, K. Gireesan, R. Nagendran, L.S. Vaidhyanathan, J. Jayapandian and T.S. Radhakrishnan. SQUIDs Highly sensitive magnetic sensors. *Curr. Sci.* **77** (1999) 759 - 769.

[7] V. Pizzella, S.D. Penna, C.D. Gratta and G.L. Romani. SQUID systems for biomagnetic imaging. *Supercond. Sci. Technol.* **14** (2001) R79 - R114.

[8] G. Stroink, B. Hailer and P. Van Leeuwen. "Cardiomagnetism." In: Magnetism in Medicine, edited by W. Andrä and H. Nowak. Weinheim: *WILEY-VCH*, 2006, pp. 164 - 209.

[9] D. Drung and M. Mück. "SQUID Electronics." In: The SQUID Handbook - Fundamentals and Technology of SQUIDs and SQUID Systems - Vol I. edited by J. Clarke and A.I. Braginski. Weinheim: *WILEY-VCH*, 2004, pp. 127 - 170.

[10] M. Hämäläinen, R. Hari, R.J. Ilmoniemi, J. Knuutila and O.V. Lounasmaa. Magnetoencephalography-theory, instrumentation, and applications to noninvasive studies of the working human brain. *Rev. Mod. Phys.* **65** (1993) 413 - 497.

[11] S. J. Williamson and L. Kaufman. Biomagnetism. *J. Magnetism and Magnetic Materials.* **22** (1981) 129 - 201.

[12] Z. G. Ozdemir, O.A. Cataltepe and U. Onbasli. "Some Contemporary and Prospective Applications of High Temperature Superconductors." In: Applications of High-Tc Superconductivity, edited by A.M. Luiz. *InTech*, ISBN 978-953-307-308-8, 2011, pp. 15 - 44.

[13] K. Sternickel and A.I. Braginski. Biomagnetism using SQUIDs: status and perspectives. *Supercond. Sci. Technol.* **19** (2006) S160 - S171.

[14] J. Vrba. SQUID gradiometers in real environments. *NATO ASI Series.* **329** (1996) 117 - 178.

[15] J. Vrba, G. Haid, S. Lee, B. Taylor, A.A. Fife, P. Kubik, J. McCubbin and M.B. Burbank. Biomagnetometers for unshielded and well shielded environments. *Clin. Phys. Physiol. Meas.* **12** (1991) 81 - 86.

[16] J. Vrba and S.E. Robinson. Signal Processing in Magnetoencephalography. *METHODS.* **25** (2001) 249 - 271.

[17] W.A.M. Aarnink, P.J. Van Den Bosch, T.M. Roelofs, M. Verbiesen, H.J. Holland, H.J.M. ter Brake and H. Rogalla. Active noise compensation for multichannel magnetocardiography in an unshielded environment. *IEEE Trans. Appl. Supercond.* **5**(2) (1995) 2470 - 2473.

[18] H. Matsuba. "Magnetic Shielding by HT_c Superconductor." In: Advances in Superconductivity IV, edited by H. Hayakawa and N. Koshizuka. Japan: *Springer*, 1992, pp. 1055 - 1060 .

[19] M.P. Janawadkar, T.S. Radhakrishnan, K. Gireesan, C. Parasakthi, S. Sengottuvel, Rajesh

Patel, C.S. Sundar and Baldev Raj. SQUID - based measurement of biomagnetic fields. *Curr. Sci.* **99(1)** (2010) 36 - 45.

[20] C.P. Foley, M.N. Keene, H.J.M ter Brake and J. Vrba. "SQUID system issues." In: The SQUID Handbook - Fundamentals and Technology of SQUIDs and SQUID Systems - Vol I. edited by J. Clarke and A.I. Braginski. Weinheim: *WILEY-VCH*, 2004, pp. 251 - 355.

[21] H. Koch and W. Haberkorn. Magnetic field mapping of cardiac electrophysiological function. *Phil. Trans. R. Soc. Lond. A.* **359** (2001) 1287 - 1298.

[22] P.C. Ribeiro, S.J. Williamson and L. Kaufman. SQUID arrays for simultaneous magnetic measurements: calibration and source localization performance. *IEEE Trans. Biomed. Eng.* **35**(7) 551 - 560.

[23] N. Mariyappa, C. Parasakthi, S. Sengottuvel, Rajesh Patel, K. Gireesan, T.S. Radhakrishnan, M.P. Janawadkar and C.S. Sundar. Improving noise performance of the SQUID in the presence of high resistive leads. *AIP Conf. Proc.* **1447** (2012) 891 - 892.

[24] P.H. Ornelas, A.C. Bruno, C. Hall Barbosa, E. Andrade Lima and P. Costa Ribeiro. A survey of calibration procedures for SQUID gradiometers. *Supercond. Sci. Technol.* **16** (2003) 427 - 431.

[25] J.C. Mosher, P.S. Lewis and R.M. Leahy. Multiple dipole modeling and localization from spatio-temporal MEG data. *IEEE Trans. Biomed. Eng.* **39** (1992) 541 - 557.

[26] H. Haneishi, N. Ohyama, K. Sekihara and T. Honda. Multiple current dipole estimation using simulated annealing. *IEEE Trans. Biomed. Eng.* **41** (1994) 1004 - 1009.

[27] K. Uutela, M. Hämäläinen and R. Salmelin, Global optimization in the localization of neuromagnetic sources. *IEEE Trans. Biomed. Eng.* **45** (1998) 716 - 723.

[28] Wang Qian, Ma Ping, Lu Hong, Tang Xue-Zheng, Hua Ning and Tang Fa-Kuan. Inverse computation for cardiac sources using single current dipole and current multipole models. *Chinese Phys. B* **18** (2009) 5566 - 5574.

3 Pre-processing of MCG signal using EEMD

Following a discussion on various methods used for the pre-processing of magnetocardiography (MCG) data, this chapter presents a brief description of the Ensemble Empirical Mode Decomposition (EEMD) method and the detailed steps involved in the application of EEMD in the context of MCG signal denoising. The application of EEMD based method to eliminate the low and high frequency baseline drifts contained in the experimentally measured MCG data is elucidated. The EEMD based denoising method applied in the context of both simulated as well as experimental MCG data and a comparison of the EEMD based denoising method with other standard denoising methods used conventionally is presented. This chapter also includes the description of the method used by us for the non-invasive detection of the extremely weak His-bundle activity. The combined use of EEMD and Independent Component Analysis (ICA) to denoise the multichannel MCG data is described. The chapter concludes with the results of comparison of denoised multichannel MCG data by EEMD-ICA with those obtained by other techniques such as standalone ICA and wavelet enhanced ICA (wICA).

3.1 Brief Overview of Denoising Methods

As the ECG and MCG signals have analogous morphological features, the signal denoising methods applied for the preprocessing of the ECG data could be applied to the preprocessing of the MCG data as well. There are various signal processing tools based on the use of wavelet transform [1], Independent Component Analysis (ICA) [2] etc., and methods such as frequency domain filtering [3], Signal Space Projection (SSP) [4], etc., which have been widely used at the signal preprocessing stage. Each of these techniques, however, has its own advantages and disadvantages as discussed below.

Conventionally, filtering methods based on Fourier transform such as Finite Impulse Response (FIR), Infinite Impulse Response (IIR) [5, 6], etc., and averaging methods have been used for the enhancement of the signal-to-noise ratio (SNR) in the context of both ECG and MCG. If the signal is periodic, adequate suppression of uncorrelated noise may often be achieved by the **signal averaging** method [7], in which a large number of nominally identical cycles are aligned with respect to a chosen fiducial reference and are averaged. The uncorrelated random noise reduces by a factor of $\sqrt{N}$ as a result of signal averaging, where N is the number of cardiac cycles or beats. Signal averaging requires all the cardiac cycles to be nominally identical in the absence of random noise and the subtle but important inter-beat variations in the cardiac cycle could be lost in the process of averaging. The inter-beat variations such as heart rate variability would smear the weak signals such as those associated with the activity of the His bundle [8] unless the fiducial point is carefully chosen as discussed in the forthcoming section 3.10.

In **filtering**, different types of filter settings such as band-pass, low pass, notch (or band-stop) etc., are set by the user, based on the requirements of the bandwidth of the signal of interest. One could use conventional frequency domain filtering technique [3] if the signal and noise have separate bandwidths. The overlapping of the signal and noise in the frequency domain may, however, lead to the distortion in the signal when a filter attenuates the noise components; besides, this technique based on Fourier decomposition cannot be applied to the *nonlinear and non-stationary* signals. **Adaptive filtering** techniques [9, 10] use a separate set of reference channels to measure noise and use these measurements to estimate the noise present at the actual measurement channels. However, this technique requires provision of additional channels to serve exclusively as reference channels located in positions where they do not sense the signal of interest but still sample noise in a representative manner, and the reconstruction of noise at the actual measurement channels based on noise measured by reference channels is also prone to errors.

The application of **wavelet transform** in the signal processing domain is a well established and widely used technique in the context of both ECG and MCG [11]. The multi-resolution technique of wavelet transform provides the feasibility of producing time-frequency decomposition of the signal and allows a local scale dependent spectral analysis of individual features of the signal. This, in turn, paves the way for application of the technique to non-stationary signals such as transients, aperiodicity of the signal features etc. Wavelet transform method for signal denoising [11, 12, 13] is based on the use of a set of predefined basis functions, for instance Daubechies wavelet of some kind (say *db8*), to decompose the measured signals followed by suppression of components corresponding to noise or by thresholding the noise contents in the wavelet coefficients.

Techniques such as **Signal Space Projection** (SSP) [14] rely on the construction of projection operators to project out the contributions from the noise subspace. Statistical techniques such as **Independent Component Analysis** (ICA) [15, 16, 17, 18] seek to decompose the measured signals into statistically independent components by maximizing some measure of non-Gaussianity and reconstruct the signal by suppressing the components representing noise. All these methods have been extensively used in the literature for preprocessing of signals, including those of physiological origin such as ECG and MCG.

Recently, a new technique known as **Empirical Mode Decomposition** (EMD), has been proposed by Huang et al [19] for signal denoising [20, 21]. Unlike wavelet based techniques, EMD has the distinct advantage that it does not rely on a set of predefined basis functions and derives the basis functions, known as *Intrinsic Mode Functions* (IMFs), adaptively from the data set itself through a sifting process. This method is, however, prone to mode mixing, especially when the noise is present intermittently [22]. The mode mixing refers to the existence of different time scales in a single IMF or the same time scale in different IMFs. This mode mixing effect in the EMD is significantly reduced by a modified noise assisted data analysis method known as **Ensemble Empirical Mode Decomposition** method or EEMD [22, 23].

3.2 EEMD method for MCG signal pre-processing

We describe in detail the steps involved in the Ensemble Empirical Mode Decomposition (EEMD) algorithm, before presenting the results of denoising of MCG data using the EEMD method. In this section, we briefly describe the methods of Empirical Mode Decomposition (EMD) and the Ensemble Empirical Mode Decomposition (EEMD); the latter is an extended version of EMD and is designed to prevent the problem of mode mixing inherently present when EMD is applied to the experimental data. We also describe the Interval Thresholding (IT) method, which is useful for suppressing the discontinuities in the denoised version of the signal reconstructed using EEMD which often result when Direct Thresholding (DT) is used on the IMFs.

3.2.1 Empirical Mode Decomposition (EMD)

As already mentioned, the Empirical Mode Decomposition (EMD) decomposes the data into a set of Intrinsic Mode Functions (IMFs) through a sifting process [19] and the original signal of interest is reconstructed as a sum of selected IMFs. IMFs allow for the calculation of instantaneous frequency and amplitude through Hilbert spectral analysis [24], which is the energy-frequency-time spectrum. The following criteria have to be satisfied for a function to be designated as an IMF [19]: i) the number of extrema and the number of zero crossings must be equal or can differ at most by one, and ii) the mean value of the envelope defined by the local maxima and local minima at any location, must be zero (i.e., envelopes should be symmetric with respect to zero).

For a given data $x(t)$, the EMD procedure is as follows;

1. Identify all the local maxima and minima and connect all the maxima and minima with a cubic spline to respectively form an upper and a lower envelope.
2. The mean of the upper and lower envelope $m_1(t)$ is obtained and the difference,

$$h_1(t) = x(t) - m_1(t) \tag{3.1}$$

   is calculated.

3. If the difference $h_1(t)$ does not satisfy the criteria prescribed for an IMF, the above steps (1) and (2) are repeated until the envelopes are symmetric with respect to zero; the process is terminated depending on the value of a parameter SD defined by,

$$SD = \sum_{t=1}^{N} \frac{|h_{k-1}(t) - h_k(t)|^2}{h_{k-1}^2(t)} \tag{3.2}$$

4. The first IMF, $c_1(t)$ is obtained when the SD is smaller than a user defined threshold and the

residue is calculated as,

$$r_1(t) = x(t) - c_1(t) \tag{3.3}$$

5. Now the residue $r_1(t)$ is treated as the signal to be decomposed and the above steps are repeated to obtain $r_2(t), r_3(t), ..., r_m(t)$.

6. The above procedure stops when the residue $r_m(t)$ is either monotonic or a function with only one extremum.

The sum of the IMFs yields the original signal from which the decomposition was obtained. This can be represented as,

$$x(t) = \sum_{i=1}^{m-1} c_i(t) + r_m(t) \tag{3.4}$$

where, $c_i(t)$ is the i^{th} order IMF and $r_m(t)$ is the residue or the last IMF. The time scale analysis of EMD shows a progressive transition from the fine scales to the coarse scales as the order of IMF increases. EMD has been shown to act as a dyadic filter for various types of noise including both white and fractional Gaussian noise [25, 26, 27] and has been used for signal denoising by partial sum of selected IMFs. However, EMD is prone to mode mixing [22] in which two or more different time scales exist in a single IMF or two or more IMFs may have the same time scale.

3.2.2 Ensemble Empirical Mode Decomposition (EEMD)

To alleviate the problem of **mode mixing** inherent in the use of EMD, the Ensemble Empirical Mode Decomposition (EEMD) analysis was proposed by Wu and Huang [22]. In the EEMD, white noise, having the amplitude of a fraction (typically 0.1-0.4) of the standard deviation of the signal is added before performing empirical mode decomposition (EMD) to decompose the signal into Intrinsic Mode Functions (IMFs), in each trial, and the ensemble average of each IMF is taken over all the trials to represent the true IMFs. The noise added in each trial to prevent the mode mixing effect, tends to diminish by $\varepsilon_0/\sqrt{M}$, where, ε_0 is the noise amplitude and M is the number of ensemble averages, when ensemble averaged since no correlation exists among the noise introduced in different trials. The procedure for the EEMD analysis can be described as follows:

1. Add a finite amplitude of white noise to the targeted data and then decompose it into IMFs

using EMD.

$$\tilde{x_n}(t) = x(t) + \varepsilon_0 w_n(t) \tag{3.5}$$

where $\tilde{x_n}(t)$ is the signal after adding the white noise during the n^{th} trial, $x(t)$ is the targeted data, ε_0 is a scaling factor to be multiplied by the white noise at each trial, and $w_n(t)$ is the white noise added during the n^{th} trial.

2. Repeat the above step with different sets of white noise added over a large number of trials.

3. Find the mean of each IMF obtained in different trials to arrive at the final IMFs.

3.2.3 Mode mixing

As mentioned earlier, the mode mixing present in the EMD can be effectively reduced by the use of the noise assisted data analysis method, EEMD, which utilizes the uniformly distributed reference frame based on the white noise to enable the signals of similar scale to be collated together in a given IMF [22]. For instance, to demonstrate the mode-mixing effect in EMD and its reduction in EEMD, we have applied both these methods to the experimentally measured MCG data and the IMFs obtained are respectively shown in fig.3.1(a) and 3.1(b). The existence of mode mixing of two or more than two different time scales in a single IMF is indicated with a blue oval, while the existence of two different IMFs having same time scales is indicated with a red oval. This is further illustrated by performing the **Hilbert-Huang Transform** (HHT) [24], which computes the instantaneous frequency and energy content of the IMFs at each time sample. The results of Hilbert spectrum for a representative IMF (IMF5) obtained by EMD and EEMD are shown in fig.3.1(c) and (d) respectively. It may be noted that the Hilbert spectrum represents the time-frequency-energy spectrum and the level of energy is indicated in the color bar (red is maximum and blue is minimum) on the right in the fig.3.1(c) and (d).

It may also be noted that the mode corresponding to high energy, indicated with red, is confined to a narrow frequency bandwidth in the IMF obtained by EEMD. We know that the EEMD acts as a dyadic filter bank structure for Gaussian noise [26] and there will be a partial overlap of the frequency bandwidth of the adjacent order of IMFs from low to high order. This partial overlapping of the frequency bandwidth is the reason for the spread of other low energy

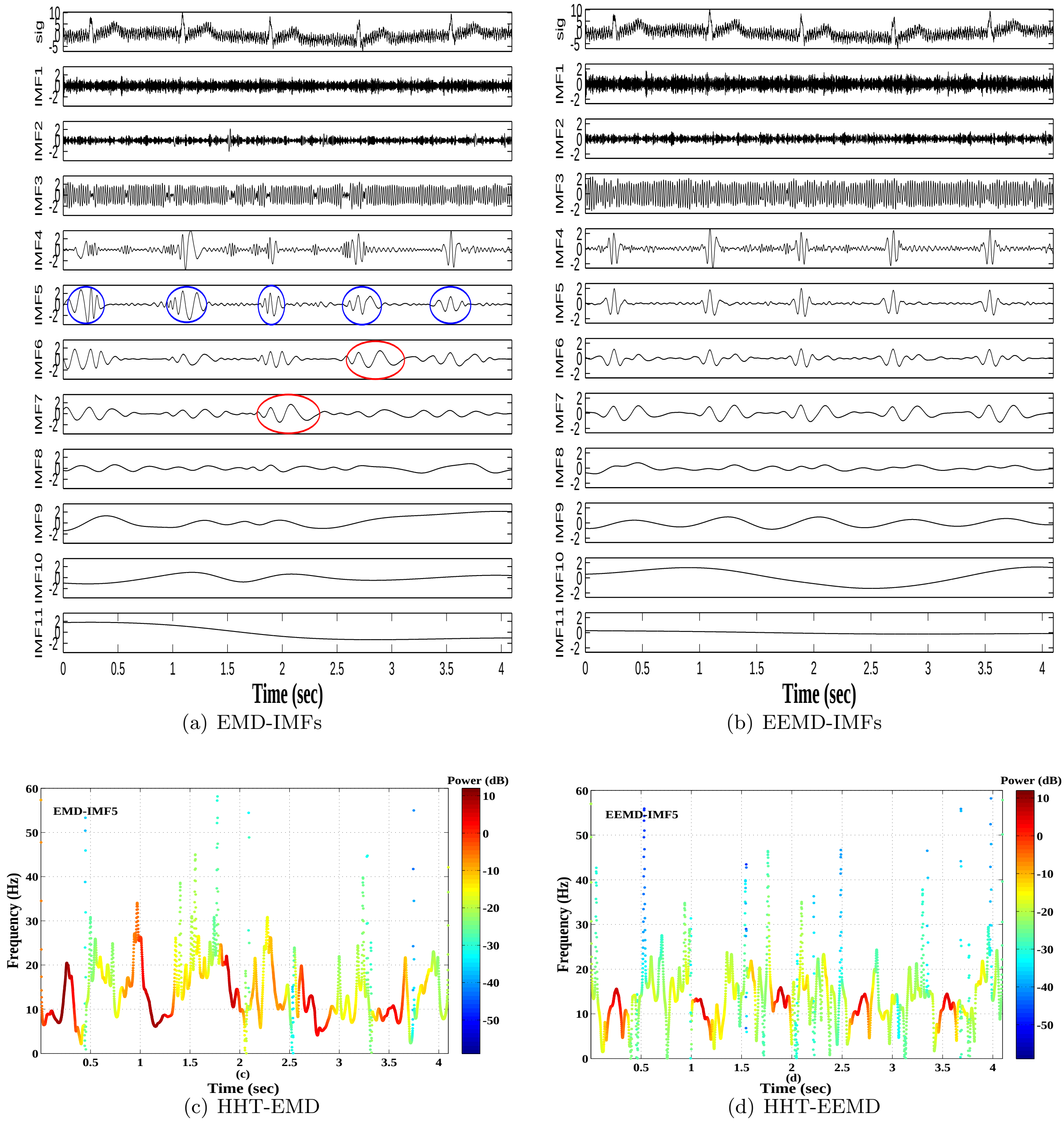

(a) EMD-IMFs

(b) EEMD-IMFs

(c) HHT-EMD

(d) HHT-EEMD

Figure 3.1: A comparison of the IMFs obtained from (a) EMD and (b) EEMD. The top panels in both (a) and (b) show the measured MCG signal from which the decomposition is obtained. The y-axis is magnetic field gradient (pT/cm). The mode mixing effect discussed in section 3.2.3 is indicated with red and blue ovals, in the left panel. This is greatly reduced on application of EEMD as seen in (b). The bottom panels (c) and (d) show Hilbert-Huang spectra, for a representative IMF (IMF5). The color bar indicates the energy level of the IMF samples. It may be noted that the high energy samples, indicated in red color, which constitute the dominant mode, have a limited frequency bandwidth in EEMD-IMF (right panel (d)) whereas they are much more dispersed along the frequency scale in the EMD-IMF (left panel (c)). This clearly illustrates the reduction of mode mixing in the IMFs obtained from the EEMD when compared with those obtained from the EMD.

frequency components seen in the Hilbert-Huang spectrum of the IMF. This clearly shows that there is a significant reduction of mode mixing of disparate scales in fig.3.1(d) (for EEMD-IMF) as compared to fig.3.1(c) (for EMD-IMF) demonstrating a key advantage of the EEMD technique over EMD. The algorithm for EMD [25, 27] and EEMD was implemented in **MATLAB** (in a PC configuration comprising Intel(R) Core(TM)2 Duo CPU with a speed of 3 GHz and 1.96 GB RAM capacity).

3.2.4 Noise Amplitude

One of the crucial issue in the EEMD method, to prevent mode mixing, is the amplitude of noise (ε_0) added. The scaling factor ε_0 (in Eq. 3.5) should be **neither too small nor too large** [28]. It has been reported [22] that the optimum amplitude of the noise to be added is in the range of 0.1-0.4 times the standard deviation of the signal. However, in some cases where the noise amplitude is larger than the amplitude of the signal to be decomposed, this prescription fails to achieve the prevention of mode mixing [28] and reduction of noise in the reconstructed signal in a relatively small number of trials. If the amplitude of the added noise is too low, it would not be sufficient for preventing mode mixing and different timescales present in the signal may not separate when the signal is decomposed into IMFs. If the amplitude of added noise is too high, the number of ensemble averages required may be too large for a reasonable suppression of noise in the ensemble averaged IMFs. The amplitude of the added noise has, therefore, to be optimal in the sense of being just sufficient to prevent mode mixing. It is also imperative to keep in mind that the added noise should not distort the signal integrity when it is reconstructed back from the linear combination of all the IMFs. Hence, it is essential that the level of noise amplitude ε_0 is carefully chosen so as to ensure the prevention of mode mixing and the suppression of added noise with a small number of ensemble averages with a view to reduce the computational complexity; it is also essential that the signal integrity is maintained with the lowest level of residual noise, a part of which may owe its origin to the noise added during the implementation of the EEMD algorithm. Thus there is a trade-off between the computational efficiency (based on the number of ensemble averages taken) and the signal-to-noise ratio (SNR) finally achieved (based on residual noise in the IMFs). Desire for a high SNR inevitably requires an increase in the computational burden. In practice, it is important to target a SNR which can be achieved with a reasonable computational burden.

In view of the reasons stated above, we introduce an **alternative strategy**, arrived at by investigating a large number of various types of input signals, where the scaling factor (ε_0) for the noise amplitude was successively taken to be related to the standard deviation of the first, second and third order time derivative of the input signal, as given in eq.3.6. In these investigations, the noise amplitude was chosen to be related to the standard deviation of the time derivative of the signal $x(t)$ as,

$$\varepsilon_0 = \frac{F}{f_s^n} * \sigma(\frac{d^n x(t)}{dt^n}) \tag{3.6}$$

where, n is the order of the derivative, f_s is the sampling frequency of the signal, used for normalizing to unit bandwidth of the signal, and F is the scaling factor. The conventionally used noise amplitude scaling factor can be obtained from Eq.3.6 when $n = 0$.

In prior art, the selection of scaling factor 0.1 to 0.4 (times the standard deviation of the signal) seems to have been obtained by iteratively analysing the data with different scales [22]. This will eventually lead to an additional computational burden when EEMD is used. In order to increase the computational efficiency, **we introduce a scaling factor F** which adjusts the noise level to the lowest value which is just sufficient to prevent the mode mixing effect and also consequently reduces the number of ensemble averages required. The scaling factor F is computed from the following equation,

$$F = \frac{||x(t)||_2}{\sqrt{x(t)_{min}^2 + x(t)_{max}^2}} \times \sqrt{\frac{\sqrt{2}}{N}} \tag{3.7}$$

where, $x(t)_{min}$ is the minimum value of the signal, $x(t)_{max}$ is the maximum value of the signal and N is the length of the data. As the scaling factor F is obtained from the signal itself, the iterative procedure for selection of scaling factor is avoided and the computational burden associated with the application of EEMD is reduced. Following various trials, the choice of $n = 2$ (second order derivative) in Eq.3.6 was found to work quite well in practice, in all cases investigated.

We also observe that the addition of the noise to the signal makes the decomposition level (number of IMFs) to vary slightly as the spectral distribution in the noise varies, even though the noise amplitude was kept fixed in all trials. The optimum decomposition level is determined by initially subjecting the observed signal with the addition of noise, to undergo decomposition for as few as ten trials. With the level of decomposition fixed from this exercise, the noise distributions, which produce the same level of decomposition in different trials are chosen and the resulting IMFs are averaged over a finite number of trials.

In fig.3.2, we compare the relative performance of the two different choices of noise amplitudes i) derived from **standard deviation of the second order derivative** of the signal as computed from Eq.3.6 when $n = 2$ (hereafter referred to as SDS) and ii) 0.2 times the standard deviation of the signal (hereafter referred to as P2S), for the ensemble averaging of 100 trials. It may be noted from the inset of fig.3.2(a) that the **signal reconstructed back from all the IMFs produced by the EEMD** with the conventional choice of noise amplitude P2S (blue line) shows significant distortion of the original signal (black line) while the signal reconstructed from IMFs derived from EEMD with the choice of noise amplitude derived from SDS almost merges with the original signal, showing that the signal integrity is not compromised when noise amplitude derived from SDS is used during the implementation of EEMD. Further, it is clearly seen (from fig.3.2(b)) that a far smaller (residual) error ensues when the noise amplitude is selected according to standard deviation of the second order derivative signal (SDS).

The choice of noise amplitude that is derived from SDS does not require any iterative procedures unlike the conventional choice of noise amplitudes which involves iterative steps to find the optimal level of noise amplitude and requires large number of ensemble averages, which eventually enhances the computational burden and complexity. Hence, for all the investigations on signal denoising using EEMD discussed hereafter, we fix the maximum number of trials for the ensemble average to be 100, as this was found to be sufficient in most cases, and the noise amplitude was derived from the standard deviation of the second order derivative of the signal (SDS) (refer Eq.3.6 when n=2).

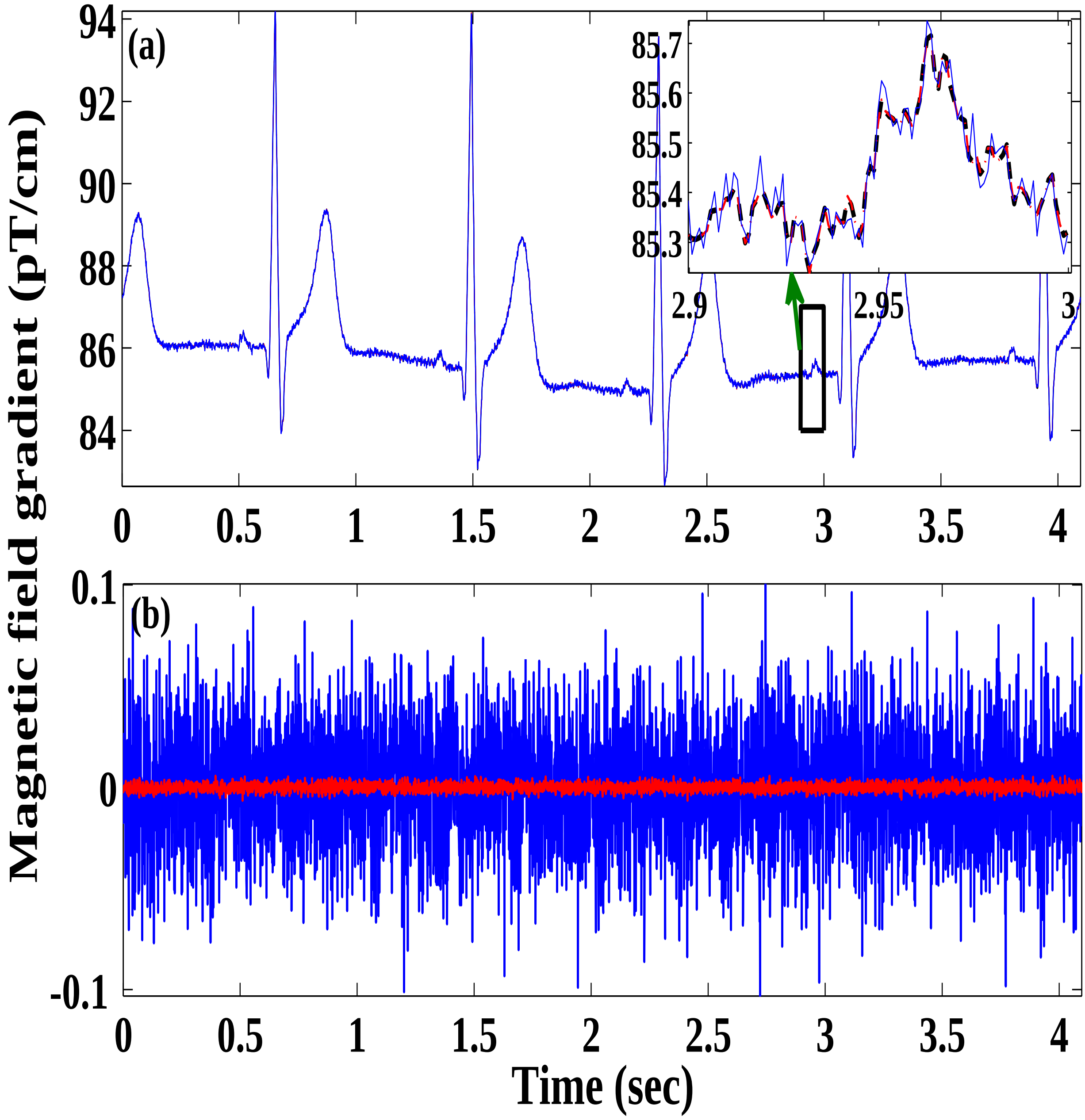

Figure 3.2: (a) Reconstructed signals from all the IMFs of the EEMD analysis for the two different noise amplitudes (0.2 times the standard deviation of the signal (P2S) (blue) and standard deviation of the second order derivative of the signal (SDS) (red)) are superposed with the original signal (black). The inset shows the expanded section of the rectangular window marked to indicate the signal reproducibility after reconstruction. It is seen that the signal reconstructed using SDS (red) is indistinguishable from the original signal (black) while that using P2S (blue) shows a deviation. (b) The error in reconstruction (difference between the original signal and reconstructed signals) for the two different noise amplitudes, P2S (blue) and SDS (red). The noise amplitude derived from SDS (red) is seen to preserve the signal integrity with a much reduced error as compared to the noise amplitude derived from P2S (blue). To achieve the same level of residual noise as in SDS (red), the number of ensemble averages has to be increased to ∼500 in the case of P2S, which substantially increases the computational burden.

3.3 EEMD Threshold based denoising

As already mentioned, **conventionally, the EMD or EEMD based denoising method reconstructs the signal from a partial sum of selected IMFs** [27, 29], especially those which have characteristic energies different compared to those of the first order IMF. The first order IMF (high frequency component) is generally expected to consist wholly of noise while the rest of the IMFs may contain noise or signal depending on the results of a statistical test (based on the empirical energy model [29]) with respect to the first order IMF [27, 29]. The IMFs which have characteristic energies similar to the first IMF (noise-only case) will be usually discarded and the rest of the IMFs are combined to obtain the denoised signal. However, in practice, the first order IMF may not always be a noise-only component. Also, in the partial sum of IMFs, there may be a possibility of excluding the high energy high frequency content of the signal of interest or a possibility of including the unwanted low energy high frequency oscillations in the signal of interest. With a view to avoid any loss of information in the high energy part of high frequency content and to avoid the possible addition of the low energy part of the high frequency content in the signal of interest, **we propose to use the thresholding based denoising** method.

The process of discriminating between the signal and noise with a (user-defined or computed) preset value or threshold is called thresholding. During the thresholding operation, the low energy IMF sample, which is below a predefined scale (or threshold) is set to zero since it is taken to be associated with noise, while the large energy IMF sample which is above the predefined threshold is retained since it is taken to be associated with the signal. In this way, by performing a thresholding operation [30] on each IMF, the low energy IMF parts (refer fig.3.1 (c) and (d), in section 3.2.3, in which blue corresponds to low energy samples and red corresponds to high energy samples as indicated in the color bar) that are lower than a threshold (which may be expected to be contributed by noise) may be eliminated.

We have used the **hard and soft thresholding** methods [30] with multiples of Donoho-Johnstone threshold known as universal threshold parameter as the cutoff in each IMF after performing EEMD. A hard and soft thresholding denosing scheme is defined as [30],

$$\tilde{c}_i(t) = \begin{cases} c_i(t), & |c_i(t)| > T_i \\ 0, & |c_i(t)| \leq T_i \end{cases} \tag{3.8}$$

for hard thresholding, and

$$\tilde{c}_i(t) = \begin{cases} sgn(c_i(t))(|c_i(t)| - T_i), & |c_i(t)| > T_i \\ 0, & |c_i(t)| \leq T_i \end{cases} \tag{3.9}$$

for soft thresholding. Where $\tilde{c}_i(t)$ represents the i^{th} thresholded IMF and T_i represents the threshold level for the i^{th} IMF.

The thresholding parameter is defined as [30],

$$T_i = C\frac{median(|c_i(t) - median(c_i(t))|)}{0.6745}\sqrt{2\ln N} \tag{3.10}$$

where C is a constant and N is length of the data. Since the noise spectra of different IMFs have different energies (refer to Hilbert spectrum shown in fig.3.1 in section 3.2.3), we have found it necessary to adopt a scale dependent threshold for each IMF instead of an identical universal threshold for all IMFs. The values of the scaling factor C were chosen to be in the range 0.6 and 1.2, with steps of 0.1 and were successively used on different IMFs until the IMF samples that are expected to contain noise (having low energy) are eliminated during the thresholding operation.

3.3.1 Interval Thresholding

We use the **interval thresholding** (IT) method [30] to alleviate the catastrophic consequences on the continuity of the reconstructed denoised signal, caused by the application of direct thresholding (see fig.3.3). In this method, the zero crossing time instances are found for each IMF, (say $Z_1^i, Z_2^i, ..., Z_{N_i}^i$ for i^{th} IMF), before (soft or hard) thresholding is applied. After the thresholding operation is performed on the IMFs, the absolute value of the extrema that fall below the threshold are considered to contain no signal, and the extrema that exceed the threshold are considered to contain the signal. In an interval between two successive zero-crossings $[Z_j^i, Z_{j+1}^i]$, even if a single extremum exceeds the threshold, the samples from the instant Z_j^i to Z_{j+1}^i of the i^{th} IMF are retained, since, at the time instance of the extrema, the signal dominance is highly likely to be extended to all the IMF samples pertaining to this specific interval. This can be represented in the following way;

$$\hat{c}_i(Z_j^i) = \begin{cases} c_i(Z_j^i), & |c_i(r_j^i)| > T_i \\ 0, & |c_i(r_j^i)| \leq T_i \end{cases} \tag{3.11}$$

where j varies from 1 to N_i, $c_i(r_j^i)$ indicates the sample at the time instance r_j^i between the two successive zero crossings at Z_j^i and Z_{j+1}^i, and $c_i(Z_j^i)$ refers to the samples from the instant Z_j^i to Z_{j+1}^i of the i^{th} IMF.

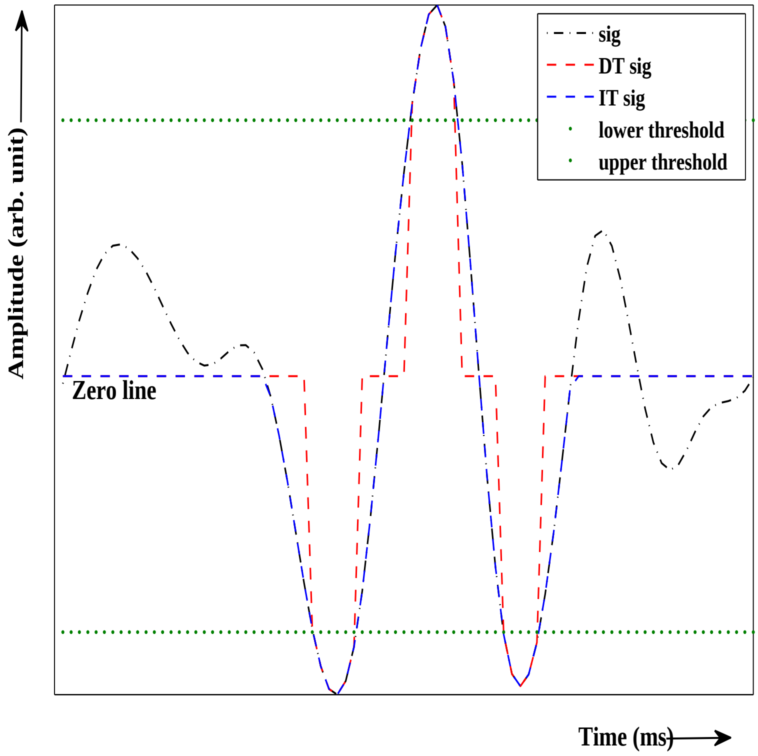

Figure 3.3: Illustration of the thresholding operation. The signal which has to be thresholded is shown with a black line. The effect of direct thresholding (DT) is shown with a red line and the effect of interval thresholding (IT) is shown with a blue line. The green dotted lines indicate the preset threshold levels. In DT, all the samples which are below the threshold level are set to zero and the samples which are above the threshold are retained. In IT, even if a single sample between two successive zero crossings exceeds the threshold level, all the samples in the interval between the two zero crossings (blue merged with black) would be retained.

3.4 EEMD denoising procedure for MCG data

The discussion so far pertained to the procedural aspects of Ensemble Empirical Mode Decomposition (EEMD) and to the recovery of the signal from without distortion in the process of decomposition into Intrinsic Mode Functions (IMFs) from all the IMFs with the view to establishing the applicability of the method. No emphasis was placed on removing the unwanted noise content, if any in the signal per say. In what follows, these considerations would be applied to denoise (suppress unwanted noise and artifacts) from the signals of interest.

Since the experimentally measured signal, and the noise contaminating it, do not always have a fixed spectral distribution (which varies spatially and temporally), it is necessary to fix the number of Intrinsic Mode Functions (IMFs) obtained from each trial of EEMD to be the same; hence, the number of IMF components which contain contributions from both signal and noise depends on the data. Given this, we apply the thresholding operation to only a few components of the low order IMFs that contain contributions from the high frequency noise contents (above 40 Hz for the present MCG data), and retain the high order IMFs that contain the low frequency contents (below 40 Hz for the present MCG data) without thresholding with a view to ensure that the low frequency content of the MCG signal does not get affected or distorted by thresholding. The choice of performing the thresholding operation only on the high order IMFs which correspond to the frequency content above 40 Hz is due to the fact that the typical ECG/MCG signal is expected to contain major frequency components below 40 Hz, and it is desirable to ensure that these signal components do not get distorted by the application of thresholding; indeed, the sole aim of performing the thresholding operation is to eliminate noise related fluctuations with amplitude lower than the prescribed threshold. The frequency limit set for thresholding can, however, be varied by the user, depending on the specific requirements of the problem.

In this way, the number of low order IMFs to be thresholded varies depending on the nature of the data since the number of IMFs is not fixed and the denoised signal is reconstructed as follows [30]:

$$\hat{x}(t) = \sum_{i=1}^{k_1} \hat{c}_i(t) + \sum_{k_1+1}^{m} c_i(t) \tag{3.12}$$

where k_1 is the highest order of IMF to be thresholded and the remaining components are unaltered, and retained without thresholding.

Having outlined the EEMD method and the steps involved in the EEMD based denoising method, we now apply it to see its efficacy for denoising as well as the elimination of baseline drift in the MCG data. The first step in the pre-processing of ECG/MCG signal involves the

elimination of baseline drift. In the as recorded MCG data, baseline drift arises either due to **slow changes** in the baseline because of breathing artifacts, electronic drifts etc. (which we term as low frequency baseline drift) or due to **discontinuous changes** in baseline because of sudden movement of the subject or sudden changes in the offset voltages during the MCG recording (which we term as high frequency baseline drift). Before any detailed analysis of the data is undertaken, it is essential to eliminate both types of baseline drifts from the as measured data. In the following sections, we describe the procedure used for the elimination of low frequency as well as high frequency baseline drifts present in the MCG data using an EEMD based method.

3.5 Elimination of low frequency baseline drift

The top panel in fig.3.1(b), in the earlier section 3.2.3 (mode mixing), is re-plotted in fig.3.4 (gray color) for illustration. It shows an experimentally measured MCG signal which is contaminated by a low frequency baseline drift. In general, the low frequency smooth variation of the baseline is expected to be contained in the residue or the highest order IMF. The smooth low frequency variation in the MCG data is generally attributed to the slow variations in the DC offset of the sensor or electronics, subject's breathing, etc.

To estimate the baseline drift present in the signal, the higher order IMFs which correspond to the very low frequency part of the spectrum [31] are considered; see bottom panels in fig.3.1(b) in the earlier section 3.2.3. If the low frequency baseline drift happens to be contained only in the highest order IMF (residue IMF), it is easy to eliminate it during the reconstruction of the baseline corrected version of the signal. However, depending on the nature of the data, it is not necessary that only the highest order or the residue IMF would correspond to the low frequency baseline drift; sometimes sum of two or three IMFs of the highest order may actually correspond to the observed low frequency baseline drift. In such a case, the residue or the sum of a few of the highest order IMFs is visually compared with the data to estimate the baseline drift. For the data presented in fig.3.4, the last four of the higher order IMFs (seen in fig.3.1(b) bottom panels in section 3.2.3) which have not undergone any thresholding treatment, have been eliminated and the remaining IMFs are then added to reconstruct the signal. The baseline drift (black) obtained by, summing the last four of the higher order IMFs (seen in fig.3.1(b) bottom panels in section 3.2.3),

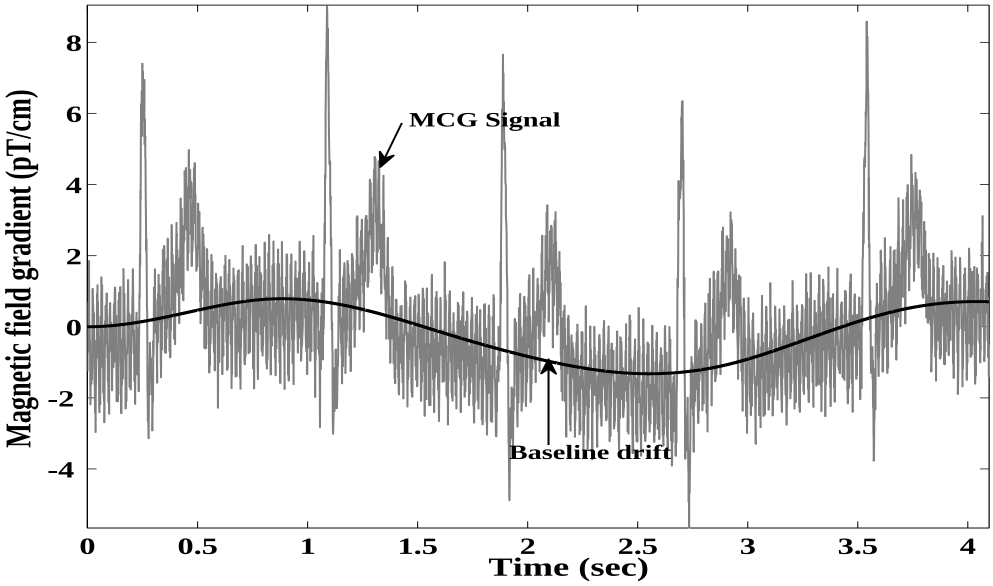

Figure 3.4: The measured MCG Signal (gray color) re-plotted from the earlier section 3.2.3 of fig.3.1(b) top panel for illustration. The MCG signal contains the low frequency baseline drift. The baseline drift extracted, by summing the last four of the higher order Intrinsic Mode Functions (IMFs) (seen in fig.3.1(b) bottom panels in the earlier section 3.2.3), from the EEMD (solid black line) method is superposed with the MCG signal. The elimination of the last four IMFs and the reconstruction of the signal from the remaining IMFs would yield the baseline drift corrected MCG data.

is superposed on the as measured MCG data in fig.3.4. The EEMD method is thus employed to extract and eliminate the low frequency baseline drift in the measured MCG data.

3.6 Elimination of high frequency baseline drift

In the context of both ECG and MCG, various methods have been reported and discussed in the literature [5, 6, 31] to eliminate the baseline drift associated with smooth low frequency variations. However, to our knowledge, no suitable method has been reported that effectively eliminates the sudden and discontinuous changes in the baseline, termed as high frequency baseline drift, such as those arising due to either a sudden movement of the subject or a sudden variation in sensor offset or drifts in the electronic modules. A sample of the experimentally measured MCG data which happened to be contaminated by sudden and discontinuous changes in the baseline is shown in fig.3.5(a). In this context, we propose a **novel method based on the use of EEMD** for the elimination of the high frequency baseline drift (seen in fig.3.5(a)) and the procedure proposed is described below.

- The first IMF (containing the high frequency content of the signal), obtained from EEMD is hard thresholded (with appropriately scaled universal threshold parameter as the threshold level (defined in Eq.3.10)) and subsequently the interval thresholding method is applied to this.
- The interval thresholded first IMF acts as the window of a band-pass filter (the values will be non-zero within the window and zero outside the window), which allows the other unthresholded IMFs (from the second IMF to the residual IMF) to pass through this window while the values outside the window are cutoff (set to zero).
- All the IMFs, after passing through this band-pass window, are summed up.
- The data which falls outside the band-pass window, after summing up, is replaced by the mean of the (raw) data between the two successive windows.
- The above procedure yields the high frequency baseline drift and the subtraction of this drift from the raw data yields the high frequency baseline drift corrected data.
- The band-pass window data after baseline correction is interpolated with the cubic spline fitted data from the neighboring data points.

In practice, the last step is required only when there is a large low frequency baseline variation contained in the original data.

We know that the wavelet acts as a dyadic filter and that the detailed and approximation coefficients contain the signal components of fine and coarse scales respectively; hence, the wavelet may be used to form a low, high or band pass filter depending on the wavelet coefficients retained during the reconstruction of the signal. The high frequency baseline drift, and the drift corrected data obtained by the wavelet based high pass and band pass filter settings are represented in the fig.3.5(b)-3.5(d) respectively. It may be noted from figures 3.5(c) and 3.5(d) that, the removal of either the low frequency components or a combination of both low and high frequency components does not completely eliminate the high frequency baseline drift present in the measured signal and,

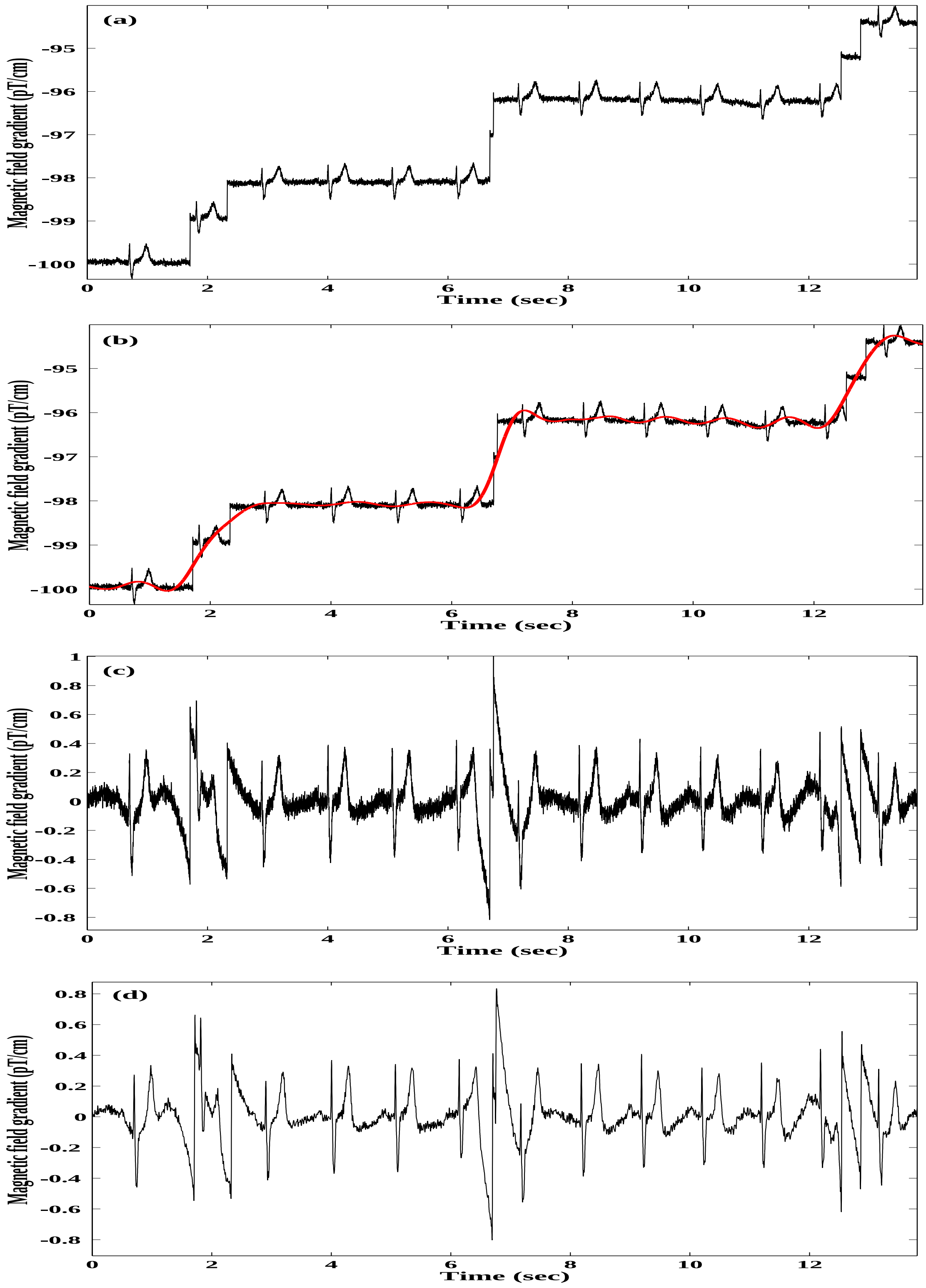

Figure 3.5: (a) A sample of a particular MCG signal showing sudden discontinuities in the baseline. (b) The baseline drift (red solid line) obtained by high pass filter is superposed with the measured signal (black solid line). The baseline drift corrected signals by (c) high pass filter and (d) band pass filter are shown. The selective signal reconstruction, from the wavelet coefficients that form high and band pass filters, fail to eliminate the effect of high frequency drift completely. This can be clearly seen from the distortion of the signals that appears in the baseline drift corrected signals in the panels (c) and (d).

indeed, the wavelet based procedure produces significant distortions in the drift corrected data. Our investigations showed that the conventional wavelet based techniques were unable to suppress such high frequency baseline drifts.

In order to eliminate such a high frequency baseline drift, we adopted the procedure described in the above section. The data, shown in fig.3.5(a), was subjected to signal decomposition by the EEMD method and the results are shown in fig.3.6. The IMFs obtained from the EEMD are used for estimating the high frequency baseline drift in the MCG signal. We have illustrated the sequence of steps used for eliminating the high frequency baseline drift in fig.3.7. The interval threshold of the first IMF is used as a band pass, as shown in fig.3.7(a) and represents the pass-band through which all other IMFs are allowed to pass (fig.3.7(b)). The subsequent steps follow as described in the earlier paragraph describing the procedure and are schematically represented in fig.3.7(c)-

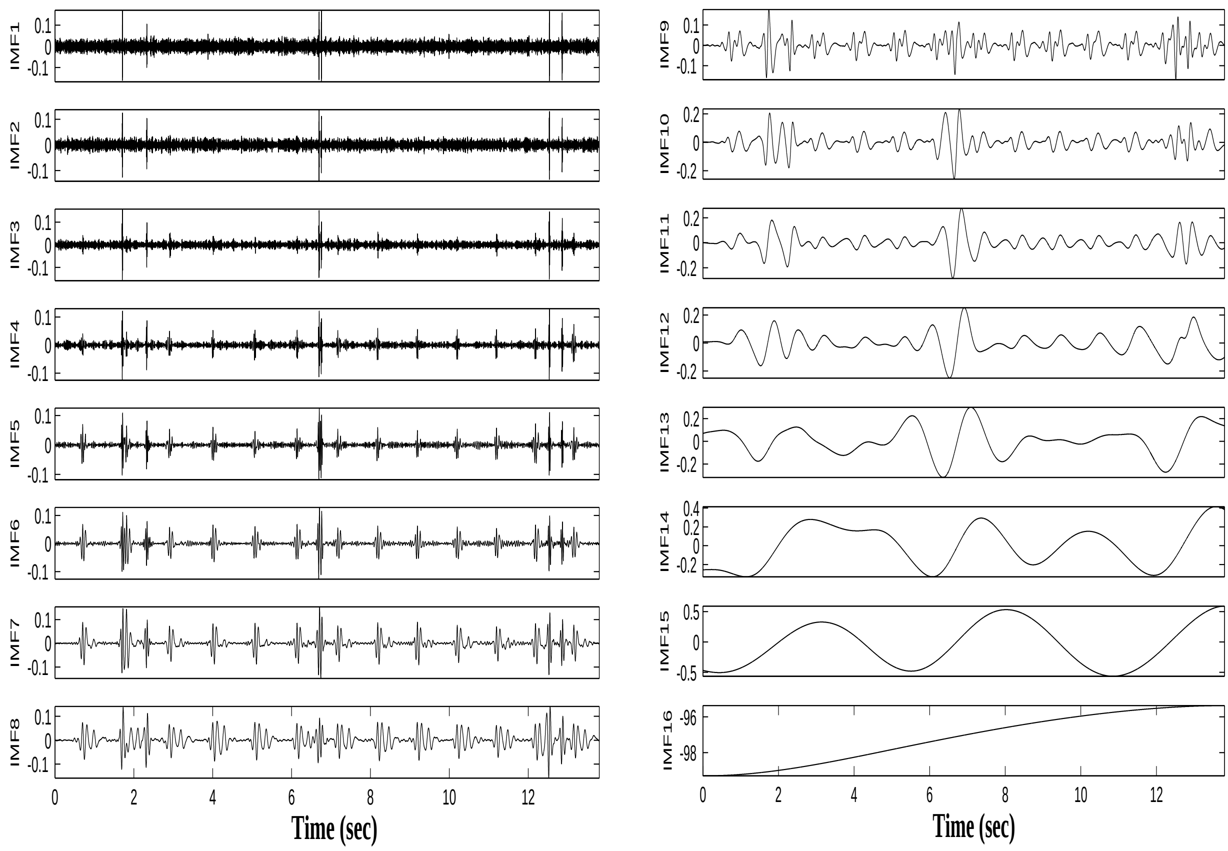

Figure 3.6: The sixteen IMFs obtained from the EEMD of the signal shown in fig.3.5(a) are stacked in two columns. The ordinate is magnetic field gradient (pT/cm). The IMFs obtained from the EEMD are used for selective signal reconstruction to eliminate the baseline drift.

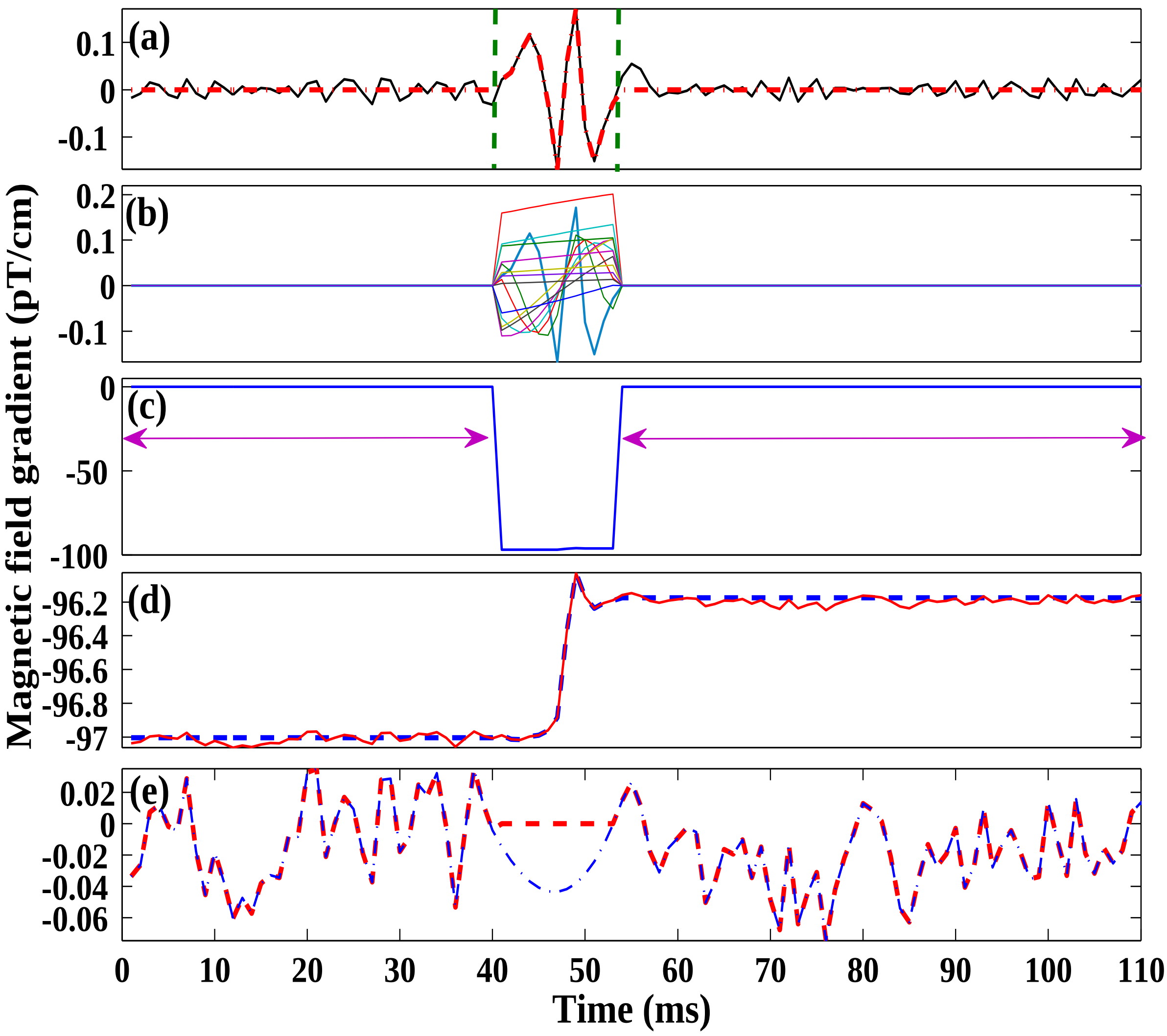

Figure 3.7: Various steps involved in the elimination of the high frequency baseline drift. (a) The interval thresholding (red) of the first IMF (black) and the time window (green) are marked. (b) All the IMFs as passed through the time window in (a) are shown (for clarity, the residual IMF is not shown because of its large amplitude). (c) Sum of the IMFs, including the residual IMF, is taken after passing them through this window (blue); the zero line outside the window on either side is indicated by arrows. (d) The zero line in (c) is replaced with the mean of the data (blue); the raw data (red) is also shown. (e) Baseline drift corrected data without spline interpolation (red merged with blue) and with spline interpolation (blue) at the time window are shown.

3.7(e). This procedure was used to obtain a credible estimate of the high frequency baseline drift and was compared with the baseline drift estimated from the wavelet based decomposition. For the wavelet based estimation of baseline drift, Daubechies wavelet *db10* with a user selectable level of decomposition was used and the last detailed coefficients were interval thresholded and windowed, since the detailed coefficients are expected to contain the high frequency components. The baseline drifts estimated from the wavelet and the EEMD based technique are shown in fig.3.8(a) along with the raw data and the differences in the drift estimated by the EEMD and the wavelet methods are shown in the insets on an expanded scale. It may be noted from the left-top inset of fig.3.8(a) that the wavelet based method does not eliminate the baseline drift completely, whereas, the EEMD

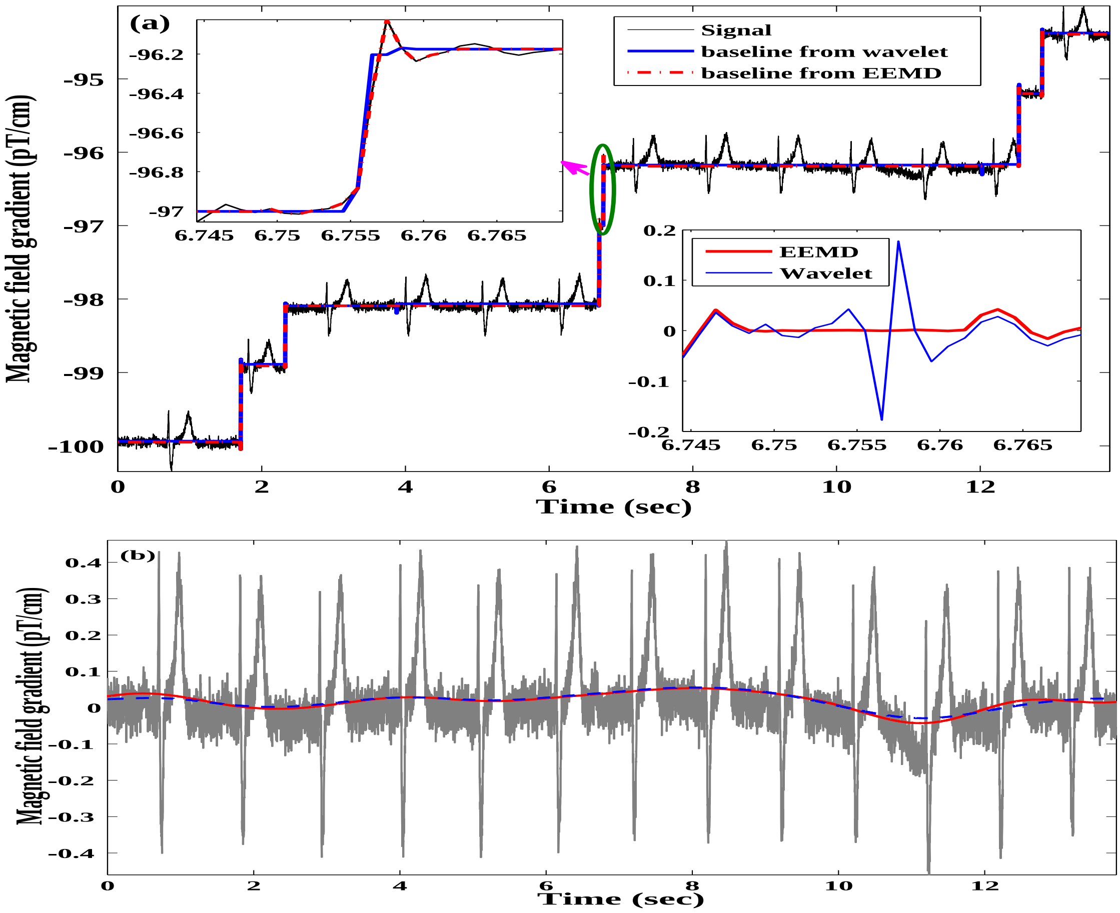

Figure 3.8: The top panel (a) shows the signal (black solid line) along with the baseline drifts obtained from the EEMD (red dashed line) and the wavelet (blue solid line) based method. The left-top inset shows the part of the trace within the green oval on an expanded scale and the right-bottom inset shows the baseline drift corrected data (red - EEMD and blue - wavelet based method) at this expanded section. The wavelet method produces a slight distortion in the baseline corrected data, as seen in the difference plot, whereas the **EEMD method performs better** in the baseline correction. (b) The high frequency drift corrected signal (gray) along with the low frequency baseline obtained from wavelet (blue dashed line) and the EEMD (red solid line). It may also be noted that there is no distortion in the high frequency drift corrected data by EEMD based method when compared with that obtained by conventional high pass and band pass filtering methods shown in fig.3.5(c) and 3.5(d) respectively.

based method proposed by us does. The wavelet based method also produces somewhat greater distortion in the baseline corrected data as compared to the EEMD based method as seen clearly in the right-bottom inset of fig.3.8(a).

Although the proposed method was successful in eliminating the sudden and discontinuous changes in the baseline, the low frequency baseline drift still persisted. The low frequency baseline drift obtained by the EEMD method, as described in section 3.5, is shown in fig.3.8(b)(red color) superposed along with the high frequency drift corrected data. The low frequency baseline drift corrected data using the wavelet based method is obtained by eliminating the approximation coefficients which contain the low frequency part of the signal. We used Daubechies wavelet of kind *db10* with a user selectable level of decomposition in such a way that the baseline drift was contained in the appropriate approximation coefficients. The low frequency baseline drift obtained by the wavelet based method is also shown in fig.3.8(b)(blue color). It may be noted that the elimination of low and high frequency baseline drifts are two independent procedures, and the sequence or order of elimination of high and low frequency baseline drifts can be decided based on the spectral power of the frequency content of the observed baseline drift. If the spectral power of the high frequency baseline drift happens to be larger than that of low frequency baseline drift, it could be eliminated first followed by the elimination of the low frequency baseline drift and vice versa.

Having seen the application of EEMD to the baseline drift elimination, we now apply the EEMD thresholding based method to the simulated and experimental MCG data in order to reconstruct the denoised version of the signal.

3.7 Denoising by EEMD: Application to simulated data

In the present study, three different types of noise have been deliberately added to the experimentally measured MCG signal with a high signal-to-noise ratio to produce a simulated noisy signal and the **effectiveness of the EEMD** technique in processing this simulated noisy signal and reconstructing the denoised version was investigated. The types of noise added include a low frequency (0.3 Hz) sinusoidal signal for simulating the baseline drift, 50 Hz sinusoidal signal for simulating the interference at power line frequency, and a high frequency random noise. Thus, the added noise was a combination of three different sources of noise given below [31].

$$n_1(t) = (1/8) * B_{pp} * randn \tag{3.13}$$

$$n_2(t) = (1/4) * B_{pp} * \sin(2 * \pi * 50 * t) \tag{3.14}$$

$$n_3(t) = (1/5) * B_{pp} * \sin(2 * \pi * 0.3 * t) \tag{3.15}$$

$$n(t) = 0.8 * [n_1(t) + n_2(t)] + n_3(t) \tag{3.16}$$

where, B_{pp} is the absolute maximum of the peak-to-peak value of the original signal. The noise $n(t)$ is multiplied with various scaling factors (between 0 and 1) to yield different signal-to-noise ratios (SNR), defined as

$$SNR = 10 * \log \left(\frac{\sum_{i=1}^{N} s^2(t_i)}{\sum_{i=1}^{N} (s(t_i) - \hat{s}(t_i))^2} \right) \tag{3.17}$$

where, $s(t_i)$ is the original signal at the time instant t_i and $\hat{s}(t_i)$ is the denoised signal (or signal with noise, $s(t_i) + n(t_i)$) at the time instant t_i.

Fig.3.9(a) shows the simulated MCG signal, viz, with the addition of noise as in Eq. 3.16, so as to give a signal to noise ratio of -4dB. Fig.3.9(b) shows the denoised (and baseline drift corrected) signal obtained by the EEMD method with hard-direct thresholding (blue) while that obtained by hard-interval thresholding (red) is superposed along with the original signal (black) before the addition of noise. In the hard-direct thresholding method, the IMF was hard thresholded, i.e., the IMF samples having values lower than the preset threshold value were set to zero and the samples having values higher than the preset threshold value were retained as such. If we add such hard thresholded IMFs, this would result in the appearance of discontinuities in the reconstructed signal. In view of this, we apply interval thresholding subsequently to the hard thresholded IMFs in the hard-interval thresholding method. The interval thresholding retains all the IMF samples (which exist before the application of hard thresholding), even if a single value between the two successive zero crossing points exceeds the preset threshold value. The discontinuity in the signal caused by the application of direct thresholding (DT) is shown in the inset of fig.3.9 which represents the expanded section of the rectangular box (in the duration of 0.15 to 0.4 sec) shown in fig.3.9. It is clearly seen that the interval thresholding reduces the discontinuities in the denoised signal.

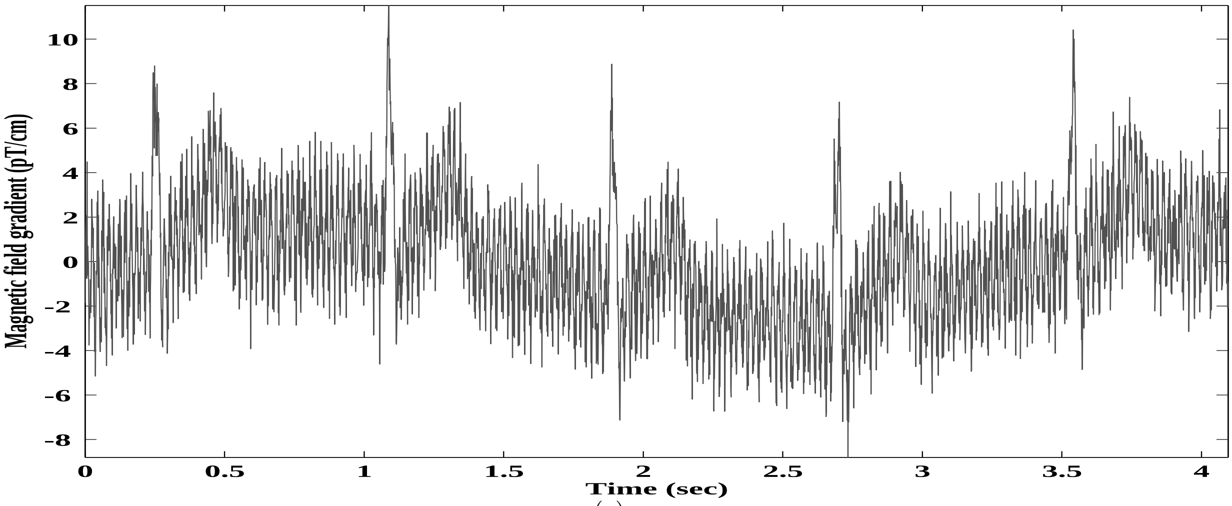

(a)

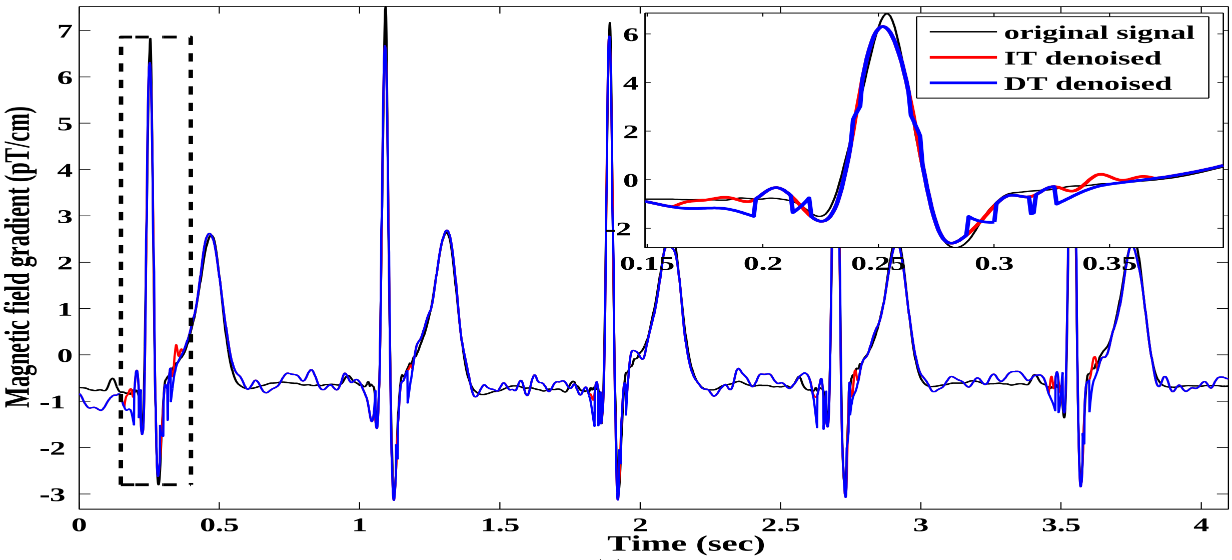

(b)

Figure 3.9: (a) The simulated MCG signal, viz, with the addition of noise as in Eq.3.16, resulting in a signal to noise of -4dB and (b) The denoised signals by EEMD-interval thresholding (red) and EEMD-direct thresholding (blue) methods superposed with the original signal before the addition of noise (black). The inset represents the expanded section of the rectangular box in the duration of 0.15 to 0.4 sec to indicate the discontinuity in the signal (blue) caused by the effect of direct thresholding (DT). The MCG signal quality is significantly improved by EEMD based denoising method. Further, the interval thresholding method effectively reduces the discontinuity in the signal caused by the direct thresholding method.

In fig.3.10, we compare the performance of the wavelet and the EEMD based denoising methods using hard and soft thresholding (defined in Eq.3.8 and 3.9 respectively) in both cases. The wavelet based denoising was performed with a Daubechies wavelet of 'db10' with user selectable level of decomposition with a view to remove the low frequency baseline drift for all the cases. The reduction in the SNR for the soft thresholding method is due to the reduction in the signal content (refer Eq.3.9) of the lower order IMFs. It is seen from fig.3.10 that the EEMD method is capable of achieving better SNR when compared to wavelet based denoising. It may also be noted that, SNRs

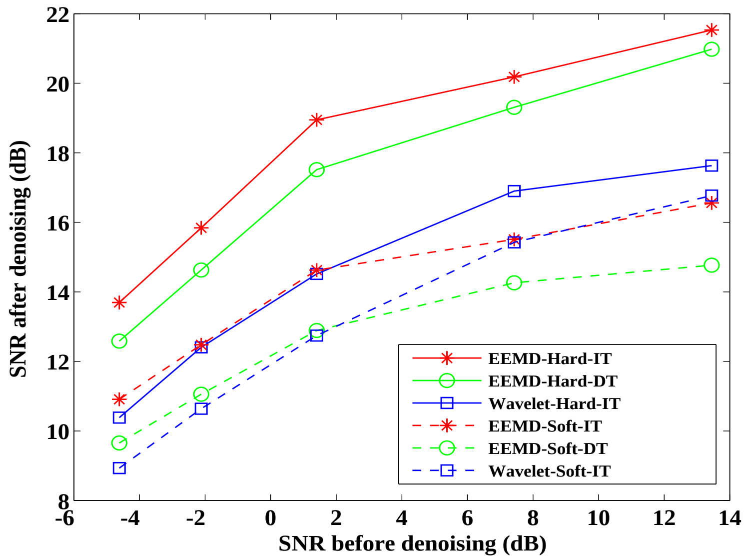

Figure 3.10: The variation of the signal-to-noise ratio (SNR) after denoising by wavelet and EEMD techniques with soft (dashed lines) and hard (solid lines) thresholding for both Direct Thresholding (DT) and Interval Thresholding (IT) schemes. The EEMD method outperforms the wavelet based denoising method, while the use of Interval Thresholding (IT) improves the SNR when compared to the Direct Thresholding (DT).

are much better for the interval thresholding (IT) method compared to the direct thresholding (DT). In view of this, henceforth in this chapter, hard-IT (hard thresholding followed by interval thresholding) is adopted as the preferred procedure for both the EEMD and the wavelet based denoising of the experimental data.

3.8 Denoising by EEMD: Application to experimental data

In the following, we illustrate the application of the EEMD method to the experimentally measured MCG data. MCG was recorded on a human subject in the supine position inside a magnetically shielded room (MSR) using a 37 channel MCG system [33] at a sampling rate of 1 kHz and with low pass filter setting of 300 Hz. The details of the measurement are given in chapter 2. Among the 37 channels, the data in a few channels were found to be quite noisy, i.e., having poor SNR, and it was essential to denoise such data by EEMD based method. For the purposes of illustration, we have selected here the noisy MCG signals measured in two channels, which were found to be particularly noisy: the first one was contaminated with the power line interference (50 Hz) as well as baseline drift (fig.3.11(a)) and the second one was contaminated by high frequency noise (fig.3.11(c)). It may be noted that although, for the purposes of illustration, we have shown the experimental data sets corresponding to these two channels only, the method has been applied to all the measurement channels. The denoised MCG signals, as obtained using the hard-IT by the EEMD and the wavelet based methods are shown in fig.3.11(b) and fig.3.11(d) respectively. The value of parameter C in Eq.3.10 (between 0.6 and 1.2) used for thresholding and

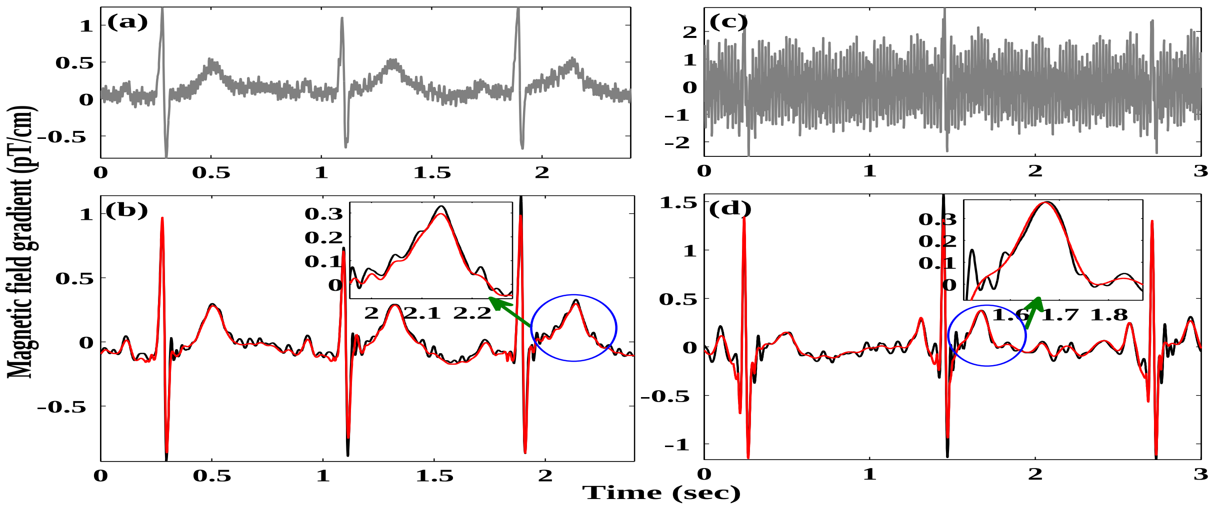

Figure 3.11: The top panels (a) and (c) represent the measured MCG signals (gray color) in two different channels. The first one (a) is corrupted by 50 Hz power line interference and the second one (c) is corrupted by high frequency noise. The bottom panels (b) and (d) represent the denoised signals obtained by EEMD-IT (red) and wavelet-IT (black) methods. For clarity, only a few cardiac cycles are shown in each case. The insets in the panels (b) and (d) show the expanded section of the data within the blue oval as indicated by arrows. The MCG signal features (P,QRS and T wave) which are buried in the noise in the panel (c) are successfully extracted. The quality of the denoised experimental data is better for the EEMD method, as can be clearly seen from the inset of figures where the noise oscillation is reduced at the location of the T-wave, when the EEMD method is used as compared to the wavelet method.

the detailed procedure used (given in section 3.4) for processing of experimental data was identical to that used for the synthetic or simulated data. It is seen that the MCG signal features (P, QRS and T wave), which are buried in the noise in the as recorded data, are successfully extracted and the quality of the denoised experimental data is better for the EEMD method as compared to the wavelet method. This can be further clearly seen from the inset of figures 3.11(b) and 3.11(d) where the noise oscillations are reduced, especially at the location of the T-wave, when the EEMD based method is used as compared to the wavelet based method. Also, the experimental MCG data presented in fig.3.8 (in section 3.6) denoised by the EEMD based hard-IT method is shown in fig.3.12. It may be noted that the denoised signal reveals cardiac features which were buried in the noise originally and, further, the procedure does not cause any distortion in the denoised signal.

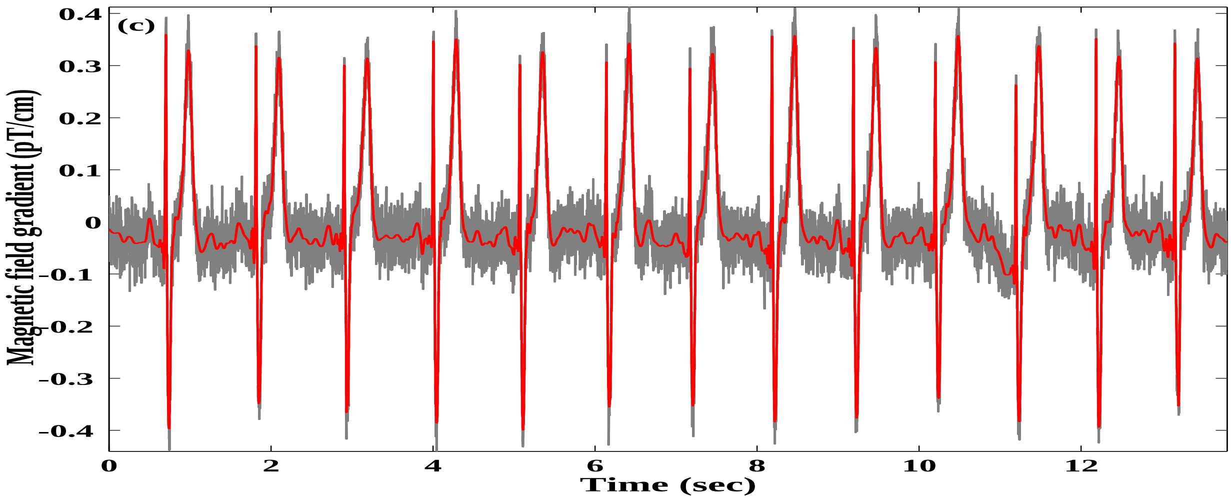

Figure 3.12: The MCG data presented in fig.3.8(a) after the removal of high frequency and low frequency drifts by the EEMD method shows no distortion (gray color). Also, the baseline drift corrected signal, when further denoised by the EEMD method (red color), reveals the cardiac features which were otherwise buried in the noise.

3.9 Comparison of EEMD and ICA based denoising

The performance of the EEMD based denoising method was also compared with that achieved using Independent Component Analysis (ICA) [2, 32], which is another technique used conventionally for denoising the measured data. The latter is closely related to the Blind Source Separation (BSS) technique [34], that extracts the statistically independent components (IC), by de-mixing the observed signals, from the simultaneously measured multichannel spatio-temporal data representing an admixture of Independent Components (ICs) with an unknown mixing matrix. The ICA relies on the assumption that the observed signals are spatial mixtures of temporally independent sources, which are non-Gaussian. ICA has been widely used in the signal processing for removing the artifacts from noisy as recorded signals. The denoised signal is reconstructed by setting to zero, the ICs corresponding to artifacts.

Fig.3.13 shows the application of ICA to the 37 channel MCG data to reconstruct the denoised signal, although, for clarity, the results corresponding to only five channels have been shown. For

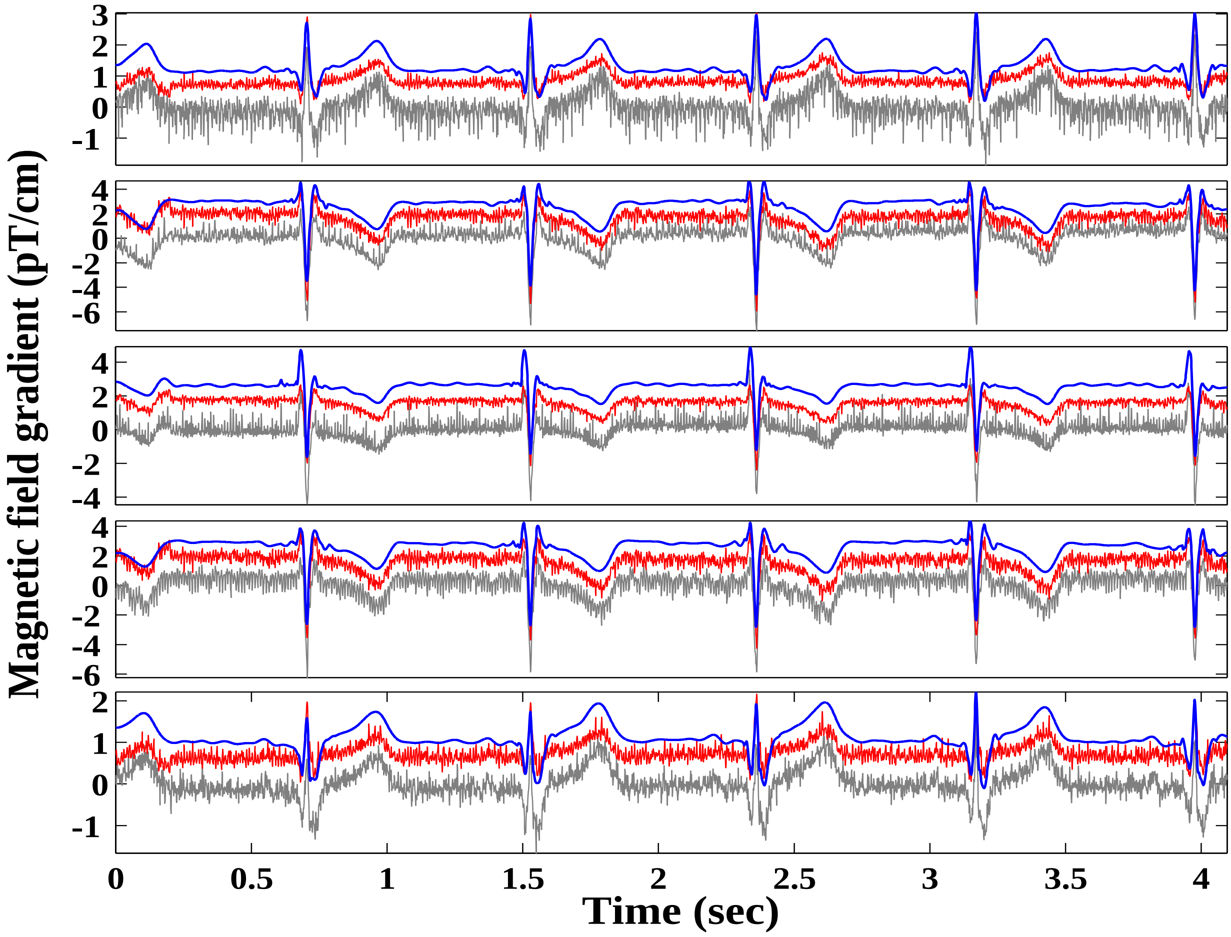

Figure 3.13: A few representative channels, from 37 channel experimental MCG data, denoised using ICA (red) and EEMD (blue) based methods, along with the measured (gray) MCG data, for a comparison of performance of the two methods. For clarity, the traces are vertically shifted along the y-axis. The EEMD based denoising method reveals well resolved cardiac features and achieves a considerably higher noise suppression when compared to the ICA based denoising method.

the present data set, nine independent components (limited by principal component analysis (PCA) based energy-eigen value spectrum) were found and four were identified as corresponding to artifacts and the signal was reconstructed using the remaining five non-artifact ICs. For the same MCG data set, EEMD based hard-IT method was applied independently to each channel and the results (indicated in blue line) have been shown as superposed with the respective ICA based denoised data for a comparison of the performance of the two methods. The parameter C used for thresholding of the IMFs had the same value as before (between 0.6 and 1.2). It is evident from fig.3.13 that EEMD achieves a considerably higher suppression of noise compared to ICA in this case resulting in superior quality for the denoised MCG signals with well resolved cardiac features.

3.10 Application of EEMD for His bundle detection

Detection of the His-bundle activity is extremely important in the management of arrhythmia and in clinical decisions related to implantation of a pacemaker based on the duration of the observed AH interval (Atrial contraction to His-Bundle, typically 60-140 ms) and HV interval (His-bundle to Ventricular contraction, typically 35-55 ms); in the current clinical practice, this requires an ICU based electrophysiological study (EP) involving an invasive insertion of catheter based electrodes right in the vicinity of the His-bundle, especially since this structure is located amidst electrically insulating tissues. One of the important clinical applications of MCG involves the possibility of the non-invasive detection of the rather weak His-bundle activity (magnetic field strength of ~200 fT) [8]. Since the His-bundle activity is extremely weak, it is usually masked by noise in a typical cardiac cycle and it is necessary to employ signal averaging techniques (averaging a large number of cardiac cycles by aligning them with respect to a fiducial reference point) to suppress uncorrelated random noise in order to discern the characteristic features associated with the His-bundle activity. The choice of fiducial point for signal averaging in case of His-bundle detection is crucial as the inevitable variation in the heart rate [35, 36] results in variations in the durations of different segments of the cardiac cycle such as the PR interval and the QRS. When the R-peak is chosen as the fiducial point for averaging (as has been done in most of the studies hitherto), the beat-to-beat fluctuation in the QRS duration potentially smears out the relatively weak His-bundle feature. In view of this, Sengottuvel et al [35] have proposed the use of **QRS onset as the fiducial point** for averaging the cardiac cycles, since the HV interval is known to remain relatively constant from beat-to-beat; indeed, the use of QRS onset as a fiducial point for averaging of cardiac cycles has made it possible to non-invasively detect a robust feature associated with the His-bundle, compared to many of the earlier studies, which used the R-peak as the fiducial point.

Although the QRS onset (or ventricular onset) works well as the fiducial point for His-bundle detection, the number of cardiac cycles (beats) that needs to be averaged is very large, depending on the amplitude of noise present in the measurement. Use of EEMD for denoising the measured MCG signal, therefore, has the potential to substantially lower the noise level present in the denoised data, and, consequently, to unravel the His-bundle activity by averaging only a considerably lower number of cardiac cycles. We illustrate this approach by the application of EEMD for preprocessing the signal to reduce the overall noise level, and eliminate the baseline drift, breathing artifact (typically 15 cycles/min), power line interference etc. before signal averaging is performed. Fig.3.14(a) and (b) show the extraction of His-bundle activity using the measured data on four channels after signal averaging was performed with QRS onset as the fiducial reference point. It may be noted that in the absence of EEMD based preprocessing, it was necessary to average about 200 cardiac cycles to reveal the His-bundle activity with some clarity (fig.3.14(a)), while averaging over just 8 cardiac cycles was sufficient when EEMD based preprocessing was used to denoise the signal (fig.3.14(b)). The effectiveness of the conventional wavelet based denoising technique has also been investigated in the context of noninvasive detection of His-bundle activity. For the wavelet based pre-processing,

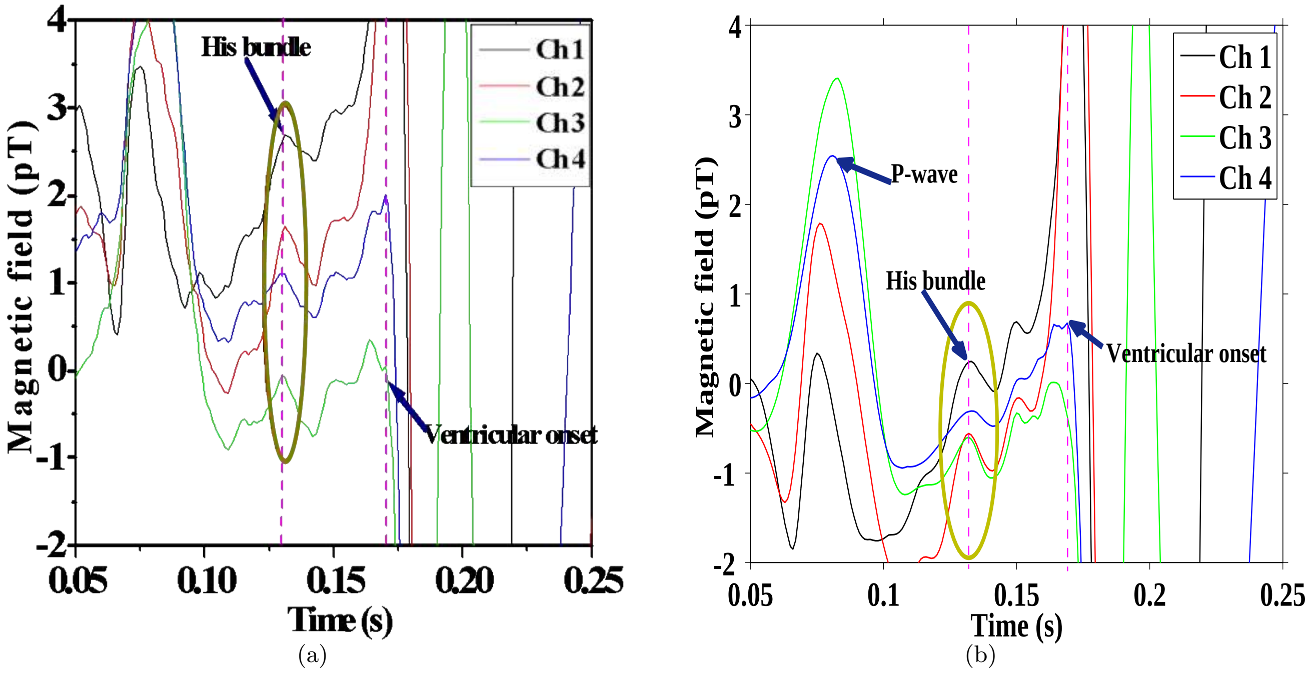

Figure 3.14: Detection of His bundle activity using the signal averaged MCG (SAMCG), with QRS onset (or ventricular onset) as a fiducial point, by averaging more than 200 cardiac cycles (after wavelet pre-processing) in (a) and only 8 cardiac cycles (after EEMD pre-processing) in (b) is shown. It may be noted that for the signal pre-processed with EEMD before signal averaging is performed, the weak His bundle activity is seen conspicuously with considerably lower number of averages.

Daubechies wavelet *db10* was used and the data was subjected to a level of decomposition such that low frequency approximation coefficients contain the low frequency fluctuations such as baseline drift, subject's breathing and movement artifact; the undesired components of the measured signal represented by such wavelet coefficients are suppressed during the reconstruction of the denoised version of the signal. It is evident from fig.3.14(b) that it is possible to extract the His-bundle activity from the Signal Averaged MCG (SAMCG) with considerably **lower number of averages when EEMD based pre-processing is used**, whereas a much larger number of cardiac cycles had to be averaged to reveal the His-bundle activity when wavelet based preprocessing is used (fig.3.14(a)). This was found to be due to the fact that the identification of QRS onset as the fiducial point in the EEMD based denoised data is clearer and more pronounced and also the elimination of artifacts is more efficient in EEMD based denoised data as compared to that denoised by wavelet or other techniques. Any ambiguity or variability in the identification of QRS onset due to residual noise fluctuations (owing to the very short duration of His-bundle activity) would result in smearing out of the feature, thus necessitating the averaging of a larger number of cardiac cycles to adequately suppress the uncorrelated noise and reveal the very weak signal associated with the His-bundle activity.

3.11 On the application of combined EEMD and ICA for denoising the multichannel data

Although the EEMD method was shown to be superior in denoising the MCG data compared to the other conventional denoising techniques such as wavelet and ICA based methods, the computational burden associated with the use of EEMD (as it involves the computation of data driven basis functions by an iterative procedure as described in section 3.2.1 and the computation of ensemble averages over a large number of trials as described in section 3.2.2) is significantly higher even for handling single channel data; this computational burden increases further when the number of channels to be denoised increases. Thus, a direct application of EEMD to multichannel MCG data with a large number of channels involves a significantly high computational burden, and, hence, there is a need to find an alternative strategy aimed at reducing this computational burden in using EEMD for preprocessing. It may be noted in this context that Independent Component Analysis (ICA) [2, 34, 37] is a widely used technique for the elimination of artifacts in the case of multichannel MCG data with a large number of channels [17], although in practice our investigations have shown that ICA, by itself, is not adequate to suppress the artifacts completely (as can be seen in fig.3.13 in the section 3.9). In view of this, use of a combination of wavelet and ICA (wICA) [38] and also EMD and ICA (EMD-ICA) [39] have been proposed, to enhance the quality of the reconstructed denoised signal. In the context of Electroencephalography (EEG), the artifact removal using wICA has been reported [38, 40, 41, 42] for the multichannel EEG data.

It has been pointed out earlier that a limitation of the wavelet based method is that it is based on a set of predefined basis functions to decompose the signal and a limitation of the EMD based method is that the Intrinsic Mode Functions (IMFs) suffer from mode mixing. To overcome these limitations, we have carried out a combination of EEMD and ICA for denoising the multichannel MCG data with a large number of channels. The **combination of EEMD and ICA involves much reduced computational burden** compared to the use of EEMD alone in the context of multichannel MCG data with a large number of channels, since, in this case, the number of independent components is likely to be substantially lower compared to the total number of channels as discussed in the following section and EEMD needs to be applied only to each ICA component rather than to each measurement channel.

3.11.1 ICA based denoising methods

Before, we apply the combination of EEMD and ICA to the multichannel MCG data, we discuss the basic features of the three methods based on ICA for the elimination of artifacts:

- The conventional ICA artifact suppression [17] involves the estimation of unknown mixing matrix ($\mathbf{A}$) and the extraction of independent sources ($\mathbf{s(t)}$) from the measured spatio-temporal data ($\mathbf{x(t)} = \mathbf{As(t)}$), followed by the reconstruction of the artifact free signal by setting to zero all the visually identifiable independent sources which can be attributed to artifacts. Then, the back projection of the perceived non-artifact sources with the mixing (or weighting) matrix provides the artifact suppressed signals.

- In the wavelet enhanced ICA (wICA) method [40], the multichannel MCG data is subjected to ICA to obtain the Independent Components (ICs) and then the wavelet based denoising is used as an intermediate step to eliminate the signals of interest, such as the cardiac source whose components may have leaked into the ICs representing artifacts and retain only the artifact components which are then projected back to obtain the artifact signals contained in the MCG data. These artifact signals are then subtracted from the raw MCG signals to estimate the artifact free MCG signals.

- In the EEMD-ICA method, described in the present work, we adopt the ICA method to decompose the multichannel MCG data into statistically independent sources and then apply the EEMD method to the independent sources that are visually identified as non-artifact sources. Here, the non-artifact ICs or sources referred to are the cardiac source components contained in the ICs. Each such identified non-artifact independent source is subjected to the decomposition by the EEMD method into IMFs and the threshold based EEMD denoising method (see section 3.3) is applied to these IMFs. The IMFs corresponding to the baseline drift and breathing artifact, which lie in the low frequency part of the spectrum, are also eliminated before the reconstruction of the denoised signal. The identified artifact components are set to zero and the non-artifact components denoised by the EEMD method are projected back with the mixing matrix to reconstruct the signals.

Application of EEMD to each channel of a multichannel MCG system may be computationally very intensive when the number of channels is large (say ~ 100) because the application of EEMD involves ensemble averaging over a large number of trials. When a combination of ICA and EEMD is used, however, ICA decomposes the measured signals into a much smaller number of statistically independent components (say ~ 20) and EEMD has to be applied only to each IC rather than to each channel, resulting in a significant reduction of computational burden.

We now illustrate the suppression of artifacts in the multichannel MCG data, recorded in our laboratory, by using the EEMD-ICA method and compare the results with those obtained by other established methods such as Independent Component Analysis (ICA) and the wavelet-ICA (wICA).

The MCG data was recorded simultaneously at 37 spatial locations on a human subject using a 37 channel SQUID based system, inside a Magnetically Shielded Room (MSR). The as recorded data in different channels was contaminated by several sources of noise and artifacts such as baseline drift, breathing artifact, 50 Hz power line interference, high frequency random noise, etc., as shown in fig.3.15. The level and type of noise and its variation across the different channels are attributed to the differences related to sensor noise, closeness of the noise source (say breathing, movement of the subject) to the sensors, spatial variation of the noise components, noise contributed by processing electronics, etc.

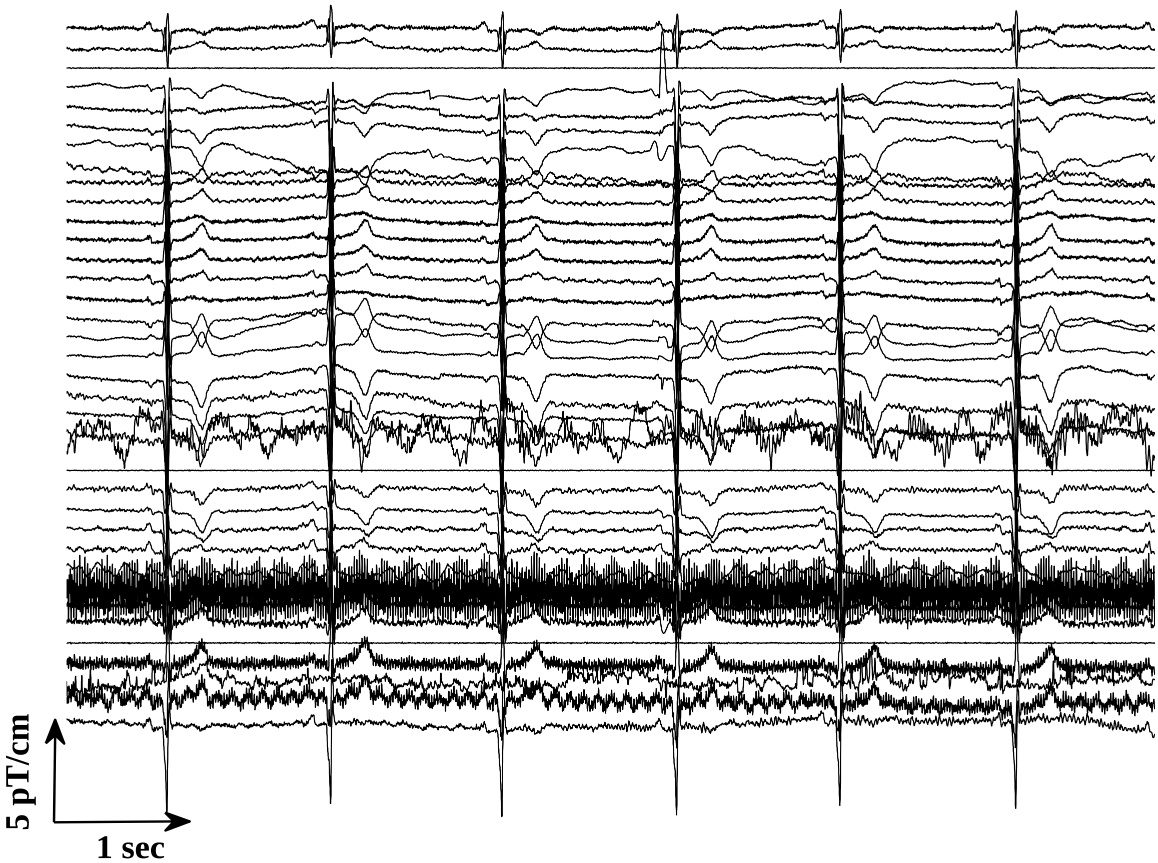

Figure 3.15: An experimentally measured MCG data on a human subject, contaminated by various types of noise such as low frequency baseline drift, breathing artifact, 50 Hz and harmonics, high frequency random noise, etc., at 37 spatial locations (for clarity, each channel is shifted vertically).

The multichannel spatio-temporal MCG data, shown in fig.3.15, was first subjected to the ICA and fifteen ICs were estimated as shown in fig.3.16. The top inset of fig.3.16 shows the eigenvalue spectrum, obtained from the Principal Component Analysis (PCA), which is used for limiting the

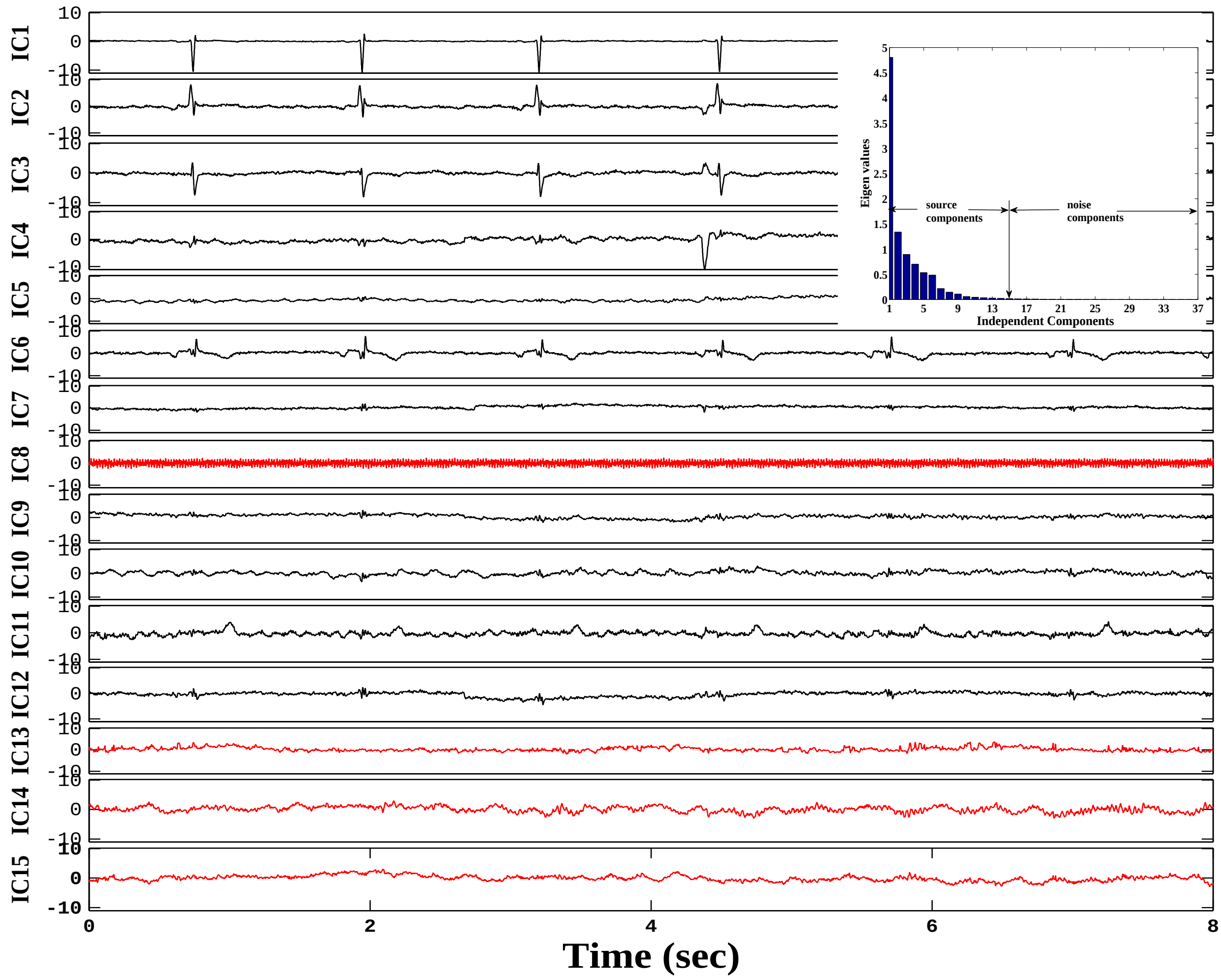

Figure 3.16: The independent components (ICs) obtained from the Independent Component Analysis (ICA) for the MCG data presented in fig.3.15. The ordinate indicates the magnetic field gradient (pT/cm). The visually identified artifact components (50 Hz and harmonics) are indicated by red and the non artifact components (guided by periodic nature of cardiac features such as QRS complex and T-wave) are indicated by black. The top inset shows the eigenvalue spectrum, obtained from Principal Component Analysis (PCA), from which the number of ICs is limited in such a way that the components covering 99% of the signal power are assumed to belong to the signal subspace while the components covering the remaining 1% of the signal power are assumed to belong to the noise subspace. For the data presented in fig.3.15, fifteen ICs cover 99% of the signal power.

number of ICs to represent the data. The components that cover 99% of the signal power (from left to right in the inset of fig.3.16) are assumed to belong to the signal subspace, while the components which contain the remaining 1% of the signal power are assumed to belong to the noise subspace, and are consequently ignored. By visual inspection, eleven of these were designated as non-artifact ICs (shown in black in fig.3.16, guided by the periodic nature of the cardiac features such as QRS complex and T-wave) while the other four were identified as artifact ICs (shown in red in fig.3.16).

In the conventional ICA based artifact suppression method, the identified four artifact ICs are set to zero and the eleven non-artifact ICs, as such, are projected back to obtain the artifact suppressed signals. In the wICA method [40], the eleven non-artifact ICs are denoised by the wavelet based interval threshold denoising method and these denoised ICs are then subtracted from the corresponding non-artifact ICs to obtain the artifacts. The artifact-only ICs are then back projected with the mixing matrix to estimate the artifact signals which are eventually subtracted from the raw MCG data to obtain the artifact suppressed signals. For the wavelet based denoising, we have used Daubechies wavelet of kind $db10$ with a level of decomposition in such a way as to ensure that the low frequency baseline drift is contained in the appropriate approximation coefficients. We have also used the interval thresholding (IT) [30], which has not been used by others earlier in using the wICA method [40], with a view to reducing the discontinuities in the reconstructed denoised signal that are caused by the application of direct thresholding (DT) as discussed in the section 3.3.1. The universal threshold parameter [30] (see Eq.3.10) was used for thresholding the wavelet detail coefficients that contain high frequency components.

The EEMD-ICA combination method employed in the present work uses EEMD interval threshold method as an intermediate step to denoise the eleven non-artifact ICs and the denoised ICs are projected back with the mixing matrix, by setting the other four artifact ICs to zero, in order to obtain the artifact free signals. As an illustration, the top panel of fig.3.17 shows the sixth non-artifact independent component obtained from ICA and the middle panel shows the denoised version of that component obtained by the EEMD interval threshold based method. The detailed procedure for the EEMD interval threshold based method is described in section 3.4. The universal threshold parameter was used for thresholding the IMFs which was identical to that used in the wavelet based method. The bottom panel of fig.3.17 represents the residue, which is the difference between the sixth independent component and its denoised version, and is indicative of the amount of noise contained in IC6. In a similar way, the other eleven non-artifact ICs are also denoised and the artifact free signal is reconstructed by a recombination of the selected denoised ICs as mentioned earlier. The panels from top to bottom of fig.3.18 shows the MCG butterfly plot [43] (superposition of MCG data for all channels) for a single unaveraged cardiac cycle obtained from the

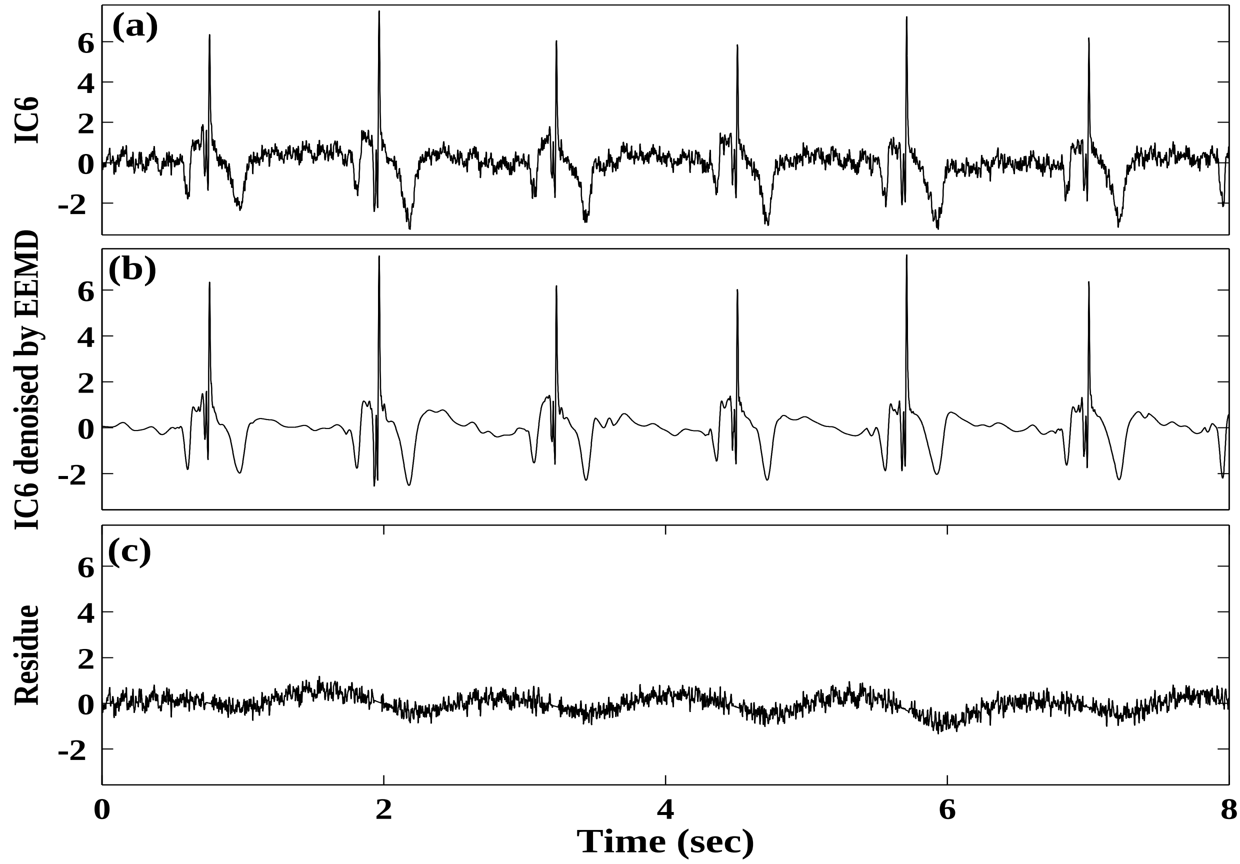

Figure 3.17: As an illustration, the top panel shows the sixth independent component (IC6) and the middle panel shows the IC6 denoised by the EEMD method. The bottom panel shows the residue obtained by taking the difference between the raw IC6 and the denoised IC6. The ordinate indicates the magnetic field gradient (pT/cm). The residual noise contained in the sixth independent component is effectively removed by the EEMD method.

raw data (without denoising) and after using preprocessing algorithms such as ICA alone, wICA, and EEMD-ICA to denoise the raw data. It is clearly seen that the noise is much reduced and the **signal quality significantly enhanced when the EEMD-ICA based denoising method is used** as compared to the other methods.

The preprocessing step of noise reduction is eventually expected to result in better localization of the source. The effect of signal denoising (by the three ICA based denoising methods viz., ICA, wICA and EEMD-ICA), on the iso-magnetic field map (MFM), the pseudo current density map (PCD) and the inverse solution based on current dipole model is presented in the **fourth chapter**.

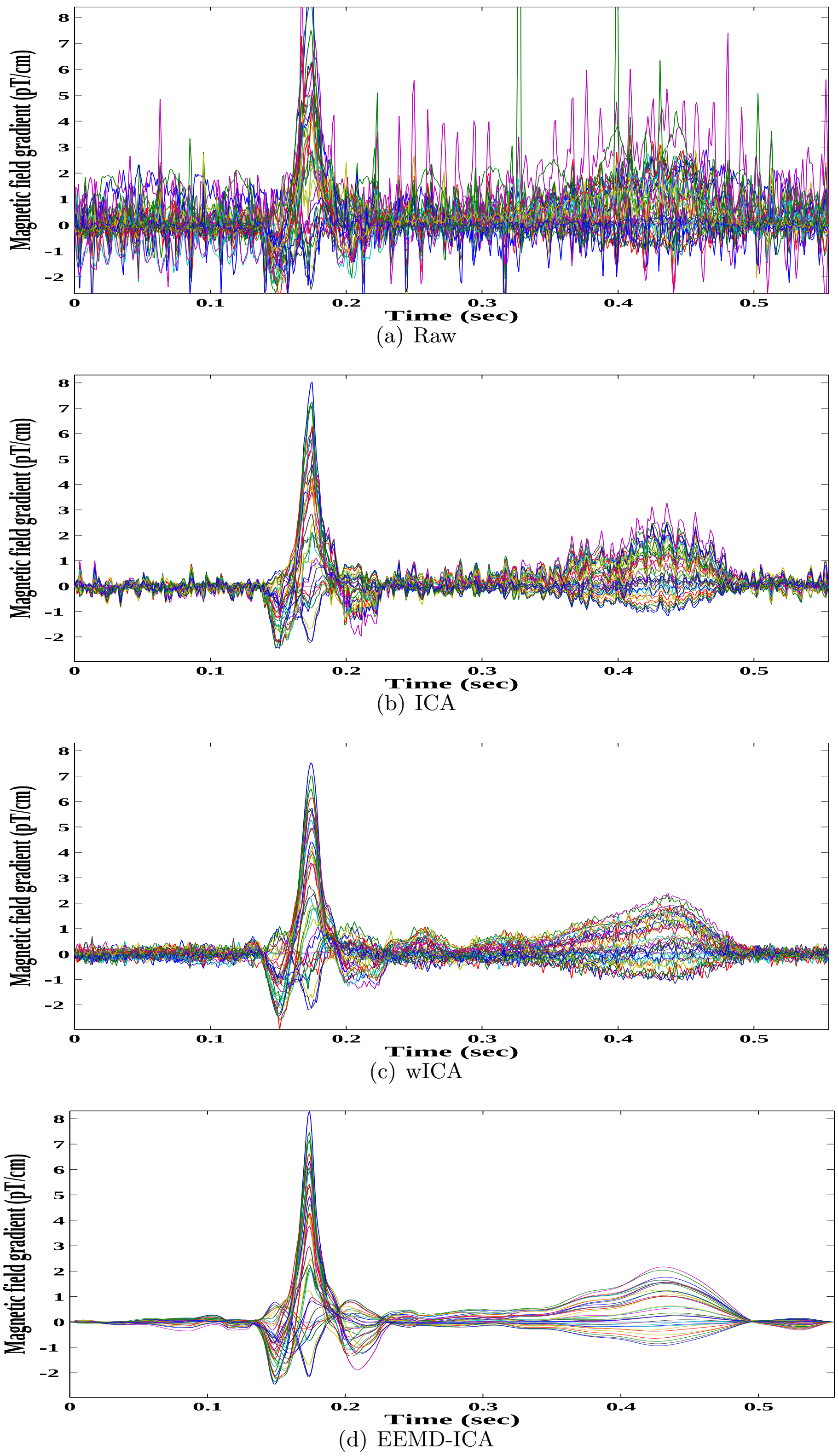

(a) Raw

(b) ICA

(c) wICA

(d) EEMD-ICA

Figure 3.18: The panels from top to bottom shows the butterfly MCG plot constructed using the raw data, and the data denoised by ICA alone, wICA and EEMD-ICA methods respectively. The EEMD-ICA is seen to result in an effective noise reduction compared to the ICA alone and wICA methods.

3.12 Conclusions

We adopted the EEMD based method to denoise the MCG data and eliminate the baseline drift contained in it. The noise amplitudes employed in the EEMD method, to prevent mode mixing, were derived from the standard deviation of second order derivative of the signal (SDS), as against the conventional use of 0.1-0.4 times the standard deviation of the signal to be denoised. This resulted in a reduction in the number of trials required to suppress the uncorrelated noise when ensemble average is taken and also aided in the reconstruction of the pristine signal with substantially reduced errors.

In the threshold based denoising, the use of interval thresholding method smoothened the discontinuities in the signal, which have a tendency to appear when direct thresholding is used, and further enhanced the SNR. We demonstrated the effective use of EEMD technique to eliminate the low and high frequency baseline drift contained in the experimentally measured MCG signal. As an illustration, the EEMD technique was used for the elimination of the high frequency random noise, power line frequency interference at 50 Hz and its harmonics etc. in the measured MCG data, and the results were compared with those obtained by wavelet and ICA based denoising methods. Our results show that the performance of EEMD was superior to that of both wavelet and ICA based methods.

We have used a combination of EEMD and ICA methods to denoise the multichannel MCG data and have compared the results with those obtained by the other methods conventionally used for artifact suppression such as standalone ICA and also the wavelet enhanced ICA (wICA) artifact suppression methods. We note that the EEMD-ICA technique is superior for suppressing the artifacts and for enhancing the signal quality when compared to the standalone ICA and the wICA methods. In the context of multichannel MCG data with a large number of channels, EEMD-ICA method also has the advantage of lower computational burden compared to that for the standalone EEMD by requiring the application of EEMD to each independent component instead of each channel. The EEMD-ICA can be used for the analysis of beat-to-beat cardiac data to detect the abnormal changes from one beat to the other without requiring the conventional averaging techniques to enhance the signal-to-noise ratio.

Bibliography

[1] P.S. Addison. Wavelet transforms and the ECG: a review. *Physiol. Meas.* **26** (2005) R155 - R199.

[2] A. Hyvärinen and E. Oja. Independent Component Analysis: Algorithms and Applications. *Neural Networks.* **13** (4-5) (2000) 411 - 430.

[3] L. Dang-Ting, T. Ye, R. Yu-Feng, Y. Hong-Wei, Z. Li-Hua, Y. Qian-Sheng and C. Geng-Hua. A novel filter scheme of data processing for SQUID-based Magnetocardiogram. *Chinese Phys. Lett.* **25** (2008) 2714 - 2717.

[4] S. Taulu, J. Simola and M. Kajola. Applications of the Signal Space Separation Method. *IEEE Trans. Sig. Proc.* **53** (9) (2005) 3359 - 3372.

[5] S. Luo and P. Johnston. A review of electrocardiogram filtering. *J. Electrocardiol.* **43** (2010) 486 - 496.

[6] R.P. Narwaria, S. Verma and P.K. Singhal. Removal of baseline wander and power line interference from ECG Signal - A survey approach. *Int. J. Electron. Eng.* **3** (2011) 107 - 111.

[7] K. Kim, Y.H. Lee, H. Kwon, J.M. Kim, I.S. Kim and Y.K. Park. Averaging algorithm based on data statistics in Magnetocardiography. *Neurol. Clin. Neurophysiol.* **42** (2004) 1 - 4.

[8] S. Yamada, K. Kuga, K. On and I. Yamaguchi. Noninvasive recording of His potential using Magnetocardiograms. *Circ. J.* **67** (2003) 622 - 624.

[9] Z. Xue-Min, R. Yu-Feng, Y. Hong-Wei, Z. Shi-Ping, C. Geng-Hua, Z. Li-Hua and Y. Qian-Sheng.

A digital filtering scheme for SQUID based Magnetocardiography. *Chinese Phys.* **15** (2006) 100 - 104.

[10] V. Tiporlini, N. Nguyen and K. Alameh. Adaptive noise canceller for Magnetocardiography. *IEEE Proc. HONET.* (2011) 359 - 363. doi: 10.1109/HONET.2011.6149770.

[11] V.S. Poudov. The comparison of possibilities of continuous and discrete wavelet transforms for MCG data processing. *IEEE Proc. Electron Devices and Materials.* (2004) 138 - 142. doi: 10.1109/PESC.2004.241212.

[12] Y. Dong, H. Shi, J. Luo, G. Fan and C. Zhang. Application of wavelet transform in MCG-signal denoising. *Mod. Appl. Sci.* **4** (2010) 20 - 24.

[13] B. Arvinti, A. Isar, R. Stolz and M. Costache. Performance of Fourier versus Wavelet analysis for magnetocardiograms using a SQUID-acquisition system. *IEEE Proc. SACI.* (2011) 69 - 74. doi: 10.1109/SACI.2011.5872975.

[14] J.Q. Campbell, H. Eswaran, J.D. Wilson, P. Murphy, C.L. Lowery and H. Preissl. Fetal Magnetocardiographic Source Separation : Independent Component Analysis Techniques and Signal-Space Projection. *IJBEM.* **7**(1) (2005) 329 - 333.

[15] S. Comani, D. Mantini, G. Alleva, S.D. Luzio and G.L. Romani. Fetal magnetocardiographic mapping using independent component analysis. *Physiol. Meas.* **25** (2004) 1459 - 1472.

[16] S. Comani, D. Mantinic, P. Pennesic, A. Lagattab and G. Cancellieri. Independent component analysis: fetal signal reconstruction from magnetocardiographic recordings. *Computer Methods and Prog. in Biomed.* **75** (2004) 163 - 177.

[17] K. Kobayashi, Y. Uchikawa, T. Simizu, K. Nakai and M. Yoshizawa. The rejection of magnetic noise from the wire using independent component analysis for magnetocardiogram. *IEEE Trans. Magnetics.* **41** (2005) 4152 - 4154.

[18] D. DiPietroPaolo, H.P. Müller, G. Nolte and S.N. Erné. Noise reduction in magnetocardiography by singular value decomposition and independent component analysis. *Med. Biol. Eng. Comput.* **44**(6) (2006) 489 - 499.

[19] N.E. Huang, Z. Shen, S.R. Long, M.C. Wu, H.H. Shih, Q. Zheng, N.C. Yen, C.C. Tung and H.H. Liu. The empirical mode decomposition and the Hilbert spectrum for nonlinear and non-stationary time series analysis. *Proc. R. Soc. Lond. A.* **454** (1998) 903 - 995.

[20] B. Weng, M.B. Velasco and K.E. Barner. ECG Denoising Based on the Empirical Mode Decomposition. *IEEE proc. EMBS.* (2006) 1 - 4. doi:10.1109/IEMBS.2006.259340.

[21] S. Pal and M. Mitra. Empirical mode decomposition based ECG enhancement and QRS detection. *Computers in Biol. and Med.* **42** (2012) 83 - 92.

[22] Z. Wu and N.E. Huang. Ensemble empirical mode decomposition method: A noise-assisted data analysis method. *Advances in Adaptive Data Analysis.* **1** (2009) 1 - 41.

[23] T. Wang, M. Zhang, Q. Yu and H. Zhang. Comparing the applications of EMD and EEMD on time-frequency analysis of seismic signal. *J. Appl. Geophys.* **83** (2012) 29 - 34.

[24] N.E. Huang and Z. Wu. A review on Hilbert-Huang transform: Method and its applications to geophysical studies. *Rev. Geophys.* (RG2006) 46:doi: 10.1029/2007RG000228.

[25] P. Flandrin, G. Rilling and P. Gonçalvés. Empirical mode decomposition as a filter bank. *IEEE Sig. Process. Lett.* **11** (2004) 112 - 114.

[26] Z. Wu and N.E. Huang. A study of the characteristics of white noise using the empirical mode decomposition method. *Proc. R. Soc. Lond. A.* **460** (2004) 1597 - 1611.

[27] P. Flandrin, P. Gonçalvás and G. Rilling. "EMD equivalent filter banks, from interpretation to applications." In: Hilbert-Huang Transform: Introduction and Applications, edited by N. E. Huang and S.S.P. Shen. Singapore: *World Scientific*, vol.**5**, 2005, pp 57 - 74.

[28] J. Zhang, R. Yan, R.X. Gao and Z. Feng. Performance enhancement of ensemble empirical mode decomposition. *Mech. Sys. Sig. Process.* **24** (2010) 2104 - 2123.

[29] Z. Zhidong, J. Liu and S. Wang. Denoising ECG signal based on ensemble empirical mode decomposition. *Proc. SPIE. 8285* (ICGIP 2011) doi:10.1117/12.913515.

[30] Y. Kopsinis and S. McLaughlin. Development of EMD-based denoising methods inspired by wavelet thresholding. *IEEE Trans. Sig. Process.* **57** (2009) 1351 - 1362.

[31] K.M. Chang. Arrhythmia ECG noise reduction by ensemble empirical mode decomposition. *Sensors.* **10** (2010) 6063 - 6080.

[32] A. Hyvärinen and E. Oja. A Fast Fixed-Point Algorithm for Independent Component Analysis. *Neural Computation.* **9**(7) (1997) 1483 - 1492.

[33] C. Parasakthi, Rajesh Patel, S. Sengottuvel, N. Mariyappa, K. Gireesan, M.P. Janawadkar and T.S. Radhakrishnan. Establishment of 37 channel SQUID system for magnetocardiography. *AIP Conf. Proc.* **1447** (2012) 871 - 872.

[34] C.J. James and C.W. Hesse. Independent component analysis for biomedical signals. *Physiol. Meas.* **26** (2005) R15 - R39.

[35] S. Sengottuvel, C. Parasakthi, N. Mariyappa, Rajesh Patel, K. Gireesan, M.P. Janawadkar, T.S. Radhakrishnan and T.R. Muralidharan. Enhancing the reliability in the non-invasive measurement of the His bundle magnetic field using a novel signal averaging methodology. *Ann. Noninvasive Electrocardiol.* **17**(3) (2012) 186 - 194.

[36] U.R. Acharya, K.P. Joseph, N. Kannathal, C.M. Lim and J.S. Suri. Heart rate variability: a review. *Med. Bio. Eng. Comput.* **44** (2006) 1031 - 1051.

[37] J.V. Stone. Independent component analysis: an introduction. *TRENDS in Cognitive Sci.* **6** (2002) 59 - 64.

[38] N.P. Castellanos and V.A. Makarov. Recovering EEG brain signals: Artifact suppression with wavelet enhanced independent component analysis. *J. Neurosci. Methods.* **158** (2006) 300 - 312.

[39] B. Mijović, M. De Vos, I. Gligorijević, J. Taelman and S. Van Huffel. Source Separation From Single-Channel Recordings by Combining Empirical-Mode Decomposition and Independent Component Analysis. *IEEE Trans. Biomed. Engg.* **57** (2010) 2188 - 2196.

[40] M.T. Akhtar, W. Mitsuhashi and C.J. James. Employing spatially constrained ICA and wavelet denoising for automatic removal of artifacts from multichannel EEG data. *Signal Processing.* **92** (2012) 401 - 416.

[41] G. Inuso, F. La Foresta, N. Mammone and F.C. Morabito. Wavelet-ICA methodology for efficient artifact removal from Electroencephalographic recordings. *IJCNN 2007 Conf. Proc.* (2007) 1524 - 1529.

[42] N. Mammone, F.L. Foresta and F.C. Morabito. Automatic Artifact Rejection From Multichannel Scalp EEG by Wavelet ICA. *IEEE SENSORS.* **12** (2012) 533 - 542.

[43] W. Haberkorn, U. Steinhoff, M. Burghoff, O. Kosch, A. Morguet and H. Koch. Pseudo current density maps of electrophysiological heart, nerve or brain function and their physical basis. *Biomagn. Res. Technol.* **4:5** (2006).

4 Cardiac source estimation from MCG

This chapter presents the Equivalent Current Dipole (ECD) model for the cardiac source and discusses two source estimation methods, viz., Pseudo Current Density (PCD) maps and the solution of the inverse problem in the context of an Equivalent Current Dipole (ECD) model. For the latter, a simple nonlinear least square optimization technique with sets of pseudo-random numbers as initial estimates of source parameters for solving the inverse problem is described. The validation of the proposed method, using both simulated as well as experimentally measured magnetic field data corresponding to a small current carrying source coil at a known location is presented. The application of the method to the analysis of the experimentally measured MCG data on a human subject is described. The results of investigations on the effect of noise on the source localization accuracies for the simulated data for both single and two ECDs are presented. This chapter also discusses the effect of signal pre-processing techniques on the magnetic field maps, inferred pseudo current density maps and the solution of the inverse problem.

4.1 Equivalent Current Dipole (ECD) model

In the context of Magnetocardiography (MCG), the underlying source, which is related to the electrical activity of the heart, has to be reconstructed from the measured magnetic field distribution over the anterior surface of a thorax. A physiologically plausible and mathematically simple model [1], known as the **Equivalent Current Dipole** (ECD) representing the cardiac source is widely used, in this context, because of its simplicity and robustness. This model assumes that the flow of current is confined to an infinitesimally small volume element at any given instant of time. In MCG measurements, the normal component of the magnetic field generated by the equivalent current dipole $\vec{Q}$ located in a horizontally layered conductor is given by [2],

$$B_z = \left(\frac{\mu_0}{4\pi} \frac{\vec{Q} \times (\vec{r} - \vec{r}^{'})}{|\vec{r} - \vec{r}^{'}|^3} \right) \cdot \vec{e}_z \tag{4.1}$$

where μ_0 is the permeability of the free space, $\vec{Q}$ is the dipole moment vector, $\vec{r}$ is the position vector of the measurement location and $\vec{r}^{'}$ is the position vector of the source inside the conductor. However, all the experimental MCG measurements carried out, in our laboratory, were using the first order axial gradiometer; hence the data is fitted to the field gradient of the ECD model, i.e.,

$$\frac{\partial B_z}{\partial z} = -\frac{3\mu_0}{4\pi} \sum_{i=1}^{n} \frac{(z - z_i^{'})[Q_{ix}(y - y_i^{'}) - Q_{iy}(x - x_i^{'})]}{((x - x_i^{'})^2 + (y - y_i^{'})^2 + (z - z_i^{'})^2)^{5/2}} \tag{4.2}$$

Here, n is the number of dipoles, $(x_i^{'}, y_i^{'}, z_i^{'})$ and (Q_{ix}, Q_{iy}) are the position coordinates and x and y components of the dipole moment of the i^{th} dipole. It may be noted that for a dipole embedded within a conductor parallel to the X-Y plane, Q_z component of the dipole does not contribute to the normal component B_z of the magnetic field, so that five parameters describe the model completely.

There are two cardiac source estimation methods widely used in the context of MCG, which have been adopted in this thesis, viz., i) Pseudo Current Density (PCD) maps [3, 4] and ii) source reconstruction by solving the inverse problem [5, 6]. We discuss the PCD maps and the inverse problem in the subsequent sections 4.2 and 4.3.

4.2 Pseudo Current Density Maps

The pseudo-current density (PCD) map provides an approximate image of a possible 2D representation of the 3D current density distribution associated with the source. Hosaka-Cohen transformation [3] seeks to transform the measured magnetic field distribution in the sensor plane to a possible representation of the source in the form of pseudo-current density distribution in the source plane using the partial derivatives of the z component of the magnetic field B_z. The pseudo-current density (PCD) maps [4] or the current arrow maps [7] allow the source to be visualized and portrayed in the form of the underlying current density distribution, which are often found to be close to the location of the actual electrophysiological activity. Accordingly, the **source may**

be assumed to be located at a place where maximum current is indicated in the PCD map. The pseudo current density $\vec{c}(x, y)$ is derived from the measured values of B_z by the following equation [3],

$$\vec{c} = \frac{\partial B_z}{\partial y}\vec{e_x} - \frac{\partial B_z}{\partial x}\vec{e_y} \tag{4.3}$$

where, $\vec{e_x}$ and $\vec{e_y}$ are the unit vectors in x and y directions respectively. The amplitude and the direction of the pseudo current density arrows $\vec{c}(x, y)$ are determined by the spatial derivatives of B_z.

The amplitude of $\vec{c}$ is coded as the length of the arrow and the underlying false color scaled by the amplitude $|\vec{c}|$ enhances the visualization of information. As an illustration, the Magnetic Field Map (MFM) obtained from Eq.4.1 for the equivalent current dipole source parameters, $|Q| = 1\ \mu Am,\ x = 0.1\ m,\ y = 0.1\ m$, and $z = -0.1\ m$ is shown in fig.4.1(a), while the corresponding PCD map obtained from the spatial derivatives of the magnetic field distribution (as in Eq.4.3) is shown in fig.4.1(b). The assumed location and orientation of the Equivalent Current Dipole (ECD), indicated by tip and direction of the arrow respectively in the Magnetic Field Map (MFM), are reconstructed in the Pseudo Current Density (PCD) map where maximum current flow (red color) is shown. It is evident from this demonstration that the PCD maps are useful in portraying the possible source current density distribution. It may also be noted that the PCD maps do not reproduce the point like character of the current dipole; rather, it is analogous to the characteristic point spread function of the source.

In the following section, we briefly discuss the solution of the inverse problem in the context of sources which may be identified by a small number of parameters that may be estimated through the usual nonlinear optimization techniques. However, a major challenge in obtaining a reliable solution to the inverse problem by this method is that the solution may be trapped in a local minimum.

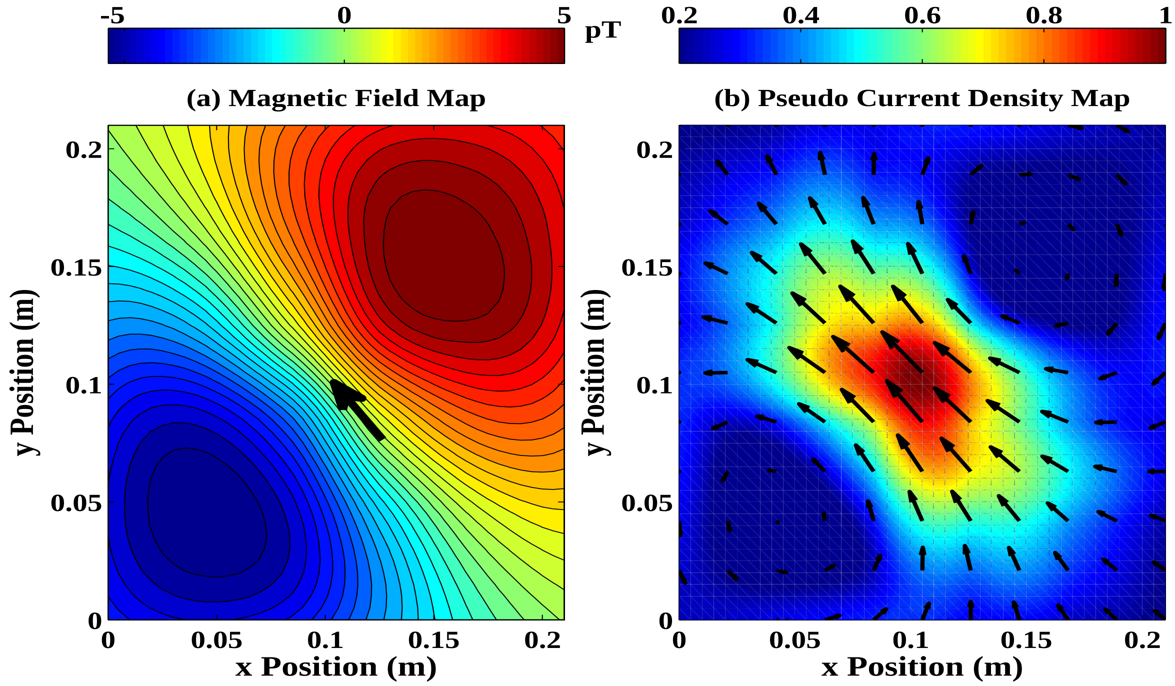

Figure 4.1: Magnetic field map (MFM) simulated for an Equivalent Current Dipole (ECD) with the source parameters, $|Q| = 1\ \mu Am,\ x = 0.1\ m,\ y = 0.1\ m$, and $z = -0.1\ m$ (from Eq.4.1) and (b) the corresponding Pseudo Current Density (PCD) map constructed from the spatial derivatives of B_z (refer Eq.4.3). The colorbar scale in the MFM indicates the field values (B_z). In the colorbar scale for the PCD map, the maximum current is normalized to unity. The arrow indicates the direction of the Equivalent Current Dipole (ECD), while the length of the arrow in the PCD map indicates the strength of the current at the particular spatial location. It may be noted that in this simulated case, the maximum current flow (indicated by red), in the PCD map does indeed correspond to the actual location of the current dipole. The assumed location and orientation of the Equivalent Current Dipole (ECD), indicated by tip and direction of the arrow respectively in the Magnetic Field Map (MFM), are reconstructed in the Pseudo Current Density (PCD) map which shows the maximum current flow (red color) at the assumed actual location of the dipole. The utility of the PCD maps for portraying the possible source current density distribution is clear from the above demonstration.

4.3 Inverse problem on MCG data

The term forward problem relates to a theoretical model with a given set of parameters (as in Eq.4.1) which may be used for predicting the experimental observations (magnetic field intensity at the position of each sensor), whereas the term inverse problem relates to estimating the values of the source parameters from the experimental observations. However, the inverse problem is, in general, ill-posed (i.e., sensitive to measurement errors) and the solution is not unique (i.e., a large number of source configurations may result in a nearly identical magnetic field distribution to within the error of measurement) [1, 2]. Nevertheless, it is important to infer a physically admissible source configuration which can account for the observed magnetic field distribution and several approaches have been used by researchers for this purpose. The non-uniqueness of the inverse problem, in ECG/MCG, is overcome by introducing realistic constraints on the possible solutions [1], in order to exclude all solutions except the one that is confined to a limited class of source configurations.

Many algorithms have been adopted in the literature for the solution of the inverse problem by iteratively refining an initial estimate of source parameter values (dipole position and strength) until the discrepancy between the measured magnetic field distribution and that computed using the final set of parameter values in a forward model reaches a minimum value [6]. These include, for example, methods such as Levenberg-Marquardt (LM) [8], Nelder-Mead (NM) downhill simplex search [9], MUltiple Signal Identification and Classification (MUSIC) technique [10], simulated annealing [11], genetic algorithms [12] etc., to reliably estimate the parameters of the Equivalent Current Dipole (ECD).

In the present study, we adopted the simple nonlinear least square approach to solve the inverse problem with the Equivalent Current Dipole (ECD) model as the cardiac source. In the nonlinear least square technique, the estimation of unknown parameters (five parameters-three coordinates of position (x, y, z) and two components of dipole moment (Q_x, Q_y, Q_z) -of the ECD embedded in a horizontally layered conductor (refer Eq.4.2)) is achieved by means of minimizing the square of the difference between the actual experimental measurements and the predictions from the corresponding model for the given set of source parameters. The best-fit parameters are found by means of an iterative procedure [6] such as the Levenberg-Marquardt (LM) algorithm or Nelder-Mead (NM) downhill simplex search algorithm as the magnetic field depends nonlinearly on the ECD position. However, the nonlinear optimization solutions with Levenberg-Marquardt (LM) and Nelder-Mead (NM) downhill simplex search algorithms may in general depend on the initial values [13] assumed for the parameters to be estimated. If the initial guess lies far from the actual solution, then **the solution may be trapped in a local minimum and this is the main pitfall of iterative minimization algorithms**. Towards this, we have proposed and used a set of pseudo-random numbers as an initial guess for the values of the parameters of three positional variables (x, y, z) and two moment variables (Q_x, Q_y) that characterize the Equivalent Current Dipole (ECD) and carried out successively nonlinear optimization using Levenberg-Marquardt algorithm for different sets of pseudo-random numbers. The different sets of pseudo-random numbers have been used, as an initial guess, in order to avoid the solution getting trapped in a local minimum value. We also imposed certain realistic spatial constraints on the solution of the inverse problem to choose the physically relevant solution as discussed subsequently in the forthcoming section 4.4.

4.4 Methodology for solving inverse problem

The methodology for reconstructing the source parameters of the Equivalent Current Dipole (ECD) was implemented using MATLAB. To have an estimate of the quality of agreement between the measured and calculated (with the source parameters inferred from nonlinear least square optimization) data, R-Square (RSQ) and Root Mean Square Error (RMSE) are evaluated [14].

$$RSQ = \left(1 - \frac{\sum_{i=1}^{k}(B'_{im} - B'_{ic})^2}{\sum_{i=1}^{k}(B'_{im} - \bar{B}'_{m})^2}\right) * 100 \quad (4.4)$$

$$RMSE = \sqrt{\frac{1}{N}\sum_{i=1}^{k}(B'_{im} - B'_{ic})^2} \quad (4.5)$$

Here, B'_{im} and B'_{ic} represent the measured and the calculated $\frac{\partial B_z}{\partial z}$ values at i^{th} spatial location (sensor position). $\bar{B}'_m$ is the mean of the measured magnetic field gradient $\frac{\partial B_z}{\partial z}$.

The method comprises of the following steps:

1. Choose a set of pseudo random numbers for the position coordinates and the moment parameters as an initial guess
2. Fit the spatial distribution of $\frac{\partial B_z}{\partial z}$ values to the dipole model and search for optimal dipole parameters using the nonlinear least square optimization method based on Levenberg-Marquardt (LM) algorithm and calculate the R-square (RSQ) and Root Mean Square Error (RMSE)
3. Repeat the steps (1) and (2) for at least fifty different sets (this number can be varied, but fifty sets were found to be adequate in all cases) of pseudo random numbers

4. From amongst the distribution of RSQ values, the physical parameters (x, y, z, Q_x, Q_y) that result in maximum RSQ (within a 4% band around the maximum) are accepted with the constraint that the spatial location(s) of the dipole(s) lie within the region of space directly below the projection of the total sensor coverage area in the measurement plane

5. If multiple solutions come within the region of space as restricted above, then the solution with maximum R-square (RSQ) will be selected. Correspondingly, solutions based on RSQ with unphysical parameters will be rejected

In the nonlinear least square optimization technique, the maximum number of iterations (10^6) and the absolute tolerance (10^{-6}) were fixed. If the solution converges to within the prescribed absolute tolerance before reaching the maximum number of iterations, the loop will terminate. If it does not converge, the loop will terminate after the execution of the prescribed maximum number of iterations most often resulting in low values of RSQ. The results of such iterations are excluded from any further consideration. The computation time for convergence to the final solution was less than thirty seconds (in a PC configuration comprising Intel(R) Core(TM)2 Duo CPU with a speed of 3 GHz and 1.96 GB RAM capacity) for a total of fifty independent trials with different sets of pseudo-random numbers.

As mentioned earlier in the section 4.3, the nonlinear least square technique is sensitive to initial guess values. We demonstrate this by simulating the magnetic field distribution for single Equivalent Current Dipole (ECD) obtained from Eq.4.2 at different spatial locations (say, at the nodal points of a 6×6 square lattice with a spacing of 4.2 cm). The detailed discussion for the simulation has already been presented in section 4.7. The method discussed above was used for reconstructing the source parameters of the simulated data using independent sets of pseudo-random numbers as initial guess in fifty trials and the index of fit R-square (RSQ) was calculated for each trial. To see the sensitivity of R-square (RSQ) to the dipole parameters, the changes in RSQ when each dipole parameter is varied in the neighbourhood of its optimal value (while keeping all others fixed) were calculated and these results are shown in fig.4.2. The smooth variation of RSQ with dipole parameters helps to provide confidence in the estimated values of dipole parameters. It may also be noted that if one starts with initial guess values which are not sufficiently close to the true solution, the algorithm may converge to a solution which may not be physically consistent. Fig.4.2 (bottom right panel) illustrates the histogram of the RSQ values constructed when fifty trials, each corresponding to a different set of pseudo-random numbers serving as the initial guess values of parameters, are carried out. It is also evident from this figure that some sets of initial values fail to converge to the actual solution and result in rather poor values of RSQ; such trials are ignored in the proposed method. It may be noted that the histogram illustrates the spread in the resulting R-square (RSQ) values when fifty trials are conducted and we choose the physical parameters that result in maximum RSQ (within a 4% band around the maximum) with the constraint that the spatial location(s) of the dipole(s) lie within the region of space directly below the projection of the total sensor coverage area in the measurement plane.

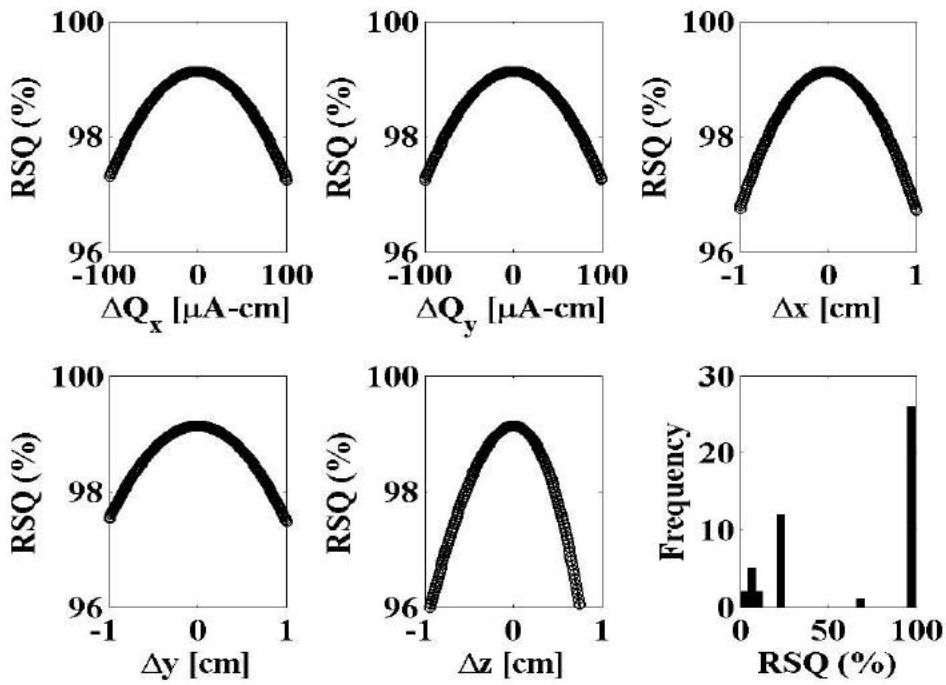

Figure 4.2: The variation in R-square (RSQ) when a dipole parameter is varied around its optimal value. The bottom right panel shows the histogram of RSQ values resulting from fifty trials with independent sets of pseudo-random numbers as initial values for the source parameters in the nonlinear optimization technique used for source analysis from the data presented in section 4.7. It may be noted that, if one starts with initial values which are not sufficiently close to the true solution, the algorithm may converge to a solution which may not be physically consistent. The histogram of RSQ values reveals that some sets of initial values fail to converge to the actual solution and result in rather poor values of RSQ.

To validate the methodology, the experimental data corresponding to the magnetic field distribution (a) produced by a current carrying source coil at the known location and (b) the experimentally measured MCG data were used.

4.5 Application to experimental data: Locating a magnetic dipole

A small 10 turn current carrying copper coil of 4 mm diameter was approximated as a **point source (or magnetic dipole)** whose magnetic field distribution was experimentally measured using the SQUID system. The source coil was initially placed under the centre of the cryostat (13 channel MCG system), which is taken to be the origin of the coordinate system in these studies. A sinusoidally varying current at a frequency of 23 Hz was passed through the source coil and the output of each SQUID channel was phase sensitively detected using a lock-in-amplifier. The coil was then displaced to a new position in the $X-Y$ plane and the resulting magnetic field distribution was recorded. Subsequently, the coil was kept at a fixed location in the $X-Y$ plane and its position along the z-direction was adjusted by either raising or lowering the cryostat by a known amount and the measurements were repeated. Since the coil diameter (4 mm) is much smaller compared to the distance between the coil and the plane of the sensor array (which was varied between 40 to 60 mm during the measurement), the field produced by the coil may be approximated to that of a point dipole. The observed experimental data was fitted in each case by modelling the source coil as a point magnetic dipole with a field given by,

$$\vec{B} = \frac{\mu_0}{4\pi}\left[\frac{3(\vec{m}\cdot\vec{r})\vec{r} - r^2\vec{m}}{r^5}\right] \tag{4.6}$$

The component B_z of the magnetic field produced by a dipole oriented along the z-axis is given by

$$B_z(x,y,z) = \frac{\mu_0 m_z}{4\pi}\left(\frac{2(z-z_i^{'})^2 - (x-x_i^{'})^2 - (y-y_i^{'})^2}{((x-x_i^{'})^2 + (y-y_i^{'})^2 + (z-z_i^{'})^2)^{5/2}}\right) \tag{4.7}$$

Here, $(x_i^{'}, y_i^{'}, z_i^{'})$ and m_z are the position and dipole moment of the source coil. Since axial gradiometers were used in the experimental set up, the data was fitted to the axial gradient $\frac{\partial B_z}{\partial z}$ produced by a dipole oriented along the z-axis. The position parameters and the magnetic dipole moment values inferred by fitting the data are compared with the known values corresponding to the source coil as shown in fig.4.3. It is evident from fig.4.3 that **the algorithm is able to correctly infer the dipole position within a localization error of ±2 mm**. We have also found that the inferred magnetic moment of the dipole was in agreement with the value of the moment estimated from the area of the coil and the current passing through it.

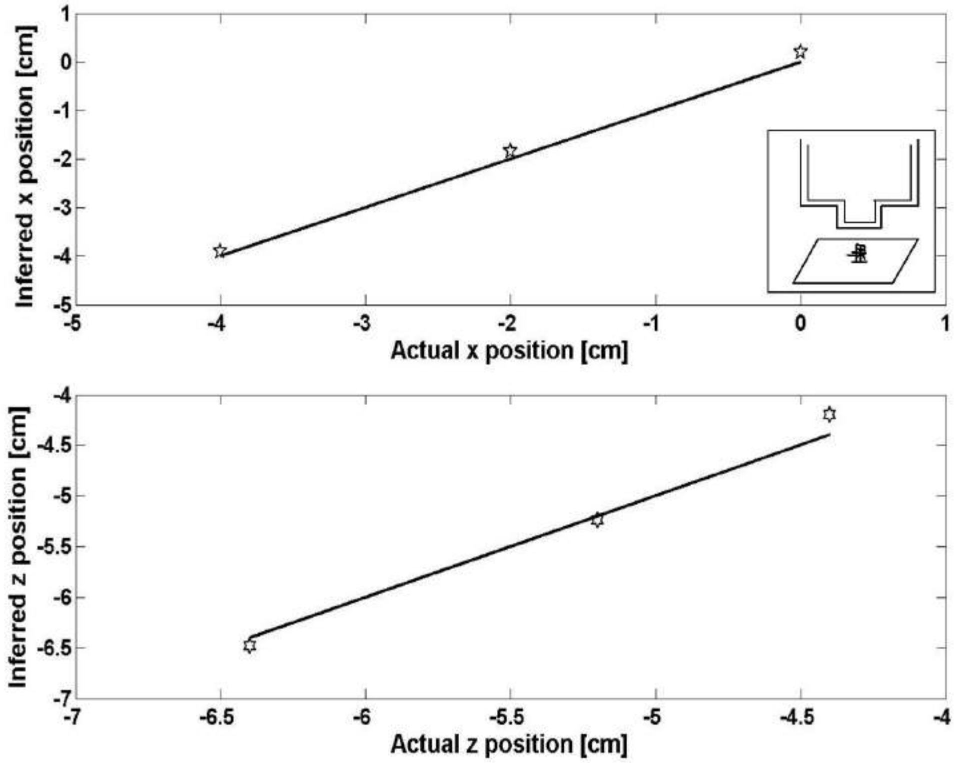

Figure 4.3: The top panel represents the inferred source coil position when it was displaced along the x direction keeping (y,z) constant at (0,-5.2) cm and the bottom panel shows the inferred source coil position when it was displaced along the z direction keeping (x,y) constant at (-1,1) cm. The solid line indicates the actual position and $\star$ indicates the position inferred by solving the inverse problem using the proposed method. The inset schematically shows the source coil placed under the SQUID based system. It is seen that the algorithm correctly infers the position of the source coil within a localization error of ±2 mm.

4.6 Application to experimental MCG data

The method was applied to the MCG data initially measured on a healthy human subject, using a four channel SQUID based system, inside a magnetically shielded room. Fig.4.4 shows the grid pattern of the measurement locations superimposed on a representation of the chest surface to indicate the measurement positions relative to the heart, which is schematically shown as inlay. The origin of the coordinate system is taken to lie in the plane containing the sensors for measurements. The measurements were carried out sequentially at a total of 36 locations on a 6 × 6 square lattice covering an area of 21 cm × 21 cm, as described in chapter 2. The model for single equivalent current dipole was fitted to the measured MCG data at several instants of time such as when the cardiac cycle is passing through the peaks corresponding to ventricular depolarization (R-wave) and repolarization (T-wave) respectively (fig.4.5(a)). The measured and the reconstructed Magnetic Field Map (MFM) from the single Equivalent Current Dipole (ECD) fit at the instant of R-peak is shown in fig.4.5(b). The single dipole fit gives a reasonable and physically meaningful solution for the measured MCG at the peak of ventricular depolarization as well as repolarization. In order to have further confidence in the localization methodology used, we have carried out

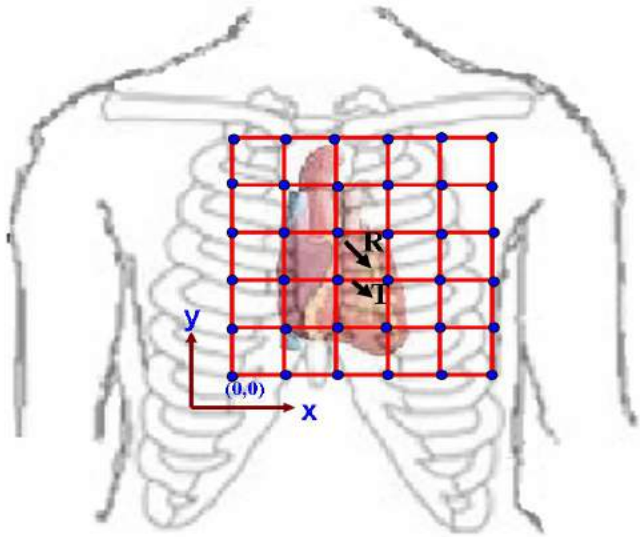

Figure 4.4: The two dimensional thoracic surface of a subject showing the location of the grid pattern (the jugular notch over the sternum provided the reference) used for the MCG measurement as well as other anatomical landmarks relative to the heart. The origin of the coordinate system is taken to lie in the plane containing the sensors for measurements. The arrows represent the orientation of the respective dipoles obtained from a solution of the inverse problem at the instants of the R and T peaks.

MCG measurements on three other healthy subjects (total of four subjects, 2 males and 2 females) whose age ranged between 46 and 69 years. The spread (mean ± standard deviation) in the ECD parameters across the four subjects is listed in table 4.1.

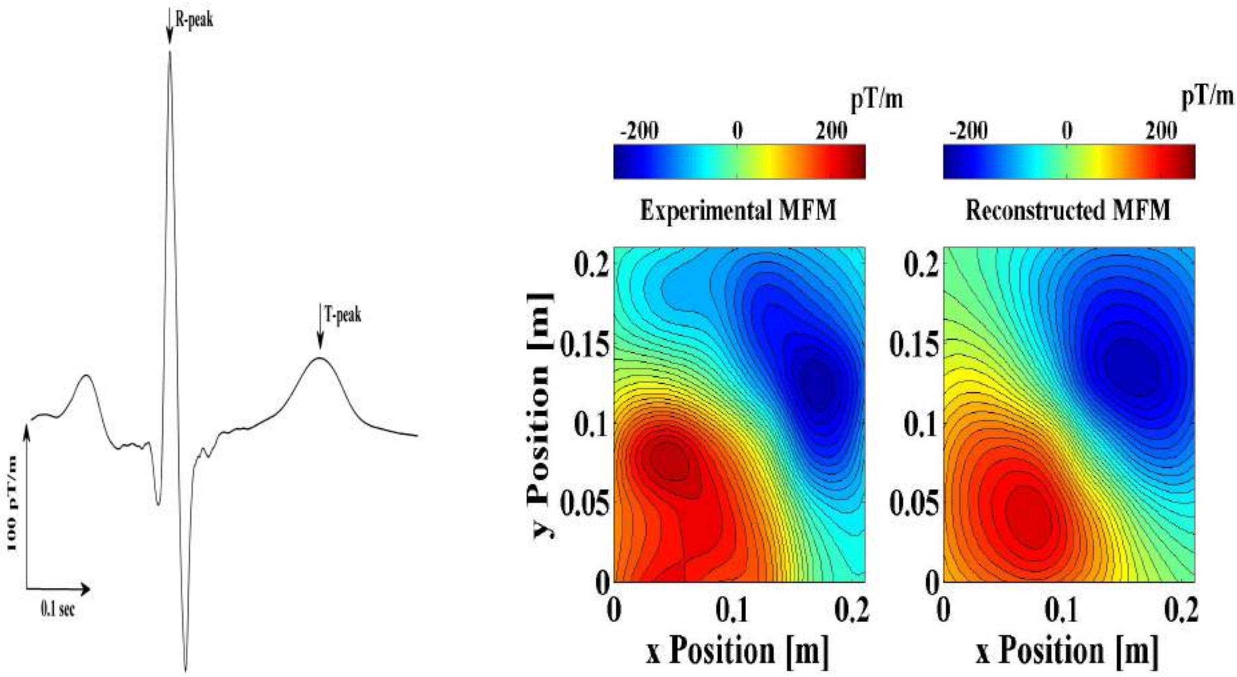

(a)

(b)

Figure 4.5: (a) The signal averaged MCG (magnetic field gradient in pT/m vs time in sec) at one anatomical location shown for illustrative purposes only; the arrows represents the time instants of the R-peak and the T-peak at which the dipole parameters were inferred (b) The Magnetic Field Map (MFM) obtained from the experimental MCG data and the reconstructed data at the instant of ventricular depolarization (R-peak) for a single ECD model for a 57 years old male subject. It may be noted that the MFM obtained through the solution of the inverse problem is in fair agreement with the experimental MFM of the MCG data.

Table 4.1: The spread in the parameters of the Equivalent Current Dipole (ECD) across the four subjects investigated. The ECD positions are indicated with respect to the sensor coordinates (see fig.4.4). The magnitude of the dipole moment is larger at the ventricular depolarization than at ventricular repolarization, as expected. The relatively large spread in the dipole strengths across four subjects may be attributed to the age and other physiological attributes of the subjects. The spread in the position of the dipole could be attributed to the differences in overall body frame.

Instant	Q_x (μA-cm)	Q_y (μA-cm)	x (cm)	y (cm)	z (cm)
R-peak	(604 ± 249)	(-487 ± 477)	(11.04 ± 0.87)	(8.80 ± 0.84)	(-12.62 ± 0.71)
T-peak	(184 ± 174)	(-18 ± 71)	(11.16 ± 0.93)	(6.77 ± 1.39)	(-12.62 ± 1.10)

One can infer from table 4.1 that, for all the subjects, the location of the ECD at both the instants of R and T peaks lies in the ventricular region (the arrows marked in fig.4.4, representing the result on one subject). The variation in the positional parameters of the dipole during the instants of time corresponding to ventricular depolarization and repolarization are well within a reasonable spread (±1 cm) across the four subjects and the values are listed in table 4.1. We can also note from the table 4.1 that the magnitude of the dipole moment is larger at the ventricular depolarization than at ventricular repolarization, as expected. **The spread in the position of the dipole could be attributed to the differences in overall body frame**; indeed there may be slight variations in the location of the source from subject to subject. The reason for the relatively large spread across the four subjects in the dipole strengths is not clear; perhaps it may be attributed to the age and other physiological attributes of the subjects. We have also observed that for all the four subjects, the y coordinate of the dipole shifts downwards (see fig.4.4, as a representative fit) as the cardiac cycle proceeds from R-wave to T-wave while the x and z coordinates remain relatively invariant. Indeed Langner et al [15] have noted that the location of the dipole for ventricular depolarization is different from that of the ventricular repolarization.

Although the validation of the method was demonstrated for the 4 channel [16] and 13 channel [17] MCG system, we note that results were similar for the 37 channel MCG system. The influence of noise on the source localization was investigated with the simulated magnetic field distribution for single and two dipoles case and the results are presented in the following sections 4.7 and 4.8.

4.7 Effect of noise on source localization: Single dipole analysis

A single Equivalent Current Dipole (ECD) and a horizontally layered conductor [2] are adopted for simulating magnetic field gradient distribution, using Eq.4.2 (for $n = 1$), at 36 positions on a square lattice in the measurement plane as indicated in fig.4.4. The simulation case is to mimic the experimental MCG measurements by four channel SQUID based MCG system which was initially used to record the magnetocardiograms on the subject's chest sequentially at a total of 36 locations on a 6×6 square lattice covering an area of 21 cm $\times$ 21 cm as indicated in fig.4.4. The assumed parameters of the ECD are contained in table 4.2. These values are typical, and are comparable to those typically obtained from an analysis of actual MCG data using the ECD as a possible source model (see table 4.1 for the source parameters obtained from the experimental MCG data). The reconstructed parameters of the ECD from the simulated magnetic field distribution, for the noiseless case, are included in table 4.2.

In order to explore the influence of noise on the localization accuracy, an additive noise of 2 to 10% was added to the value calculated using Eq.4.2. This level of noise effectively simulates the noise present in the experimental measurements. The parameters reconstructed from the simulated magnetic field values with various input noise levels are listed in table 4.2. The root mean square error (RMSE), as defined in Eq.4.5 [14], in each case is listed in table 4.2 to illustrate the impact of noise on the quality of the fit. It may be noted from table 4.2 that, the reconstruction of single

Table 4.2: Parameters obtained from the single Equivalent Current Dipole (ECD) with different input noise levels are shown. (∗) in the first line indicate the assumed parameters of the ECD. The ECD positions are indicated with respect to the sensor coordinates (see fig.4.4). The reconstruction of single equivalent current dipole is exact in the noise free case and shows a localization error of about 2 mm in the x and y coordinates and about 6 mm in the z coordinate of the dipole for the noise level of 10%. The localization error increases with increasing noise.

% of RMS Noise	Q_x (μA-cm)	Q_y (μA-cm)	x (cm)	y (cm)	z (cm)	RSQ (%)	RMSE (pT/cm)
No noise	-367.2^*	538.3^*	9.72^*	8.61^*	-11.26^*	100.00	0.0000
2	-373.3	545.5	9.70	8.56	-11.32	99.97	0.0370
4	-374.2	542.6	9.67	8.57	-11.26	99.87	0.0723
6	-385.8	563.9	9.66	8.54	-11.40	99.67	0.1165
8	-389.7	572.0	9.68	8.50	-11.47	99.54	0.1375
10	-419.8	608.0	9.62	8.40	-11.85	99.13	0.1856

equivalent current dipole using the method, discussed in section 4.4, is exact in the noise free case. It is also seen from table 4.2 that the **localization error increases with increasing noise**. The localization error of about 2 mm in the x and y coordinates and about 6 mm in the z coordinate of the dipole for the noise level of 10% is seen. It may also be noted that the error in the dipole moment also increases as the noise level increases. It may be noted that the magnetic field depends linearly on the magnetic moment parameters while the dependence on position parameters is nonlinear (refer Eq.4.1). The difference in the sensitivity of the estimated parameters to the noise level may be ascribed to this. Fig.4.6 shows the Magnetic Field Map (MFM) with 10% of additive noise obtained from the simulation along with the MFM after reconstruction from the inferred ECD parameters. It is evident from this figure that, although the algorithm reconstructs the originally assumed MFM reasonably well, the presence of noise in the input data results in an error in the source localization as seen in table 4.2.

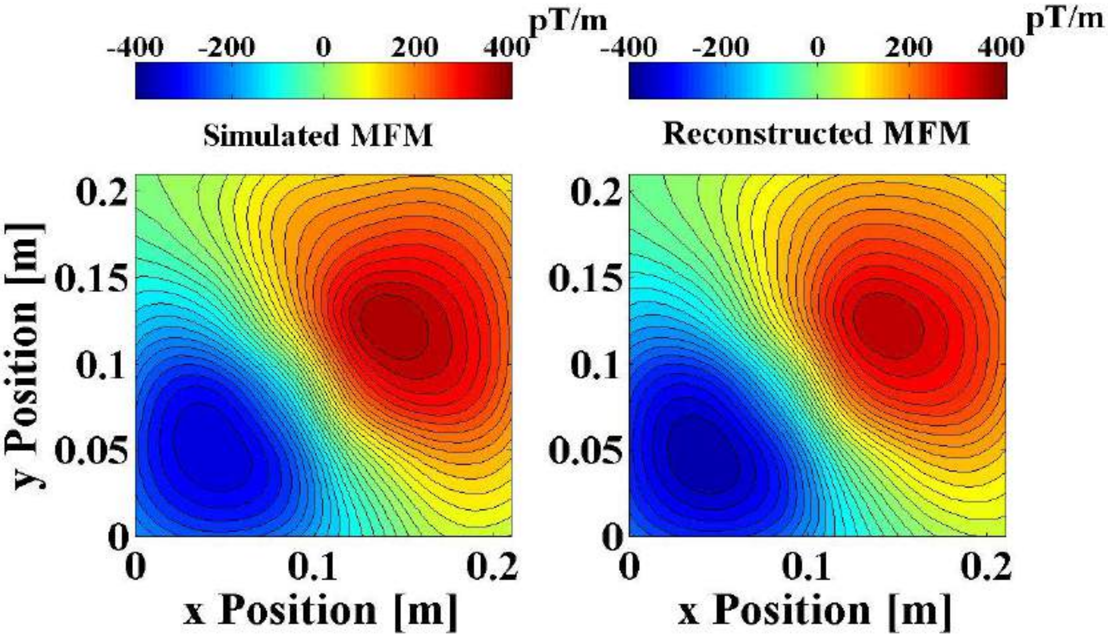

Figure 4.6: The simulated and the reconstructed spatial distribution of the magnetic field gradient $\frac{\partial B_z}{\partial z}$ for single Equivalent Current Dipole (ECD) with an additive noise of 10% of the maximum signal. It may be noted that the reconstructed Magnetic Field Map (MFM) obtained through the solution of the inverse problem shows good agreement with the simulated MFM.

4.8 Effect of noise on source localization: Two dipoles analysis

The influence of noise on the source localization was also investigated for the case of two dipoles. The values of the dipole moments and the position parameters assumed for the two equivalent current dipoles (ECDs) for the purposes of simulation are given in table 4.3. The coordinate system is same as for the single dipole case in section 4.7. The magnetic field gradient values are generated at a total of 36 sensor locations on a 6×6 square lattice covering an area of 21 cm $\times$ 21 cm (as indicated in fig.4.4), using Eq.4.2 for $n = 2$. In this case, during reconstruction, it is possible that multiple solutions are obtained within the prescribed boundary showing a reasonably high statistical index of fit. In this circumstance, we have found it expedient to accept a solution if the two dipoles are separated by at least 2 mm in x and y positions and if the depths of the two dipoles do not differ by more than 50 mm (baseline length of the gradiometer). It is also observed that the solutions with maximum R-square (RSQ) with a 4% tolerance and the aforesaid constraints (in section 4.4) correspond to the true solutions in a large number of simulated cases.

The different levels of noise have been added to the input data to see the influence of noise on the source localization and the results are tabulated in table 4.3. The dipole parameters inferred using the present method described in section 4.4 are found to be close to the actual values assumed originally for the purposes of simulation and have also been tabulated in table 4.3. The quality of the fit can be inferred from the values of R-square (RSQ) and root mean square error (RMSE) which are also given in table 4.3. The parameters obtained after reconstruction have a localization

Table 4.3: Parameters obtained from the reconstruction of two dipoles while adding different levels of noise to the input data. ($*$) in the first two lines indicate the assumed parameters of the Equivalent Current Dipole (ECD). The ECD positions are indicated with respect to the sensor coordinates (see fig.4.4). The reconstruction of two ECDs is exact in the noise free case and shows a localization error of about 10 mm in x, 2 mm in y, and 12 mm in z coordinates for the highest noise level of 10% of rms value of the signal. It may be noted that increase in the noise level leads to a large error in the source localization and particularly in the dipole moment parameters; this emphasizes the necessity of pre-processing of the raw data by using a suitable method for noise reduction in order to obtain robust source estimation.

% of RMS Noise	Qx (μA-cm)	Qy (μA-cm)	x (cm)	y (cm)	z (cm)	RSQ (%)	RMSE (pT/cm)
No noise	-367.2*	538.3*	9.72*	8.61*	-11.26*	100.00	0.0000
	-767.4*	42.5*	4.58*	6.52*	-11.15*		
2	-318.7	521.8	9.89	8.69	-11.23	99.98	0.0529
	-857.1	74.2	4.78	6.56	-11.40		
4	-288.4	504.0	10.07	8.69	-11.21	99.91	0.1048
	-933.9	110.8	4.90	6.59	-11.64		
6	-263.3	482.5	10.27	8.64	-11.17	99.80	0.1552
	-1011.0	153.7	5.01	6.61	-11.90		
8	-237.8	457.1	10.49	8.58	-11.10	99.66	0.2042
	-1095.0	203.6	5.11	6.62	-12.18		
10	-213.8	429.9	10.71	8.49	-11.01	99.48	0.2515
	-1185.0	259.3	5.21	6.63	-12.47		

error of about 10 mm in x, 2 mm in y, and 12 mm in z coordinates for the highest noise level of 10% of root mean square (rms) value of the signal. It is also noted that the errors in the values of dipole moments becomes relatively larger as the noise level increases. The localization errors for the case of two dipoles are seen to be larger than those corresponding to the single dipole case at the same noise level. This could be on account of increase in the number of parameters to be estimated for the case of two dipoles. It may be noted in general that the **increase in the noise level leads to a large error in the source localization; this emphasizes the necessity of pre-processing** methods for noise reduction to obtain robust source estimation.

4.9 Effect of signal pre-processing on source localization

Having seen that the robustness and stability of the inverse solution is influenced by the level of noise which contaminates the signal, it is evident that use of appropriate pre-processing steps is an essential prerequisite before the source localization is carried out. Signal preprocessing with a view to eliminate or reduce the noise present in the measured data is expected to result in a more accurate localization of the source from the measured magnetic field distribution. In order to investigate the effect of pre-processing methods on the improvement in source localization, we used the methods of the Independent Component Analysis (ICA), wavelet enhanced ICA (wICA) and the combined Ensemble Empirical Mode Decomposition with ICA (EEMD-ICA) for noise reduction (as discussed in chapter 3) on the 37 channel MCG data. Fig.4.7(a) shows the grid pattern of the measurement locations (in 37 channel MCG system) superimposed on a representation of the chest surface to indicate the measurement positions relative to the heart, which is schematically shown as inlay. The origin of the coordinate system is taken to lie in the plane containing the sensors used for measurements. Fig.4.7(b) shows the representative cardiac cycle (which was pre-processed by EEMD-ICA as discussed in chapter 3, see fig.3.18), at the 37 spatial locations for a normal 27 year old human subject. This spatio-temporal MCG data was used for constructing the magnetic field maps (MFM), at different instants of cardiac cycle, which were successively used for construction of Pseudo Current Density (PCD) maps as well as for obtaining the cardiac source parameters through the solution of the inverse problem. In the following sections, we discuss the results of the effect of pre-processing methods on the MFM, PCD maps and the inverse solution.

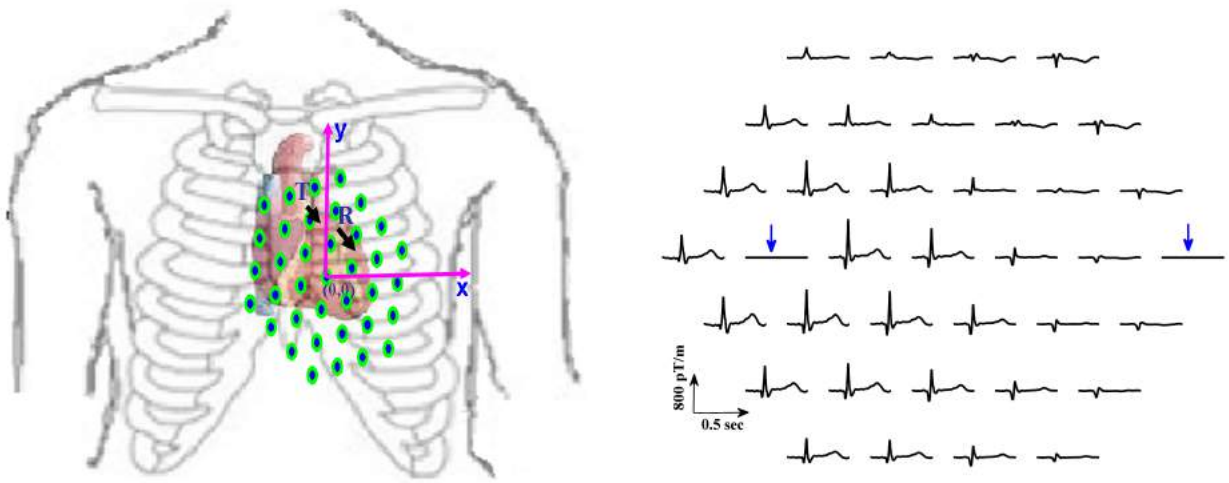

(a) (b)

Figure 4.7: (a) The two dimensional thoracic surface of a subject showing the location of the grid pattern (the left jugular notch over the sternum provided the reference) used for the measurement using 37 channel MCG system, as well as other anatomical landmarks relative to the heart. The origin of the coordinate system is taken to lie in the plane containing the sensors for measurements. The sensor at the origin (0,0) is 14 cm vertically down on the y-axis and 3 cm horizontally left on the x-axis with respect to the left-jugular notch of the subject, which was used as an anatomical landmark. The black arrows represent the orientations of the respective dipoles obtained from the fit at the instants of the R and T peaks (see section 4.12). (b) The pre-processed MCG by EEMD-ICA (refer fig.3.18(d) in chapter 3) at the 37 spatial locations for a single epoch (un-averaged). The blue arrows indicate the channels which were not functional during these measurements.

4.10 Effect of signal preprocessing on MFM

The effect of denoising of the measured signals by the three ICA based denoising methods, viz., Independent Component Analysis (ICA), wavelet enhanced ICA and combined Ensemble Empirical Mode Decomposition and ICA (EEMD-ICA), on the Magnetic Field Map (MFM) is illustrated in fig.4.8. The top to bottom panels in fig.4.8(a)-(d) illustrate the MFM obtained during the T-wave at different instants (indicated at the top of each MFM) for the raw data, and for the data denoised using the ICA alone, wICA and EEMD-ICA as the respective denoising techniques. The noise contained in the raw data distorts the field map and leads to poor source localization when it is used to infer the source through the solution of the inverse problem. The MFM obtained using the data denoised by ICA alone, wICA and EEMD-ICA techniques respectively demonstrate progressively resolved field maps. Among these, the MFM obtained by the EEMD-ICA method stands out as very highly resolved compared to those obtained by ICA alone and by wICA and

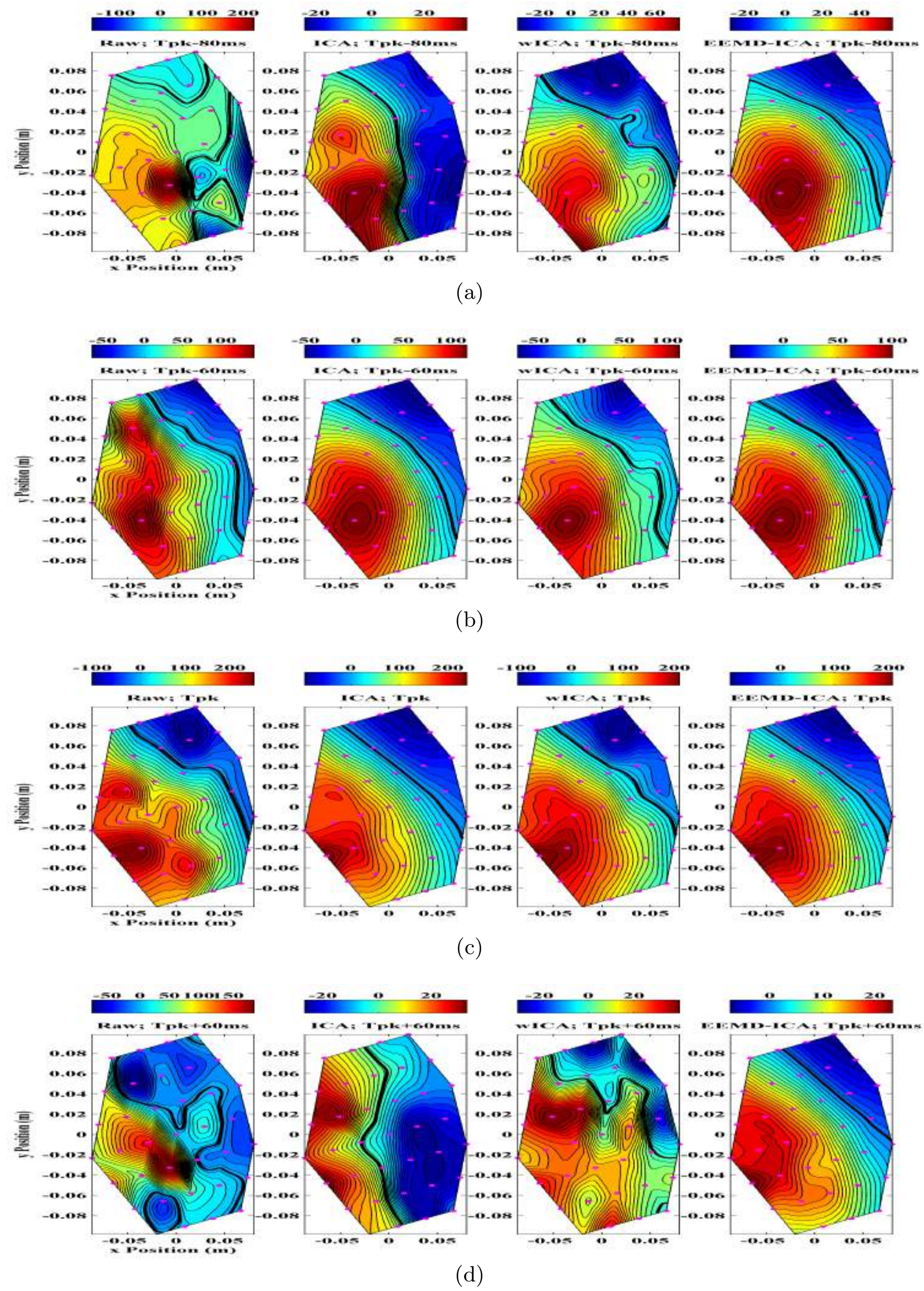

Figure 4.8: The top to bottom panels represent the Magnetic Field Maps (MFM) constructed at the different instants, Tpk-80, Tpk-60, Tpk and Tpk+60 ms respectively, of cardiac cycle during the T-wave (refer fig.4.5(a)). The panels from left to right illustrates the MFM for the raw MCG data and after it is denoised by ICA alone, wICA and EEMD-ICA respectively. Here, the Tpk refers to the instant of T-peak; Tpk-80ms and Tpk+60ms respectively refer to the instants in the cardiac cycle before 80ms and after 60ms from the T-peak. The other time instants are indicated in a similar way. The color bar indicates the magnetic field gradient values (pT/m). The dots (magenta color) on the MFM indicate the positions of the sensors during the measurement (refer fig.4.7(a)) and the thick black line is the line along which the field is close to zero. The EEMD-ICA is seen to result in a clearly resolved and well formed dipolar pattern, at different instants of time during the T-wave, compared to the ICA alone and wICA methods.

reveals a very clear dipolar pattern. Also, in the **MFM obtained from the signals denoised by EEMD-ICA, the dipolar pattern is well maintained** at different instants of cardiac cycle during the T-wave, when compared to those obtained from the signals denoised by ICA alone and wICA methods. These results suggest that the MFM obtained after preprocessing the data by the EEMD-ICA technique would yield a more robust and stable inverse solution.

4.11 Effect of signal preprocessing on PCD maps

The performance of the three denoising techniques is further compared by constructing the Pseudo Current Density (PCD) maps or the current arrow maps [4] using Hosaka-Cohen transformation [3]. The PCD map, as discussed in section 4.2, provides an approximate 2D representation of the 3D current density distribution and the source may be assumed to be located at a place where the maximum current is indicated in the PCD map. The top to bottom panels in fig.4.9 illustrate the PCD maps obtained during the T-wave at different instants of time (corresponding to the MFM in fig.4.8) for the raw data, and for the data denoised using ICA alone, wICA and EEMD-ICA respectively shown in the left to the right panels. In each PCD map, the current density value (computed from Eq.4.3) is normalized to unity at each instant of time and the color scales are graded between 0.5 (blue) and 1 (red). The arrows in the PCD map indicate the probable direction of current flow and the length of the arrows indicate the magnitude of the current. The red color indicates the maximum current flow where the source is located. The origin of the coordinate system is taken to lie in the plane containing the sensors for measurements. During the MCG measurements, the cryostat was positioned in such a way that the sensor at the origin (0,0) was at a location that was displaced by 14 cm along the negative y-axis and 3 cm along the positive x-axis (reference to fig.4.7) with respect to the left-jugular notch of the subject, which was taken to be the anatomical reference landmark. It is expected that during the T-wave (ventricular repolarization), the activation centre is confined to the ventricular region. However, in the PCD map constructed using the raw data, the source is seen to be at a location inferior to the chest and the activation centres inferred at different instants of time are found to be at different locations. This spread of activation sites during the T-wave, although not clearly seen in the MFM but seen in the PCD map, is due to the fact that the PCD map is more sensitive to small spatial fluctuations in the magnetic

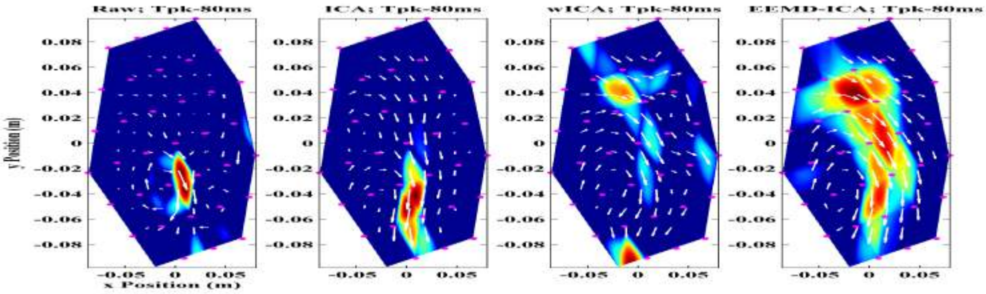

(a)

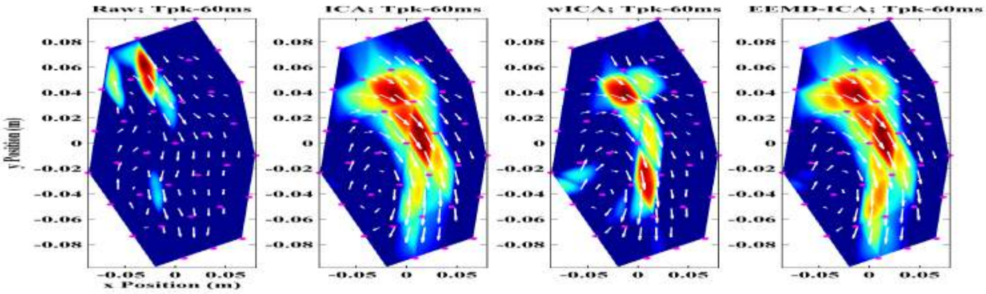

(b)

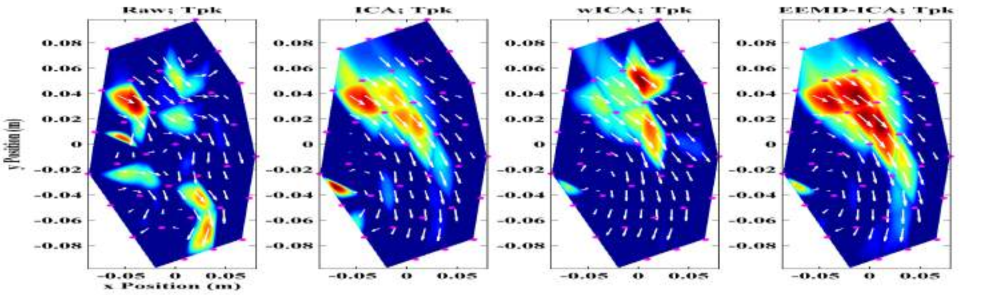

(c)

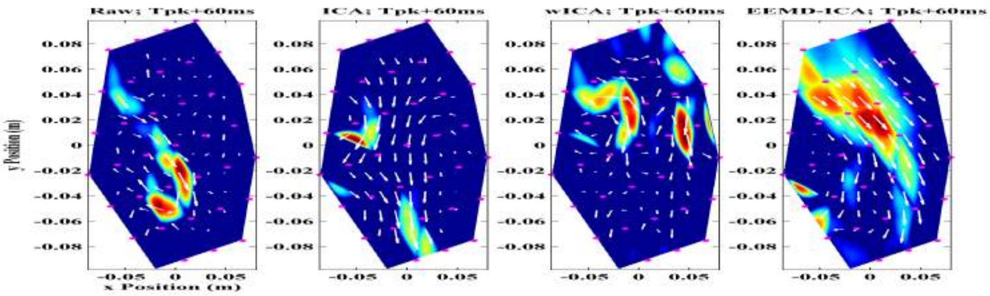

(d)

Figure 4.9: The top to bottom panels represent the Pseudo Current Density (PCD) map constructed at the different instants, Tpk-80, Tpk-60, Tpk and Tpk+60 ms respectively, of cardiac cycle during the T-wave (refer fig.4.5(a)). The panels from left to right illustrates the PCD map for the raw MCG data and after it is denoised by ICA alone, wICA and EEMD-ICA respectively. Here, the Tpk refers to the instant of T-peak; Tpk-80ms and Tpk+60ms respectively refer to the instants in the cardiac cycle before 80ms and after 60ms from the T-peak. The other time instants are indicated in a similar way. The dots (magenta color) on the PCD map indicate the positions of the sensors (refer fig.4.7(a)). The red color indicates the maximum current flow, where the source is located, and the arrows indicate the direction of current flow. The EEMD-ICA is seen to result in a consistently located activation centres (or source location), at different instants of time during the T-wave, compared to the ICA alone and wICA methods.

field values due to the presence of residual noise; this is on account of the fact that the PCD map is obtained from the spatial derivatives of the magnetic field, and the derivatives are sensitive to finer details (or fluctuations) present in the original input data. However, the PCD maps obtained from the EEMD-ICA provide a clearer and well resolved information relating to the activation centre during the ventricular repolarization for a normal subject. In the case of the data denoised by EEMD-ICA, it may also be noted that **the activation centre is consistent in location and confined** to approximately the same region at different instants of time of the T-wave. It is evident that the combined Ensemble Empirical Mode Decomposition and Independent Component Analysis (EEMD-ICA) method provides a superior suppression of noise present in the signal (as seen in fig.3.18 in chapter 3) and consequently yields a more reliable spatial localization of the source when compared to the conventional techniques such as Independent Component Analysis (ICA) alone and wavelet enhanced ICA (wICA) methods.

4.12 Effect of signal preprocessing on inverse solution

We further analyze the effect of pre-processing of signals by the above three denoising techniques, viz., Independent Component Analysis (ICA) alone, wavelet enhanced ICA (wICA) and Ensemble Empirical Mode Decomposition and Independent Component Analysis (EEMD-ICA) on the source parameters of the Equivalent Current Dipole (ECD) estimated through the solution of the inverse problem. The single ECD source model and the horizontally layered conductor model [2] have been adopted for the solution of the inverse problem using the nonlinear least square optimization approach as discussed in section 4.4. A stable and physically consistent inverse solution (at different instants of time corresponding to the R-wave and the T-wave, as indicated in fig.4.5(a)) with a high value for the statistical index R-square (RSQ) was observed for the data denoised by EEMD-ICA technique, which is already evident from the stable dipolar MFM (fig.4.8), when compared to the inverse solution obtained using data denoised by ICA alone and wICA techniques. We list in table 4.4 the ECD parameters obtained at two different instants of time during the cardiac cycle, viz., the R-peak (ventricular depolarization) and the T-peak (ventricular repolarization).

The indicated ECD parameters in table 4.4 are with respect to the sensor plane origin, which is relatively positioned at 3 cm left in the horizontal X direction and 14 cm down in the vertical Y

direction in the $X - Y$ plane with respect to the location of the left jugular notch of the subject (refer fig.4.7(a)), which is taken to be the anatomical reference point for the purposes of alignment. As expected, the dipole moment at the instant of R-peak is relatively larger than that at the instant

Table 4.4: The estimated parameters of the ECD, for a 27 year old normal subject at the R-peak and the T-peak, obtained from the data denoised by three different ICA based techniques. ($\star$) indicate the high R-square (RSQ) with physically consistent solution and (‡) indicate physically inconsistent solution with high RSQ. The ECD position parameters indicated in table 4.4 are with respect to the origin of coordinates in the sensor plane, which is located 3 cm left in the horizontal X direction and 14 cm down in the vertical Y direction in the $X - Y$ plane (refer fig.4.7(a)) with respect to the location of the left jugular notch of the subject, which is taken to be the anatomical reference point for the purposes of alignment.

Instants	Methods	Q_x (μA-cm)	Q_y (μA-cm)	x (cm)	y (cm)	z (cm)	RSQ (%)	RMSE (pT/cm)
R-peak	ICA	1855.5	-2782.7	3.92	2.64	-10.69	89.95	0.89411
	wICA	1904.5	-3064.3	3.58	2.97	-11.28	90.92	0.82990
	EEMD-ICA	2204.6	-3278.1	3.71	3.12	-11.32	91.30*	0.86354
T-peak	ICA	2315.5	-1499.6	-6.17‡	9.70‡	-17.71‡	94.20‡	0.15569
	wICA	1577.5	-1065.3	-1.71	6.07	-14.61	92.21	0.25378
	EEMD-ICA	1594.7	-1096.6	-1.66	6.01	-14.95	94.11*	0.21196

of T-peak in all the cases. It may be noted that the root mean square error (RMSE) and RSQ represent different statistical indices for indicating the quality of the fit, and quite often, a higher value of RSQ does not necessarily imply a lower value of RMSE. This is due to the fact that the RSQ is not much sensitive to scaling of data unlike RMSE. Hence, for further use, we consider only RSQ. It may be noted from table 4.4 that the ECD parameters obtained at the instant of R-peak (where the SNR is relatively high) using the MCG data denoised by ICA alone, wICA and EEMD-ICA techniques are close to each other. Nevertheless, the EEMD-ICA shows the highest values (of the three methods) for the statistical index RSQ and yields somewhat larger dipole strength compared to that inferred from the data denoised using the techniques such as the ICA alone and wICA. On the other hand, the ECD parameters obtained at the instant of the T-peak (where the SNR is not as high) using the MCG data denoised by ICA alone yields source locations which are physically inconsistent (i.e., the source location (refer to fig.4.7(a)) which is displaced 3 cm to the right and 4 cm down in the $X - Y$ plane with respect to the left jugular notch), although the RSQ is high. It is expected that the source location of the ventricular activity should be towards the left of the jugular notch. The MCG data denoised by the other two techniques wICA and EEMD-ICA yield physically consistent solutions, which are also close to each other; however, the data denoised by EEMD-ICA yields a higher value for the RSQ when compared to the data denoised by wICA. Although the source locations inferred, through the solution of the inverse problem, at the instant of a peak in the cardiac cycle (high SNR) were close to each other when the data was denoised using wICA and EEMD-ICA, there are differences in the source locations given by the two denoising algorithms, when the source localization is carried out at an instant of time away from a peak (low SNR). Our investigations show that in all the cases, the denoising of the data by **EEMD-ICA resulted in a better and more credible source localization.** It may also be noted that the data fitted to the single ECD at the instant of the R-peak and the T-peak shows that the value of the statistical index RSQ is higher for the magnetic field distribution at the T-peak compared to that at the R-peak. This may be attributed to the fact that the magnetic field distribution during the ventricular repolarization is closer to that expected for a dipolar source, when compared to the magnetic field distribution during the ventricular depolarization.

4.13 Conclusions

The cardiac source estimation from the MCG data through the construction of Pseudo Current Density (PCD) map and the solution of the inverse problem in the context of a single Equivalent Current Dipole (ECD) is discussed. The method for reconstructing the source parameters of the ECD using different sets of pseudo-random numbers as the initial values in the nonlinear least square optimization technique using Levenberg-Marquardt (LM) algorithm is described. The method was applied to the experimental data related to the measured magnetic field distribution produced by a current carrying source coil and was validated by demonstrating its ability to locate the source within a localization error of $\pm 2mm$. The method has been applied to the experimentally measured MCG data for four subjects and has been shown to yield reasonable values for the parameters of the ECD. The localization error could be further minimized by employing more realistic source and volume conductor models. It is evident that the iterative nonlinear least square optimization with pseudo-random numbers as initial parameter values is useful in evaluating the ECD parameters from the measured data at different instants of cardiac cycle and has the potential to reveal significant information that is of value to a cardiologist.

The effect of noise on the source localization accuracy has been investigated and the results show that the accuracy of the source localization decreases with increasing noise level. Further, the effect of signal denoising on the construction of PCD maps was investigated and it was found that the PCD maps constructed from the signals denoised by the EEMD-ICA method yielded a clearer and well resolved source estimate compared to the situation when the signals were denoised by the ICA alone and wICA methods. Also, the data denoised by EEMD-ICA yielded a stable and robust inverse solution when compared to the situation when the signals were denoised by the ICA alone and wICA methods.

Bibliography

[1] P.C. Hansen, M.L. Kringelbach and R. Salmelin. MEG: An Introduction to Methods. Oxford Univ. Press. New York. 2010.

[2] J. Sarvas. Basic mathematical and electromagnetic concepts of the biomagnetic inverse problem. *Phys. Med. Biol.* **32** (1987) 11 - 22.

[3] W. Haberkorn, U. Steinhoff, M. Burghoff, O. Kosch, A. Morguet and H. Koch. Pseudo current density maps of electrophysiological heart, nerve or brain function and their physical basis. *Biomagn. Res. Technol.* **4**:5 (2006).

[4] K. Ogata, A. Kandori, T. Miyashita, K. Sekihara and K. Tsukada. A comparison of two-dimensional techniques for converting magnetocardiogram maps into effective current source distributions. *Rev. Sci. Instrum.* **82** (2011) 014302.

[5] M. Hämäläinen, R. Hari, R.J. Ilmoniemi, J. Knuutila and O.V. Lounasmaa. Magnetoencephalography-theory, instrumentation, and applications to noninvasive studies of the working human brain. *Rev. Mod. Phys.* **65** (1993) 413 - 497.

[6] C.D. Gratta, V. Pizzella, F. Tecchio and G.L. Romani. Magnetoencephalography - a noninvasive brain imaging method with 1 ms time resolution. *Rep. Prog. Phys.* **64** (2001) 1759 - 1814.

[7] Hans Koch. Recent advances in magnetocardiography. *J. Electrocardiol.* **37** (2004) 117 - 122.

[8] D.W. Marquardt. An algorithm for least-squares estimation of nonlinear parameters. *SIAM J Appl. Math.* **11** (1963) 431 - 441.

[9] J.A. Nelder and R. Mead. A simplex method for function minimization. *Comput. J.* **7** (1965) 308 - 313.

[10] J.C. Mosher, P.S. Lewis and R.M. Leahy. Multiple dipole modeling and localization from spatio-temporal MEG data. *IEEE Trans. Biomed. Eng.* **39** (1992) 541 - 557.

[11] H. Haneishi, N. Ohyama, K. Sekihara and T. Honda. Multiple current dipole estimation using simulated annealing. *IEEE Trans. Biomed. Eng.* **41** (1994) 1004 - 1009.

[12] K. Uutela, M. Hämäläinen and R. Salmelin. Global optimization in the localization of neuromagnetic sources. *IEEE Trans. Biomed. Eng.* **45** (1998) 716 - 723.

[13] Jia-Jin J Chen, Jhy-Guang Yeh and Jing-Jane Tsai. Initial estimation methods for dipole modeling in localization of epileptogenic focus. *Medical Eng. and Physics* **20** (1998) 11 - 20.

[14] M. Embrechts, B. Szymanski, K. Sternickel, T. Naenna and R. Bragaspathi. Use of machine learning for classification of magnetocardiograms. *IEEE Proc. Syst. Man Cybern.* **2** (2003) 1400 - 1405.

[15] P.H. Langner and S.R. Moore. Location of the electrical center of ventricular repolarization. *American Heart Journal.* **52** (1956) 335 - 342.

[16] N. Mariyappa, C. Parasakthi, S. Sengottuvel, K. Gireesan, Rajesh Patel, M.P. Janawadkar, C.S. Sundar and T.S. Radhakrishnan. Dipole localisation using SQUID based measurements: Application to magnetocardiography. *Physica C.* **477** (2012) 15 - 19.

[17] N. Mariyappa, M.P. Janawadkar, T.S. Radhakrishnan, C.S. Sundar, S. Sengottuvel, K. Gireesan, C. Parasakthi and Rajesh Patel. Elucidation of equivalent current dipole from Magnetocardiography measurements. *AIP Conf. Proc.* **1349** (2010) 449 - 450.

5 Summary and Future work

5.1 Summary

In the thesis, we described the in-house development of MCG facility at IGCAR, Kalpakkam and the development of suitable methods for preprocessing and analysis of the recorded MCG data. The salient features of the thesis are:

- Setting up of a multichannel Magnetocardiography (MCG) measurement facility which involved a careful assembly and wiring of SQUID sensors arranged inside a flat bottom liquid helium cryostat is described. The MCG system has been progressively upgraded from an instrument with a single SQUID channel to an instrument with 37 SQUID channels arranged in a plane as a hexagonal array of 37 SQUID sensors with an inter-sensor spacing of 3 cm.
- The sensor output was calibrated by coupling a magnetic field of known strength and recording the system response. All the SQUID sensors were characterized by making detailed measurements of spectral density of voltage noise as a function of frequency. Recording of MCG data on normal human subjects as well as those with a cardiac dysfunction is described.
- Ensemble Empirical Mode Decomposition (EEMD) method is adopted for MCG signal denoising and the procedure for extracting the Intrinsic Mode Functions (IMFs) is described in chapter 3. In the EEMD method, we introduced the empirical relation for noise amplitude related to the standard deviation of the second order time derivative of the signal (as against the conventional use of the amplitude related to the standard deviation of the signal itself) in order to prevent mode mixing, and achieve substantial reduction of noise using relatively lower number of ensemble averages. The use of interval thresholding method has been described to

reduce the discontinuities in the reconstructed denoised signal, which usually appear when direct thresholding is applied.

- The elimination of baseline drift associated with smooth low frequency variations which sometimes arise due to the subject's breathing and movement has been elucidated. A novel method to eliminate the sudden and discontinuous changes in the baseline termed as high frequency baseline drift has been proposed. The EEMD based method eliminates the high frequency baseline drift more effectively as compared to the standard wavelet based method.

- The EEMD hard-interval thresholding method is applied to denoise the single channel MCG data and its performance is compared with that achieved using other standard techniques such as wavelet transform and Independent Component Analysis (ICA). The signal quality has been shown to be significantly improved by EEMD based denoising method when compared to that obtained by wavelet and ICA based denoising methods.

- The EEMD based method has also been used to detect the extremely weak signal associated with His-bundle magnetic field employing considerably lower number of cardiac cycles for signal averaging using QRS onset as the fiducial reference point.

- A method based on a combination of Ensemble Empirical Mode Decomposition (EEMD) and Independent Component Analysis (ICA) is proposed with a view to substantially reduce computational burden associated with EEMD alone for denoising of multichannel MCG data with a large number of channels and is shown to achieve superior signal-to-noise ratio (SNR) with lower computational burden compared to either ICA alone or wavelet enhanced ICA.

- A simple Equivalent Current Dipole (ECD) model is adopted for cardiac source and the methods for visualizing the cardiac source through the construction of Pseudo Current Density (PCD) map and the estimation of source parameters through the solution of the inverse problem are described in chapter 4.

- A nonlinear least square optimization technique with independent sets of pseudo-random numbers as initial estimates of source parameter values is used for solving the inverse problem; use of independent sets of pseudo-random numbers over a large number of trials is shown to be successful in avoiding the possibility of the solution getting trapped in a local minimum. In view of the non-uniqueness of the solution to the inverse problem, necessity of imposing realistic constraints to obtain the physiologically relevant solution is emphasized. The method was successfully applied to the experimental data corresponding to the magnetic field distribution produced by a current carrying source coil at a known position. The method was shown to yield a localization error of $\pm 2\ mm$ for the known dipole location and was thus demonstrated to yield a reliable estimate of the source parameters from an analysis of the magnetic field distribution.

- The influence of noise on the source localization accuracy was investigated by simulating the magnetic field distribution produced by single and two equivalent current dipoles with various levels of input noise deliberately added to the data; the results show that the localization error increases with increase in the added noise level. These results emphasize the importance of pre-processing of MCG signals for noise reduction.

- The effect of denoising the MCG data, by ICA, wICA and EEMD-ICA, on the magnetic field maps (MFM) and the Pseudo Current Density (PCD) maps has been elucidated for the 37 channel MCG data. It is shown that the data denoised by EEMD-ICA technique provides stable empirical source estimate through the PCD map at different instants of cardiac cycle during the T-wave when compared to that obtained by ICA and wICA. Further, the effect of signal denoising on the estimation of source parameters obtained by solving the inverse problem was analyzed for the 37 channel MCG data. It is shown that the denoising of the 37 channel MCG data using a combination of EEMD and ICA yielded a robust estimation of the source parameters compared to what can be achieved using ICA or wICA for denoising. The present study shows that, **although the noise reduction is crucial for realizing a lower source localization error, it is also important to choose an appropriate method like EEMD-ICA for signal pre-processing**, for better noise suppression and, consequently, a robust and credible source estimation.

5.2 Future Work

- It is well known that a cardiac source could not always be modeled with reasonable accuracy as a single Equivalent Current Dipole (ECD) embedded in a horizontal layered conductor, and hence, there is a considerable scope for adopting more realistic models for the source as well as the volume conductor during the analysis of the measured MCG data. It is also important to use anatomical information derived from studies such as Magnetic Resonance Imaging (MRI) to constrain the solution to correspond to the physiologically relevant solution. There is a need to develop suitable algorithms to project the locations of sources (dipoles, currents etc.) inferred by an analysis of MCG data onto an MRI image of the subject in order to assist the clinician in better visualizing the information derived from an analysis of the MCG data.
- The signal preprocessing techniques developed in the context of the MCG data could also be used for the preprocessing of experimental MEG data measured with the 86 channel whole head Magnetoencephalography (MEG) system, which is getting ready for measurements in our laboratory.

List of Publications:

(a). Published:

1. Gireesan, K., Parasakthi, C., Sengottuvel, S., **Mariyappa, N.**, Rajesh Patel, Janawadkar, M.P., and Radhakrishnan, T.S., Establishment of 13 Channel SQUID based MEG system for studies in biomagnetism, *Indian Journal of Cryogenics*, 2012, **36**(1-4):169-172.

2. **Mariyappa, N.**, Parasakthi, C., Sengottuvel, S., Gireesan, K., Rajesh Patel, Janawadkar, M.P., Sundar, C.S., and Radhakrishnan, T.S., Dipole localisation using SQUID based measurements: Application to magnetocardiography, *Physica C*, 2012, **477**: 15-19.

3. Sengottuvel, S., Parasakthi, C., **Mariyappa, N.**, Rajesh Patel, Gireesan, K., Janawadkar, M.P., Radhakrishnan, T.S., and Muralidharan, T.R., Enhancing the reliability in the non-invasive measurement of the His bundle magnetic field using a novel signal averaging methodology, *Annals of Noninvasive Electrocardiology*, 2012, **17**(3):186-194.

(b). Communicated:

1. **Mariyappa, N.**, Sengottuvel, S., Parasakthi, C., Gireesan, K., Janawadkar, M.P., Radhakrishnan, T.S., and Sundar, C.S., Baseline Drift Removal and Denoising of Magnetocardiography data using Ensemble Empirical Mode Decomposition: Role of Noise Amplitude and the Thresholding Effect (Communicated to *Medical Engineering & Physics*).

2. **Mariyappa, N.**, Sengottuvel, S., Rajesh Patel, Gireesan, K., Janawadkar, M.P., Radhakrishnan, T.S., and Sundar, C.S., Denoising of multichannel MCG data by the combination of EEMD and ICA and its effect on the pseudo current density maps (Communicated to *Medical & Biological Engineering & Computing*).

(c). Conferences/Proceedings:

1. **Mariyappa, N.**, Janawadkar, M.P., Radhakrishnan, T.S., Sundar, C.S., Sengottuvel, S., Gireesan, K., Parasakthi, C., and Rajesh Patel, Elucidation of Equivalent Current Dipole from Magnetocardiography measurements, *AIP Conference Proceedings*, 2011, **1349**:449-450.

2. **Mariyappa, N.**, Parasakthi, C., Sengottuvel, S., Rajesh Patel, Gireesan, K., Radhakrishnan, T.S., Janawadkar, M.P., Sundar, C.S., Improving noise performance of the SQUID in the presence of high resistive leads, *AIP Conference Proceedings*, 2012, **1447**:891-892.

3. Parasakthi, C., Rajesh Patel, Sengottuvel, S., **Mariyappa, N.**, Gireesan, K., Janawadkar, M.P., Radhakrishnan, T.S., Establishment of 37 Channel SQUID System for Magnetocardiography, *AIP Conference Proceedings*, 2012, **1447**:871-872.

4. Sengottuvel, S., Parasakthi, C., **Mariyappa, N.**, Rajesh Patel, Gireesan, K., Janawadkar, M.P., Radhakrishnan, T.S., His bundle activity by Magnetocardiography with QRS-onset as fiducial point, *Proceedings of BIOMAG*, 2012.

5. **Mariyappa, N.**, Parasakthi, C., Gireesan, K., Sengottuvel, S., Rajesh Patel, Janawadkar, M.P., Radhakrishnan, T.S., Sundar, C.S., Development of Multichannel MEG System at IGCAR, *AIP Conference Proceedings*, 2013, **1512**:1152-1153.